

NASA Contractor Report 4182

Calculation of Aerodynamic  
Characteristics of Airplane  
Configurations at  
High Angles of Attack

J. B. Tseng and C. Edward Lan

GRANT NAG1-635  
OCTOBER 1988

(NASA-CR-4182) CALCULATION OF AERODYNAMIC  
CHARACTERISTICS OF AIRPLANE CONFIGURATIONS  
AT HIGH ANGLES OF ATTACK Final Report  
(Kansas Univ. Center for Research) 116 p

N88-28891

CSCL 01A H1/02 0161491  
Unclas

NASA

NASA Contractor Report 4182

Calculation of Aerodynamic  
Characteristics of Airplane  
Configurations at  
High Angles of Attack

J. B. Tseng and C. Edward Lan  
*Flight Research Laboratory*  
*University of Kansas Center for Research, Inc.*  
*Lawrence, Kansas*

Prepared for  
Langley Research Center  
under Grant NAG1-635



National Aeronautics  
and Space Administration

Scientific and Technical  
Information Division

1988



## SUMMARY

In this study, calculation of longitudinal and lateral-directional aerodynamic characteristics of airplanes by the VORSTAB code is examined. The numerical predictions are based on the potential flow theory with the corrections of high angle-of-attack phenomena; namely, vortex flow and boundary layer separation effects. To account for the vortex flow effect, vortex lift, vortex action point, augmented vortex lift and vortex breakdown effect through the method of suction analogy are included. The effect of boundary layer separation is obtained by matching the nonlinear section data with the three-dimensional lift characteristics iteratively.

Through correlation with results for nine fighter configurations, it is concluded that reasonably accurate prediction of longitudinal and static lateral-directional aerodynamics can be obtained with the VORSTAB code up to an angle of attack at which wake interference and forebody vortex effect are not important. Possible reasons for discrepancy at higher angles of attack are discussed.

PRECEDING PAGE BLANK NOT FILMED.



LIST OF SYMBOLS

$a_n$	Fourier coefficients
$b$	Span
$c$	Local chord
$\bar{c}$	Mean aerodynamic chord
$\tilde{c}$	A characteristic length in the calculation of augmented vortex lift. See Equation (47).
$C, C'$	Sectional leading-edge singularity parameter
$c_d$	Sectional drag coefficient
$C_D$	Drag coefficient
$C_{D_i}$	Induced drag coefficient
$c_l$	Sectional lift coefficient
$C_L$	Total lift coefficient
$C_l$	Rolling moment coefficient
$C_{l_\beta}$	$\partial C_l / \partial \beta$
$C_{l_p}$	$\partial C_l / \partial \bar{p}$
$C_{l_r}$	$\partial C_l / \partial \bar{r}$
$c_m$	Sectional pitching moment coefficient
$C_m$	Total pitching moment coefficient
$C_n$	Yawing moment coefficient
$C_{n_\beta}$	$\partial C_n / \partial \beta$
$C_N$	Body normal force coefficient based on maximum cross-sectional area
$C_{N,V}$	Sectional normal force coefficient due to body vortex lift
$C_{N,VA}$	Total augmented-vortex normal force coefficient on a body

PRECEDING PAGE BLANK NOT FILMED

$C_p$	Pressure coefficient
$\Delta C_p$	Lifting pressure coefficient
$c_s$	Sectional leading-edge suction coefficient
$\bar{c}_s$	$cc_s/\bar{c} \sin^2 \alpha$
$c_t$	Sectional leading-edge thrust coefficient
$C_s$	Total leading-edge suction coefficient
$c_{sf}$	Sectional side-force coefficient of a body
$c_{sf,N}$	Total suction force coefficient produced by a body nose section
$c_t$	Sectional leading-edge thrust coefficient
$C_y$	Side force coefficient
$F_a$	Augmented vortex lift
$f$	Ratio of vortex-induced vertical velocity to the free stream (Equation 65) or ratio of sectional lift coefficients from 2-D and 3-D calculations (Equation 81)
$h$	Vortex action point location on a body. See Equation (73).
$l$	Leading-edge length
$l_N$	Body nose length
$G$	Local tip suction singularity parameter
$k$	Residual vortex lift factor
$\vec{n}$	Unit normal vector
$N$	Number of chordwise vortex elements in a strip
$p$	Roll rate
$\bar{p}$	$pb/2V_\infty$
$q$	Pitch rate
$r$	Radial coordinate or yaw rate
$\bar{r}$	$rb/2V_\infty$

$\vec{r}$	Position vector
$r_{av}$	Average vortex action radius in producing force through momentum transfer. See Equation (46).
$r_o$	Leading-edge radius
$r_v$	Vortex action point location measured from the leading-edge
$R$	Body radius
$S$	Reference area
$S_t$	Total tip suction coefficient
$u, v, w$	Induced velocity components along x, y, z coordinates, respectively
$\vec{V}$	Total velocity vector
$V_n$	Induced normal velocity
$V_\infty$	Freestream velocity
$x, y, z$	Cartesian coordinates with x being positive pointing downstream, a positive y pointing to the right, and a positive z pointing upwards
$x_p$	Body axial station downstream of which the potential flow does not exist
$x_s$	Body axial station at which the vortex separation starts
$\bar{\Delta x}$	Nondimensional x-distance from the trailing edge to the vortex breakdown point
$x_\ell$	Leading-edge x-coordinate
$\bar{y}_{BD}$	Spanwise location of vortex breakdown point nondimensionalized with respect to half span
$\bar{y}_c$	Nondimensional centroid location of the $\bar{c}_s$ -distribution from inboard to $\eta$ of $\bar{c}_{s(max)}$
$\bar{y}_\ell$	Distance from apex to centroid of $\bar{c}_s$ -distribution from inboard to $\eta$ of $\bar{c}_{s(max)}$ , measured along the leading edge and referred to half span



$z_c$	Camber surface ordinate
$z_l$	$z$ -coordinate of the leading edge
<u>Greek</u>	
$\alpha$	Angle of attack
$\alpha_o$	Sectional angle of zero lift
$\alpha_{BD}$	$\alpha$ for vortex breakdown at the trailing edge in symmetrical loading
$\alpha_s$	Angle of attack of initial vortex separation
$\alpha_{tw}$	Difference in angles of attack at tip and root sections, negative for washout
$\beta$	Sideslip angle, or $\sqrt{1 - M^2}$
$\delta_A$	Aileron deflection angle
$\delta_c$	Angle of chordwise camber slope
$\delta_r$	Rudder deflection angle
$\eta$	$y/b/2$
$\Gamma$	Sectional circulation
$\gamma_x$	Nondimensional streamwise vortex density
$\gamma_y$ or $\gamma$	Nondimensional spanwise vortex density
$\Lambda$	Sweep angle
$\phi$	Geometric dihedral
$\Phi$	Velocity potential
$\rho$	Density
$\theta$	Angular coordinate of a body cross section
$\theta_A$	Angular location of the augmented-vortex action point on a body cross section
$\theta_c$	Angular location of the vortex action point on a body cross section

### Subscript

a	Antisymmetrical loading
aug	Augmented
$\alpha$	Due to $\alpha$ in symmetrical loading
$\beta$	Sideslip
BR	Vortex breakdown on the right wing
BL	Vortex breakdown on the left wing
f	Fuselage
l	Leading edge
max	Maximum
n	Normal direction
p	Roll rate
r	Yaw rate
t	Tip
tw	Twist
v,le	Leading-edge vortex
w	Wing
z	Normal to a planform
$\infty$	Freestream

### Abbreviation

PAN AIR	Panel Aerodynamics
QVLM	Quasi-Vortex-Lattice Method
SAAP	Stalled Airfoil Analysis Program
VSAERO	Vortex Separation Aerodynamics



## 1. INTRODUCTION

Currently there is a strong interest in the technical community in longitudinal and lateral-directional aerodynamics at high angles of attack for fighter aircraft. Maneuvering flight at high angles of attack may induce boundary-layer separation and vortex-separated flow over aerodynamic surfaces. These flow phenomena affect not only the individual aerodynamic surfaces on which these phenomena occur but also those in close proximity. As a result of an adverse pressure gradient, the well organized vortex flow may break down, significantly changing the aerodynamics of the vehicle. These flow patterns are now well known qualitatively for fighter configurations from extensive testing in wind and water tunnels. However, development of quantitative prediction methods has not kept pace with tunnel testing.

Eventually, a theoretical method for predicting aerodynamics at high angles of attack would be ideally based on Navier-Stokes solutions with appropriate turbulence modeling. However, for applications to preliminary design, this is not feasible at the present time due to inadequate computer resources. Therefore, a practical approach would be one involving panel or panel-like methods with corrections for high angle-of-attack flow features. For example, one currently available computer code for complete aircraft configurations is the PAN AIR (refs. 1 and 2). This code is based on the solution of the Prandtl-Glauert equation and may include boundary layer corrections. However, its applications to

configurations with extensive boundary-layer separation or vortex flow have not been demonstrated. It should be noted that symmetrical vortex flow without breakdown on simple configurations has been dealt with successfully in reference 3 based on a panel method. Similarly, the VSAERO code (refs. 4 and 5) was developed mainly for symmetrical flight conditions with vortex flow and boundary layer correction at moderate angles of attack. A comprehensive method for lateral-directional aerodynamics with aeroelastic effect is that of the FLEXSTAB (ref. 6). However, it was valid only in the region of linear aerodynamics, and hence at low angles of attack. Recently, the VSAERO code has been extended to calculation of stability and control characteristics of airplanes (ref. 7). Again, applications to high angle-of-attack aerodynamics have not been reported.

To remedy the inadequacy of existing methods, in particular in the area of nonlinear lateral-directional aerodynamics, the VORSTAB code was developed for vortex-dominated configurations (ref. 8). The effect of vortex lift is included through the method of suction analogy. To account for the effect of vortex breakdown, experimental data were used through a theoretical correlation parameter. The code was later extended to treat conventional fighter configurations by using nonlinear section data for the effect of boundary-layer separation (ref. 9). The nonlinear section data could be experimental or theoretical. This was done to avoid extreme difficulty in theoretical prediction of three-dimensional viscous separated flows.

In the present investigation, extensive applications of the extended VORSTAB code to fighter configurations in nonlinear longitudinal and lateral-directional aerodynamics will be reported. Both theoretical and empirical methods used in the code will be described. Numerical results for several current fighter aircraft will be presented.

## 2. THEORETICAL APPROACHES

### 2.1 General Concept

The main flow features accounted for in the VORSTAB code are illustrated in Figure 1. The flow model in the code is the potential subsonic flow, with corrections for the vortex flow effect and the boundary layer separation. The potential flow calculation is based on the small disturbance approximation of the gas dynamic equations which result in the Prandtl-Glauert equation. There are two kinds of flow singularities used in the program: horseshoe vortices for lifting surfaces and vortex multiplets for the fuselage. The strength of the singularities can be obtained by satisfying the boundary conditions on the fuselage and lifting surfaces. To properly account for the leading-edge singularity of pressure loading in the linear theory, and hence the leading-edge thrust, the Quasi-Vortex-Lattice Method (QVLM) is used (ref. 10). The lifting pressure distribution can also be correctly calculated by this method.

In addition to potential flow, the vortex flow also significantly affects the high angle-of-attack aerodynamics. The characteristics associated with vortex flow include vortex lift, action points, breakdown effect, etc. The suction analogy is used to compute the leading- and side-edge suction forces generated by the vortex flow. The action point is predicted by applying the linear momentum principle of fluid mechanics. Vortex-breakdown angles of attack and progression rates are obtained from semi-empirical formulas derived from analysis of experimental data.

Another phenomenon limiting the high angle-of-attack flight envelopes for high performance aircraft is the boundary-layer separation. To account for this effect, sectional nonlinear data are used iteratively to account for the viscous effect on the lifting surfaces. In the following, methodologies used in the code will be summarized.

## 2.2 Potential Flow Theory (Quasi-Vortex-Lattice Method)

As indicated earlier, the present potential flow method is based on the solution of the Prandtl-Glauert equation:

$$(1 - M_{\infty}^2) \frac{\partial^2 \Phi}{\partial x^2} + \frac{\partial^2 \Phi}{\partial y^2} + \frac{\partial^2 \Phi}{\partial z^2} = 0 \quad (1)$$

where  $\Phi$  is the perturbation velocity potential. The solution is represented by vortex distributions. The thin wing approximation is used throughout.

### 2.2.1 Boundary Condition

The boundary condition for the Prandtl-Glauert equation on the wing is that the normal velocity component to the wing surface should be zero. Assume that the wing surface can be described as

$$z = z_c(x,y) \quad (2)$$

Therefore, a unit normal vector on the wing surface can be defined as

$$\vec{n} = \frac{-\frac{\partial z_c}{\partial x} \vec{i} - \frac{\partial z_c}{\partial y} \vec{j} + \vec{k}}{\sqrt{1 + \left(\frac{\partial z_c}{\partial x}\right)^2 + \left(\frac{\partial z_c}{\partial y}\right)^2}} \quad (3)$$

The total velocity vector is

$$\vec{V} = (V_\infty \cos \alpha + u) \vec{i} + v \vec{j} + (w + V_\infty \sin \alpha) \vec{k} .$$

Applying the tangency condition

$$\vec{V} \cdot \vec{n} = 0 \quad (4)$$

the boundary condition becomes

$$-V_\infty \cos \alpha \frac{\partial z_c}{\partial x} - v \frac{\partial z_c}{\partial y} + V_\infty \sin \alpha + w = 0 \quad (5)$$

where  $u \partial z_c / \partial x$  has been ignored as a second-order term. For a wing with dihedral ( $\phi$ ) and twist ( $\alpha_{tw}$ ), it can be shown that (ref. 11)

$$\frac{\partial z_c}{\partial x} = \frac{-\sin \alpha_{tw} + \frac{dz_c}{dx_2} \cos \alpha_{tw}}{\cos \phi \left( \cos \alpha_{tw} + \frac{dz_c}{dx_2} \sin \alpha_{tw} \right)} \quad (6a)$$



$$\frac{\partial z_c}{\partial y} = \frac{\sin\phi \cos\alpha_{tw} + \frac{dz_c}{dy_2} \cos\phi}{\cos\phi \cos\alpha_{tw} - \frac{dz_c}{dy_2} \sin\phi} \quad (6b)$$

where the  $(x_2, y_2)$  coordinate system is illustrated in Figure 2. Basically, it is a coordinate system based on the local wing chord plane in a nonplanar configuration. For a cambered wing with small spanwise slopes  $(dz_c/dy_2)$ , it can be shown from Equation (6b) that

$$\frac{\partial z_c}{\partial y} \cong \tan\phi \quad (7)$$

Therefore, the wing boundary condition becomes

$$\begin{aligned} V_n &= \frac{w}{V_\infty} \cos\phi - \frac{v}{V_\infty} \sin\phi \\ &= \cos\phi \frac{\partial z_c}{\partial x} \cos\alpha - \cos\phi \sin\alpha \end{aligned} \quad (8)$$

With the presence of a fuselage, the induced velocity  $V_n$  on the wing consists of two terms: the effect of the wing and the effect of the fuselage. The boundary conditions on the wing and fuselage become, for the longitudinal case,

#### Wing

$$V_{nw} + V_{nf} = \cos\phi \frac{\partial z_c}{\partial x} \cos\alpha - \cos\phi \sin\alpha \quad (9)$$

#### Fuselage

$$\frac{\partial\phi_f}{\partial r} + \frac{\partial\phi_w}{\partial r} = \cos\alpha \frac{dR}{dx} - \sin\alpha \cos\theta \quad (10)$$

where  $R(x)$  is the fuselage radius. The fuselage coordinate system  $(x, \theta, r)$  is illustrated in Figure 3.

For an airplane having angular motions with rates  $p$ ,  $q$ , and  $r$ , the induced velocity at  $(x, y, z)$  due to these angular rates is

$$\begin{aligned} & -(\vec{i}p + \vec{j}q - \vec{k}r) \times (\vec{i}x + \vec{j}y + \vec{k}z) \\ & = \vec{i}(-qz - ry) + \vec{j}(rx - pz) + \vec{k}(py + qx) \end{aligned} \quad (11)$$

Adding a sideslip velocity,  $-\beta V_\infty$ , to the total velocity, the latter becomes

$$\begin{aligned} \vec{V} & = (V_\infty \cos \alpha - qz - ry + u)\vec{i} + \\ & + (v + rx - pz - \beta V_\infty)\vec{j} + \vec{k}(w + py + qx + V_\infty \sin \alpha) \end{aligned} \quad (12)$$

Substituting Equation (12) into Equation (4) and using Equation (7), the boundary condition for the angular motion becomes, after removing steady symmetrical condition and second-order terms,

#### Wing

$$\begin{aligned} V_n & = V_{nw} + V_{nf} = \frac{w}{V_\infty} \cos \phi - \frac{v}{V_\infty} \sin \phi \\ & = -\beta \sin \phi + \frac{rx - pz}{V_\infty} \sin \phi - \frac{py - qx}{V_\infty} \cos \phi \\ & = -\beta \sin \phi + \left(\frac{rb}{2V_\infty}\right)\left(\frac{2x}{b}\right) \sin \phi - \left(\frac{pb}{2V_\infty}\right) \frac{2}{b} (y \cos \phi + z \sin \phi) \\ & \quad - \left(\frac{qc}{2V_\infty}\right)\left(\frac{2x}{c}\right) \cos \phi \end{aligned} \quad (13)$$

In the current version of the code, the effect of pitching ( $q$ -term) has not been implemented. On a circular fuselage, the condition is

$$\frac{\partial \phi}{\partial r} + \frac{\partial \phi}{\partial r} = \beta \sin \theta - \left(\frac{rb}{2V_\infty}\right)\left(\frac{2x}{b}\right) \sin \theta \quad (14)$$

To satisfy these boundary conditions, two types of flow singularities are used in the program: horseshoe vortices representing lifting surfaces and vortex multiplets for the fuselage. To sum the effect of horseshoe vortices, the QVLM methodology is used to account for mathematical singularities of the square-root type at the leading edges and the Cauchy type. A two-dimensional formulation will be used to illustrate these points in the next section.

For the fuselage effect, G. N. Ward's vortex multiplets are distributed along the fuselage axis (ref.12). The velocity potential is given by

$$\Phi_f(x, \theta, r) = -\frac{1}{4\pi} \sum_n \left\{ \begin{array}{l} \cos n\theta \\ \sin n\theta \end{array} \right\} \int_{x_{fl}}^{x_{ft}} \frac{[x - \xi + \sqrt{(x - \xi)^2 + \beta^2 r^2}]^n}{r^n \sqrt{(x - \xi)^2 + \beta^2 r^2}} f_n(\xi) d\xi \quad (15)$$

where  $\cos n\theta$  is for the longitudinal case and  $\sin n\theta$  is for the lateral-directional case. When Equation (15) is substituted into Equation (10) or (14), it appears that the latter can be decomposed into Fourier components if the wing effect,  $\frac{\partial \Phi_w}{\partial r}$ , is also decomposed likewise. Let

$$\frac{\partial \Phi_w}{\partial r} = \sum_{n=1} a_n \left\{ \begin{array}{l} \cos n\theta \\ \sin n\theta \end{array} \right\} \quad (16)$$

Then, the Fourier coefficients are given by

$$a_n = \frac{2}{\pi} \int_0^\pi \left( \frac{\partial \Phi_w}{\partial r} \right) \left\{ \begin{array}{l} \cos n\theta \\ \sin n\theta \end{array} \right\} d\theta \quad (17)$$

This concept is implemented by calculating the normal velocity on the fuselage circumference induced by the wing vortex distribution at a number of fuselage stations and performing numerical integration of Equation (17). This method of Fourier component matching in satisfying the fuselage boundary condition has the advantage of requiring a much lower number of flow singularities in the solution process.

It should be noted that when a combination of surface and axial vortex distributions is used, the wing loading may become too low at the wing-fuselage juncture due to the horseshoe-vortex discretization of wing vortex distributions. This problem is solved in the present code, under the symmetrical loading condition, by eliminating the inboard trailing vortices associated with the root vortex strip. This idea is still correct even if the fuselage is absent. If this is not done, the root vortex strip will exhibit a loading similar to that near the wing tip. However, this step is not needed for the antisymmetrical case in the lateral-directional motion.

Detailed expressions for the induced velocity vector to be used in the boundary conditions can be found in reference 10 for lifting surfaces and reference 13 for a body. Note that the wake of the lifting surfaces is assumed to be flat.

### 2.2.2 Calculation of Leading-Edge Suction

To illustrate the essential idea of QVLM, consider a thin airfoil in a two-dimensional flow. The induced velocity at  $x$  on the chord line is

$$w(x,0) = -\frac{1}{2\pi} \int_0^1 \frac{\gamma(\xi)d\xi}{x-\xi} \quad (18)$$

The integrand in Equation (18) possesses a Cauchy singularity at  $\xi = x$ . In addition,  $\gamma(\xi)$  has a square-root singularity at  $\xi = 0$ . To eliminate the square-root singularity, the  $x$ -coordinate is transformed to a  $\theta$ -coordinate through the following relation:

$$x = \frac{(1 - \cos\theta)}{2} \quad (19)$$

$$\xi = \frac{(1 - \cos\theta')}{2} \quad (20)$$

Therefore, Equation (18) becomes

$$w(\theta) = \frac{1}{2\pi} \int_0^\pi \frac{\gamma(\theta')\sin\theta'd\theta'}{\cos\theta - \cos\theta'} \quad (21)$$

Let

$$g(\theta) = \gamma(\theta)\sin(\theta) \quad (22)$$

Since  $\gamma(\theta)$  has a square-root singularity at  $\theta = 0$  and  $\sin\theta$  vanishes at  $\theta = 0$  as the square root of  $x$ , the square-root singularity of  $\gamma(\theta)$  is eliminated by the factor  $\sin\theta$ . Equation (21) can be written as

$$w(\theta) = \frac{1}{2\pi} \int_0^\pi \frac{g(\theta') - g(\theta)d\theta}{\cos\theta - \cos\theta'} \quad (23)$$

Equation (23) can now be reduced to a finite sum through the midpoint trapezoidal rule as follows:

$$w(x_i) = \frac{-1}{2N} \sum_k \frac{\gamma_k x_k (1 - x_k)^{1/2}}{x_i - x_k} + \begin{cases} NC & , i = 0 \\ 0 & , i \neq 0 \end{cases} \quad (24)$$

$$x_i \text{ at } \theta_i = i\pi/N$$

$$x_k \text{ at } \theta_k = (2k - 1)\pi/2N$$

where C is related to a frequently-used leading-edge singularity parameter C'

$$C' = \lim_{x \rightarrow 0} u(x)\sqrt{x} = \lim_{x \rightarrow 0} \frac{1}{2} \gamma(x)\sqrt{x} = \frac{C}{2} \quad (25)$$

and can be computed once  $\gamma_k$ 's are obtained.

In a three-dimensional flow, the wing surface is divided into vortex strips. Over each vortex strip, the vortex integral is reduced to a finite sum in exactly the same manner as in the thin airfoil case described above with the leading-edge singularity parameter C calculated from the following relation (ref. 10):

$$\overline{NC\sqrt{\tan^2 \Lambda_\ell + \beta^2}} = \int \text{induced upwash at l.e.} \\ - \left[ \cos \phi \frac{\partial z_c}{\partial x} \cos \alpha - \cos \phi \sin \alpha \right] \quad (26)$$

The sectional leading-edge thrust coefficient ( $c_t$ ) is then given by

$$c_t = \frac{\pi C^2 \sqrt{1 - M_\infty^2 \cos^2 \Lambda_\ell}}{2 \cos \Lambda_\ell} \quad (27)$$

### 2.2.3 Pressure Distribution and Total Force and Moment Calculation

In the linearized theory of both compressible and incompressible flow, the wing pressure coefficient ( $C_p$ ) is related

to  $u$  in the expression

$$C_p = -2 \frac{u}{V_\infty} \quad (28)$$

In the thin wing theory, the vortex density function  $\gamma_y$  equals  $-2 \frac{u}{V_\infty}$ . Therefore, the lifting pressure is given by

$$\Delta C_p = 2\gamma_y \quad (29)$$

At any angle of attack, the pressure difference can be shown as (ref. 11)

$$\Delta C'_p = \cos(\alpha + \alpha_{tw} - \delta_c) \cdot 2\gamma_y \quad (30)$$

where  $\delta_c$ , equal to  $\tan^{-1} \left( \frac{dz}{dx_2} \right)$ , is the angle of the camber slope of the surface relative to the chord line.

For a cambered wing, additional lifting pressure will be generated from the interaction of a freestream component with the streamwise vortex density  $\gamma_x$ . Adding this component of lifting pressure to  $\Delta C'_p$ , the lifting pressure coefficient becomes (ref.11)

$$\Delta C''_p = \cos(\alpha + \alpha_{tw} - \delta_c) \cdot 2\gamma_y - 2\gamma_x \sin\alpha \sin(\phi + \phi_y) \quad (31)$$

where  $\phi$  is the dihedral angle,  $\phi_y = \tan^{-1} \left( \frac{dz}{dy_2} \right)$ .

With the pressure distribution calculated, the sectional force coefficient in potential flow can be calculated by chordwise integration as

$$c_{l,p} = \frac{1}{c} \int_{x_{le}}^{x_{te}} \Delta C''_p \left[ \frac{\partial z}{\partial x} \sin\alpha + \cos\alpha \right] / \left[ 1 + \left( \frac{\partial z}{\partial x} \right)^2 + \left( \frac{\partial z}{\partial y} \right)^2 \right]^{1/2} dx \quad (32)$$

$$c_{d,p} = \frac{1}{c} \int_{x_{le}}^{x_{te}} \Delta C_p'' \left[ -\frac{\partial z_c}{\partial x} \cos \alpha + \sin \alpha \right] / \left[ 1 + \left( \frac{\partial z_c}{\partial x} \right)^2 + \left( \frac{\partial z_c}{\partial y} \right)^2 \right]^{1/2} dx \quad (33)$$

In an attached flow,  $c_{d,p}$  must be reduced with the leading-edge thrust. The total force coefficients are calculated by spanwise integration of sectional force coefficients as

$$C_{L,p} = \frac{2}{S} \int_0^{b/2} c_{l,p} c dy \quad (34)$$

$$C_{D,p} = \frac{2}{S} \int_0^{b/2} c_{d,p} c dy \quad (35)$$

The sectional pitching moment coefficient is

$$c_{m,p} = -\frac{1}{c^2} \int_{x_{le}}^{x_{te}} \Delta C_p'' (\Delta x + \Delta z \frac{\partial z_c}{\partial x}) / \left[ 1 + \left( \frac{\partial z_c}{\partial x} \right)^2 + \left( \frac{\partial z_c}{\partial y} \right)^2 \right]^{1/2} dx \quad (36)$$

where  $\Delta x$  and  $\Delta z$  are the moment arms of the horseshoe vortex elements. Therefore, the total pitching moment coefficient in potential flow for a lifting surface is

$$C_{m,p} = \frac{2}{Sc} \int_0^{b/2} c_{m,p} c^2 dy \quad (37)$$

The pressure distribution on a body of revolution is computed by the following second-order formula:

$$C_{p(f)} = -2u - \left[ (1 - M_\infty^2)u^2 + v^2 + w^2 \right] \quad (38)$$

where  $u$ ,  $v$ , and  $w$  are nondimensional perturbed velocity components referred to the freestream velocity. Converting the velocity components  $u$ ,  $v$ , and  $w$  to cylindrical coordinates, Equation (38) becomes

$$C_{p(f)} = 1 - (1 + u)^2 + M_\infty^2 u^2 + \left( \cos \alpha \frac{dR}{dx} \right)^2 + \left( \frac{1}{r} \frac{\partial \Phi}{\partial \theta} - \sin \alpha \sin \theta \right)^2 \quad (39)$$



where the  $dR/dx$ -term is obtained with Equation (10) for the normal induced velocity on the body surface. The fuselage sectional normal force coefficients can be calculated by integration along the circumference as

$$c_{n(f)} = -\frac{1}{r} \int_0^{2\pi} C_p(f) \cos\theta r d\theta = -2 \int_0^{\pi} C_p(f) \cos\theta d\theta \quad (40)$$

By integrating the sectional normal force coefficients along the fuselage, the total normal force can be calculated:

$$C_{N(f)} = \frac{1}{S} \int_{x_{f\ell}}^{x_p} r c_{n(f)} dx \quad (41)$$

where  $x_p$  is the fuselage station behind which the potential flow does not exist (ref. 14).

Similarly, the fuselage moment coefficient can be obtained from

$$C_{m(f)} = -\frac{1}{S_c} \int_{x_{f\ell}}^{x_p} r c_{n(f)} x dx \quad (42)$$

## 2.3 Vortex Flow Theory

### 2.3.1 A Generalized Suction Analogy

Experiments show that for a low aspect-ratio wing with sharp leading edges, the flow always separates from the leading edge and rolls up into spiral vortex sheets and reattaches inboard of the vortex sheets. A typical flow field of leading edge vortex is shown in Figure 4. Due to this kind of flow separation, the pressure distribution on a low aspect-ratio wing is different from that given by the thin wing theory. In the method of suction analogy (ref. 15),

if the flow over the vortex sheets reattaches, the vortex lift on the wing is assumed to be the same as the leading edge suction force in attached flow. Such vortex separation also occurs along the tips (ref. 16). Therefore, it is essential to be able to predict accurately the leading-edge and side-edge suction coefficients.

To calculate the sectional leading-edge suction coefficient ( $c_s$ ), note that the suction force is the force which is normal to the leading edge, while the leading-edge thrust is the force in the x-z plane. The leading-edge thrust coefficient is calculated with Equation (27). For a plane wing, the sectional suction coefficient ( $c_s$ ) is related to the thrust coefficient ( $c_t$ ) as

$$c_s = c_t / \cos \Lambda_\ell \quad (43)$$

For a cambered wing with dihedral ( $\phi$ ), the relation is more complicated. The latter was derived in Reference 11 and is given as

$$c_s = c_t \frac{\sqrt{1 + \left(\frac{\partial z_c}{\partial x}\right)^2 + \left(\frac{\partial z_c}{\partial y}\right)^2} \left|\frac{d\vec{r}}{dy}\right|}{\left\{ \left[ \frac{\partial z_c}{\partial x} \frac{dz_\ell}{dy} + 1 \right]^2 + \left[ -\frac{\partial z_c}{\partial x} + \frac{\partial z_c}{\partial y} \tan \Lambda_\ell \right]^2 \right\}^{1/2}} \quad (44)$$

where

$$\frac{dz_\ell}{dy} = \frac{\partial z_c}{\partial x} \tan \Lambda_\ell + \frac{\partial z_c}{\partial y} \quad (45)$$

and

$$\left|\frac{d\vec{r}}{dy}\right| = \sqrt{1 + \tan^2 \Lambda_\ell + \left(\frac{dz_\ell}{dy}\right)^2} \quad (46)$$

The side-edge suction coefficient will be given later, as it is an essential parameter in lateral-directional aerodynamics.

In addition, when the leading-edge vortex system passes over an area downstream of the leading-edge tip, additional vortex lift is developed. This additional lift is called the augmented vortex lift (ref. 16). To derive an expression for the latter, consider the geometry in Figure 5. If the total vortex lift produced along the strake leading edge is equated to the force due to momentum transfer, then

$$\begin{aligned} -\int \frac{1}{2} \rho V_{\infty}^2 c_s c dy &= \int \rho V_v (\vec{V}_v \cdot d\vec{A}) \\ &= -\int 2\rho V_v (V_v r_{av} d\ell) \end{aligned}$$

It follows that

$$r_{av} = \frac{V_{\infty}^2}{4V_v^2 \ell} \int c_s c dy \quad (47)$$

where  $\ell$  is the leading-edge length over which the vortex lift is generated. If the augmented vortex lift ( $F_a$ ) is assumed to be the force produced by momentum transfer over a length ( $\tilde{c}$ ) as shown in Figure 5, then

$$\begin{aligned} F_a &= C_{L(aug)} \frac{1}{2} \rho V_{\infty}^2 S = 2\rho V_v (V_v \tilde{c} r_{av}) \\ &= \frac{1}{2} \rho V_{\infty}^2 \frac{\tilde{c}}{\ell} \int c_s c dy \end{aligned}$$

Therefore, the augmented vortex lift coefficient is given by

$$C_{L(aug)} = \frac{\tilde{c}}{\ell} C_{L(v, \ell e)} \quad (48)$$

where

$$C_{L(v, \ell e)} = \frac{1}{S} \int c_s c dy \quad (49)$$

The sectional aerodynamic characteristics due to the leading-edge vortex are given as follows:

$$c_{l,vle} = c_s \left( \frac{\partial z_c}{\partial x} \sin \alpha + \cos \alpha \right) / \left[ 1 + \left( \frac{\partial z_c}{\partial x} \right)^2 + \left( \frac{\partial z_c}{\partial y} \right)^2 \right]^{1/2} \quad (50)$$

$$c_{d,vle} = c_s \left( - \frac{\partial z_c}{\partial x} \cos \alpha + \sin \alpha \right) / \left[ 1 + \left( \frac{\partial z_c}{\partial x} \right)^2 + \left( \frac{\partial z_c}{\partial y} \right)^2 \right]^{1/2} \quad (51)$$

$$c_{m,vle} = - \frac{c_s}{c} \left( \Delta x_{le} + \Delta z_{le} \frac{\partial z_c}{\partial x} \right) / \left[ 1 + \left( \frac{\partial z_c}{\partial x} \right)^2 + \left( \frac{\partial z_c}{\partial y} \right)^2 \right]^{1/2} \quad (52)$$

Therefore, the total aerodynamic characteristics due to the leading-edge vortex are

$$C_{L,vle} = \frac{2}{S} \int_0^{b/2} c_{l,vle} c dy \quad (53)$$

$$C_{D,vle} = \frac{2}{S} \int_0^{b/2} c_{d,vle} c dy \quad (54)$$

$$C_{m,le} = \frac{2}{Sc} \int_0^{b/2} c_{m,vle} c^2 dy \quad (55)$$

### 2.3.2 Effect of Leading-Edge Radius on Vortex Separation

Kulfan assumed that on a slender wing the leading-edge vortex separation starts at an angle of attack ( $\alpha_s$ ) at which the leading-edge drag equals the leading-edge thrust (refs. 17 and 18). This condition has been shown to be consistent with the angle of attack at which the leading-edge laminar separation first occurs (ref. 19). To calculate  $\alpha_s$ , consider a cambered wing. The sectional leading-edge suction coefficient can be written as

$$c_s = K(\sin \alpha + \alpha_0)^2 \quad (56)$$

where  $K$  is a function of geometry and Mach number, and  $\alpha_o$  is the sectional angle of zero lift. For a wing, the sectional leading-edge thrust coefficient was given in Equation 27. The leading-edge singularity parameter at any  $\alpha$  can be written as

$$C = K'(\sin\alpha + \alpha_o) \quad (57)$$

Therefore, the leading-edge singularity parameter  $C_1$  at  $\alpha_s$  is obtained as

$$C_1 = C(\sin\alpha_s + \alpha_o)/(\sin\alpha + \alpha_o) \quad (58)$$

The starting angle of attack ( $\alpha_s$ ) of the leading-edge vortex separation can be obtained by equating the leading-edge drag to the leading-edge thrust. Using the expression for the leading-edge drag from reference 20, it is obtained that

$$\pi \frac{r_o}{c} \frac{\cos\Lambda_\ell}{(1 - M_\infty^2 \cos^2 \Lambda_\ell)^{1/2}} = \frac{\pi}{2} C^2 \frac{(\sin\alpha_s + \alpha_o)^2}{(\sin\alpha + \alpha_o)^2} \frac{(1 - M_\infty^2 \cos^2 \Lambda_\ell)^{1/2}}{\cos\Lambda_\ell} \quad (59)$$

where  $r_o$  is the leading-edge radius. It follows that

$$\alpha_s = \sin^{-1} \left[ \pm \frac{\sin\alpha + \alpha_o}{C} \left( 2 \frac{r_o}{c} \right)^{1/2} \cos\Lambda_\ell / (1 - M_\infty^2 \cos^2 \Lambda_\ell)^{1/2} - \alpha_o \right] \quad (60)$$

With  $\alpha_s$  calculated, the sectional thrust coefficient at  $\alpha > \alpha_s$  is given by

$$c_t = (\pi/2) C_2^2 (1 - M_\infty^2 \cos^2 \Lambda_\ell)^{1/2} / \cos\Lambda_\ell \quad (61)$$

where

$$C_2 = C[\sin(\alpha - \alpha_s) + \alpha_o]/(\sin\alpha + \alpha_o) \quad (62)$$

This sectional thrust coefficient is converted into the vortex lift coefficient through the suction analogy. From Equation (62), it can

be seen that the effect of a rounded leading edge is to decrease the vortex lift at an  $\alpha > \alpha_s$ .

### 2.3.3 Concept of Vortex Action Point

In developing the concept of the vortex action point, the linear momentum principle of fluid mechanics is used. It is assumed that the velocity distribution around the vortex in the longitudinal plane parallel to the freestream is similar to that in the cross-flow plane (Fig. 6). If a control surface  $\sigma$  is taken through the vortex center as shown in Figure 7, the vortex force should be equal to the vertical component of the force due to the momentum transfer through the control surface  $\sigma$ . As shown previously, the vortex force acting on the wing is  $\frac{1}{2} \rho V_\infty^2 c c_s$ . It follows that the force acting on the control volume is

$$-\frac{1}{2} \rho V_\infty c c_s = \int_{\sigma} \rho V_z (\vec{V} \cdot d\vec{\tau}) = \int_{\sigma} (\rho V_{z_{in}} - \rho V_{z_{out}}) \vec{V} \cdot d\vec{\tau} \quad (63)$$

To find an average  $V$ , let

$$|V| = V_z = fV_\infty \quad (64)$$

where  $f$  is a constant. Therefore for a unit span

$$\begin{aligned} \int (\rho V_{z_{in}} - \rho V_{z_{out}}) \vec{V} \cdot d\vec{\tau} &= -fV_\infty \left[ \int \rho V_{z_{in}} d\tau + \int \rho V_{z_{out}} d\tau \right] \\ &= -fV_\infty 2\rho (fV_\infty) r_v \end{aligned} \quad (65)$$

where  $r_v$  is the location of the vortex action point from the leading edge. From Equations (63) and (65) it is found that

$$r_v = \frac{1}{4f^2} c c_s \quad (66a)$$

In the program,  $f$  is determined to be 0.5 for subsonic flow (ref.

11). Therefore, the action point location ( $r_v$ ) is

$$r_v = c c_s \quad (66b)$$

#### 2.3.4 Effect of Vortex Breakdown

The effect of vortex breakdown is one of the important factors affecting the aerodynamics of high performance aircraft. Since there is no comprehensive theory to predict the breakdown location and the residual vortex strength after breakdown, a semi-empirical formula derived from a least-square analysis of available data is used in the program.

Lamar (ref. 16) observed that for delta wings, the angles of attack for vortex breakdown at the trailing edge ( $\alpha_{BD}$ ) is related to the leading-edge suction distribution ( $c_s$ ). Let

$$\bar{c}_s = c c_s / \bar{c} \sin^2 \alpha \quad (67)$$

where  $\bar{c}$  is the mean aerodynamic chord (MAC). Since  $c_s$  is proportional to  $\sin^2 \alpha$ , it follows that  $\bar{c}_s$  is a function of planform and Mach number. From a least-square analysis of Wentz's data (ref. 21), it was found that  $\alpha_{BD}$ , expressed in degrees, would fall on a single curve described as follows:

$$\alpha_{BD} = 9.195 - 23.734\bar{y}_\ell + 60.810\bar{y}_\ell^2 - 33.533\bar{y}_\ell^3 + 7.391\bar{y}_\ell^4 - 0.581\bar{y}_\ell^5,$$

$$\text{if } \bar{y}_\ell < 2.5 .$$

$$\alpha_{BD} = 38.0, \text{ if } \bar{y}_\ell > 2.5 \quad (68)$$

where  $\bar{y}_\ell$  is the distance from apex to centroid of the  $\bar{c}_s$  distribution from inboard to  $\eta$  of  $\bar{c}_{s(\max)}$  measured along the leading edge and referred to the half span. This is illustrated in Figure 8a.

The progression rate of the breakdown point on delta wings at  $\alpha > \alpha_{BD}$  was also analyzed based on Wentz's data. Although there was considerable scatter in the experimental data (Fig. 8b), a single curve based on a least-square analysis was obtained to be

$$\begin{aligned} \Delta\bar{x} = & 0.457(\Delta\alpha) - 1615(\Delta\alpha)^2 + 0.0303(\Delta\alpha)^3 - 0.0027(\Delta\alpha)^4 \\ & + 0.00009(\Delta\alpha)^5, \text{ if } \Delta\alpha < 8.0 \text{ deg.} \end{aligned} \quad (69)$$

$$\Delta\bar{x} = 0.5392 + 0.0226(\Delta\alpha), \text{ if } \Delta\alpha \geq 8.0 \text{ deg.}$$

where  $\Delta\alpha = \alpha - \alpha_{BD}$  and  $\Delta\bar{x}$  is the nondimensional x-distance, referred to the root chord, from the trailing edge to the breakdown point.

It is known that the vortex strength after breakdown is reduced but not vanished. In the VORSTAB code, the sectional  $c_{gc}$  at any station where vortex breakdown occurs is multiplied by a factor  $k$  to represent the residual vortex lift. The factor  $k$  is determined, again, by analyzing Wentz's data and is found to be (ref. 22)

$$\begin{aligned} k = & 0.131 + 0.384\bar{y}_\ell, \text{ if } \bar{y}_\ell < 1.49 \\ k = & 0.951 - 0.208\bar{y}_\ell + 0.028\bar{y}_\ell^2, \text{ if } 1.49 \leq \bar{y}_\ell < 3.71 \\ k = & 0.5, \text{ if } \bar{y}_\ell \geq 3.72 \end{aligned} \quad (70)$$



In addition, it was found that upper surface slopes in the spanwise direction due to thickness distribution will affect the movement of the burst point (ref. 23). To model this effect, it is assumed that the local angle of attack is changed by an amount equal to the spanwise upper surface angle; i.e.,  $\tan^{-1}(\partial z/\partial y)$ . The new local angle of attack is used in Equation (69) to determine the vortex burst point iteratively because  $\partial z/\partial y$  is, in general, not a constant. This effect was found to be quite significant for a highly cambered wing, such as the F-106B configuration.

#### 2.3.5 Fuselage Vortex Lift

If the aspect ratio of a slender thick wing is reduced, eventually it becomes a slender body. If the method of suction analogy is applicable to the former, it should also be applicable to the latter. Based on this assumption, the following method for calculating body vortex lift was developed. The method is based on the following assumptions and procedures.

1. As mentioned previously, the attached flow solution is obtained with the axial distribution of G. N. Ward's vortex multiplets.
2. At any axial station, vortex separation starts at a  $\theta$ -circumference location where  $C_p$  is minimum and negative. This assumption has been shown to be reasonable (ref. 24). At low angles of attack,  $C_p$  may be positive everywhere near the nose. In this case, no vortex

separation is assumed to occur. In reference 24, the axial station ( $x_s$ ) at which the vortex separation starts must be assumed or given by experiments.

3. At any axial station, the side force component of the negative  $C_p$  in the region assumed to have vortex separation is integrated to produce a sectional side force coefficient (see Fig. 9):

$$c_{sf} = \frac{1}{r(x)} \int r(x) C_p \sin(\theta) d\theta \quad (71)$$

The obtained side force is assumed to be the suction force produced by the separated vortex. This suction force is presumed to be acting at  $\theta_c$  (Fig. 10) where

$$\theta_c = \theta_{\min,p} - \Delta\theta \quad (72)$$

$$\Delta\theta = h c_{sf} \quad (73)$$

Equations (72) and (73) imply that the vortex action point is located at a distance from  $\theta_{\min,p}$  being proportional to the suction force. Therefore,

$$\Delta s = r \Delta\theta = h r c_{sf} \quad (74)$$

Based on Equation (66a),  $h$  becomes

$$h = 1/(4f^2) \quad (75)$$

In reference 25,  $f$  is determined to be  $1/\sqrt{2}$  in subsonic flow. Therefore,  $h = 0.5$  is used in the program.

With  $\theta_c$  calculated from Equation (72), sectional normal force coefficient due to the vortex is given by

$$c_{N,v} = c_{sf} \cos\theta_c \quad (76)$$

4. Similar to a wing, the augmented body vortex lift exists whenever the planview of a body is not of the delta type. Therefore, the concept employed in calculating the augmented vortex lift for a wing is also applicable for a body. Thus, if  $C_{sf,N}$  is the total suction force coefficient from the nose portion, the augmented normal force coefficient  $C_{N,VA}$  is given by

$$C_{N,VA} = \tilde{c} C_{sf,N} \cos \theta_A / \ell_n \quad (77)$$

where  $\tilde{c}$  is the length over which the nose vortex passes and  $\ell_n$  is the nose length. Note that  $\theta_A$  is the location of augmented vortex action point and is assumed to be equal to  $\theta_c$  at the body shoulder. Some calculated results for the body vortex lift in both subsonic and supersonic flows can be found in Reference 25.

#### 2.4 Effect of Boundary Layer Separation

It is known that the classical lifting line theory cannot be used for most lifting surfaces of fighter configurations because of limitations of the theory on aspect ratios and sweep angles of lifting surfaces. Furthermore, existing methods for calculating stall and post-stall characteristics of lifting surfaces are not satisfactory, particularly for thin wings used on fighter configurations. To improve the prediction methodology, a method based on utilizing nonlinear section data was developed (ref. 9).

In this method, the nonlinear sectional data was used as near-field solutions to be matched iteratively with far-field solutions obtained from the lifting surface theory. Based on this concept, it is assumed that the effect of flow separation is to reduce the local angle of attack by  $\Delta\alpha$  at a spanwise station. Therefore, the effective angle of attack at any spanwise section becomes

$$\alpha_e = \alpha_n - \alpha_i - \alpha_o - \Delta\alpha \quad (78)$$

where  $\alpha_n$  is the geometric angle normal to the section which may have dihedral,  $\alpha_i$  is the induced angle of attack,  $\alpha_o$  is the angle of zero lift, and  $\Delta\alpha$  represents a reduction in  $\alpha_n$  to be calculated due to viscous effects. It follows that

$$c_{\ell(3-D)} = c_{\ell\alpha} \sin(\alpha_n - \alpha_i - \alpha_o - \Delta\alpha) \quad (79)$$

Assuming  $c_{\ell\alpha} = 2\pi/(1 - M_\infty^2)^{1/2}$ , Equation (78) can be solved for  $\alpha_i$ :

$$\alpha_i = \alpha_n - \sin^{-1} \left[ \frac{c_{\ell(3-D)}}{c_{\ell\alpha}} \right] - \alpha_o - \Delta\alpha \quad (80)$$

Let the 2-D sectional lift coefficient evaluated at  $\alpha_n - \alpha_i$  be  $c_{\ell(2-D)}$  and let

$$f = \frac{c_{\ell(2-D)}}{c_{\ell(3-D)}} \quad (81)$$

Since  $c_{\ell(3-D)}$  is computed with an inviscid theory, its value is usually larger than  $c_{\ell(2-D)}$  if  $\Delta\alpha = 0$ . Therefore,  $f$  is usually less than 1.0. In this case, a geometric angle of attack ( $\alpha'$ ) which produces the reduced lift can be found. That is,

$$\sin\alpha' = f \sin\alpha_n$$

or,

$$\alpha' = \sin^{-1}(f \sin \alpha_n) \quad (82)$$

It follows that  $\Delta\alpha$  in Equation (78) becomes

$$\Delta\alpha = \alpha_n - \alpha' \quad (83)$$

The solution is obtained iteratively as follows:

1. Assume  $\Delta\alpha = 0$ .
2. Find  $\alpha_i$  from Equation (80).
3. Calculate  $f$  from Equation (81).
4. Determine  $\Delta\alpha$  from Equations (82) and (83).
5. Use  $\Delta\alpha$  to reduce  $\alpha$  in the 3-D boundary condition to determine  $c_{l(3-D)}$ .
6. Repeat steps 2 through 5 until the successive total lift coefficients differ by less than 0.5%.

For a configuration of moderate aspect ratio with vortex lift, the iterative procedures described above are not started until the predicted vortex breakdown occurs. Before vortex breakdown, the viscous effect is accounted for only once without iteration. The latter procedure is also used in calculating lateral-directional aerodynamics. That is, lateral-directional aerodynamic characteristics are calculated without iteration only after the calculation for longitudinal characteristics has converged. In addition, when a wing with a separated flow is subjected to a positive sideslip or roll rate, part of the left-wing separated region may be reduced or suppressed because of reduced loading. Therefore, the reduced lift due to separation may be recovered. This effect of lift recovery will make the resulting roll moment less negative and is included in the code.

Based on experience, this method is applicable to most of the current fighter configurations. However, if the lifting surfaces are dominated by vortex flow, such as the F-106B configuration, inviscid flow should be assumed.

## 2.5 Calculation of Lateral-Directional Stability Derivatives in Attached Flow

The lateral-directional stability derivatives to be discussed in this study are  $\beta$ -,  $p$ -, and  $r$ -derivatives.

### 2.5.1 $\beta$ -Derivatives ( $C_{y\beta}$ , $C_{n\beta}$ , and $C_{\ell\beta}$ )

The distribution of lifting pressure coefficients in sideslip can be written as

$$\Delta C_p = 2(\gamma_y + \gamma_x \sin\beta) \quad (84)$$

Therefore, for small sideslip angles,

$$C_{\ell\beta} = \frac{\partial C_{\ell}}{\partial \beta} = -\frac{2}{Sb} \int \left( \frac{\partial \gamma_y}{\partial \beta} + \gamma_x \right) \cos\theta y \, dy \quad (85)$$

where  $\theta$  is the camber angle.

To compute the wing contribution to  $C_{y\beta}$  and  $C_{n\beta}$ , the leading-edge and side edge suction force components due to sideslip must be calculated. The side-edge suction force per unit length is given as (ref. 13)

$$S_t(x) = \pi\rho G^2(x) \quad (86)$$

where  $G(x)$  is the singularity parameter of circulation  $\Gamma_t(y)$  at the

tip and is related to  $\Gamma_t$  by

$$G(x) = \left(\frac{b}{2}\right)^{1/2} \lim_{y \rightarrow \frac{b}{2}} \left(1 - \frac{y}{b/2}\right)^{1/2} \frac{1}{2} \frac{\partial \Gamma_t}{\partial y} \quad (87)$$

For the antisymmetrical case, the total side-edge suction force can be written as

$$S_t(x) = \pi \rho (G_\alpha \pm G_a)^2 \quad (88)$$

where the plus sign is for the right wing and the minus sign for the left wing, with subscripts  $\alpha$  and  $a$  denoting symmetrical and antisymmetrical cases, respectively.

The sectional leading-edge thrust coefficient in combined symmetrical and antisymmetrical loading can be written as (ref. 13)

$$c_t = \frac{\pi}{2} \frac{(C_\alpha \pm C_a)^2}{\sqrt{1 - M_\infty^2 \cos^2 \Lambda_\ell} \cos \Lambda_\ell} \quad (89)$$

where  $C_\alpha$  and  $C_a$  are leading-edge singularity parameters, for symmetrical and antisymmetrical loading, respectively. If  $C_a$  due to sideslip is denoted by  $C_{a\beta}$  and  $c_t$  due to sideslip only is  $\Delta c_{x\beta}$ , then the leading-edge thrust coefficient due to sideslip is given by

$$\Delta c_{x\beta} = \frac{\pi}{2} \frac{2C_\alpha C_{a\beta}}{\sqrt{1 - M_\infty^2 \cos^2 \Lambda_\ell} \cos \Lambda_\ell} \quad (90)$$

Therefore, the wing side force due to leading-edge suction in sideslip is

$$\Delta c_{y\beta} = \Delta c_{x\beta} \tan \Lambda_\ell \quad (91)$$

The total wing side force due to sideslip contains four sources:

1. Contribution from the side-edge suction

The side force along the side edge is

$$S_t = \pi\rho(G_\alpha \pm G_a)^2 \quad (92)$$

Therefore,

$$\frac{\partial S_t}{\partial \beta} = 2\pi\rho G_\alpha \left(\pm \frac{\partial G_a}{\partial \beta}\right) \quad (93)$$

2. Contribution from the leading-edge suction

$$\Delta C_{y_\beta} = \frac{2}{S} \int_{\text{right wing}} c(y) \Delta c_{y_\beta} dy \quad (94)$$

3. Contribution from the incremental pressure force due to geometric dihedral

The incremental lifting pressure force, which acts normal to a planform, has components in the side force direction. The contribution to  $C_{y_\beta}$  can be calculated by integrating sectional contributions.

4. Contribution from the induced drag

The induced drag is assumed to act in the direction of the freestream with sideslip. For small sideslip angles, the side force due to the induced drag can be computed as

$$\Delta C_y = -C_{D_i} \beta$$



It follows that

$$\Delta C_{y\beta} = -C_{D_i} \quad (95)$$

The fuselage contribution to the side force coefficient can be computed as

$$C_{y(f)} = \frac{1}{S} \int_{x_{fl}}^{x_p} r c_{y(f)} dx \quad (96)$$

where  $c_{y(f)}$  is the fuselage sectional side force coefficient. The contribution to  $C_{y\beta}$  is obtained by differentiating Equation (96) with  $\beta$ .

The yawing moment coefficients due to sideslip are obtained by taking moment of all the side force components about the z-axis.

### 2.5.2 p-Derivatives ( $C_{y_p}$ , $C_{n_p}$ , and $C_{l_p}$ )

The roll damping derivative  $C_{l_p}$  is computed by integrating the antisymmetrical pressure force induced by the roll rate multiplied by the spanwise moment arm. The side force and yawing moment due to roll rate are contributed from the following sources:

1. Contribution from the leading-edge suction

The incremental sectional leading-edge thrust coefficient due to roll rate is

$$\Delta c_{x_p} = \frac{\pi}{2} \sqrt{1 - M_\infty^2 \cos^2 \Lambda_\ell} \frac{2C_\alpha C_{a_p}}{\cos \Lambda_\ell} \quad (97)$$

Therefore,

$$\Delta c_{y_p} = \Delta c_{x_p} \tan \Lambda_\ell \quad (98)$$

$$\Delta C_{y_p} = \frac{2}{S} \int_{\text{right wing}} c(y) \Delta c_{y_p} dy \quad (99)$$

2. Contribution from the side edge suction

$$\frac{\partial S_t}{\partial p} = 2\pi\rho G_\alpha \left( \pm \frac{\partial G_{ap}}{\partial p} \right) \quad (100)$$

3. Contribution from the incremental pressure distribution

The concept described in relation to  $C_{y_\beta}$  is still applicable to  $C_{y_p}$ .  $C_{n_p}$  can be obtained by taking moment of all the side forces due to  $p$  about the  $z$ -axis.

2.5.3 r-Derivatives ( $C_{y_r}$ ,  $C_{n_r}$ , and  $C_{\ell_r}$ )

The yawing motion can change the pressure distribution on the lifting surfaces. The incremental pressure distribution due to yaw rate consists of three components:

1. Due to yaw rate  $r$ , a backwash ( $ry$ ) is produced (Fig. 11) where  $y$  is the spanwise station. Therefore,

$$\Delta C_{pr} = - \frac{ry}{V_\infty} \gamma_y \quad (101)$$

2. The sidewash ( $rx$ ) effect produces

$$\Delta C_{pr} = - \frac{rx}{V_\infty} \gamma_x \cos \phi \quad (102)$$

3. Wing-body interaction is calculated by satisfying the boundary conditions.

The calculation of  $C_{y_r}$  and  $C_{n_r}$  follows the same procedures as for computing  $C_{y_\beta}$  and  $C_{n_\beta}$ .

## 2.6 Lateral-Directional Aerodynamics in Vortex Flow

It is indicated in references 26 and 27 that in a sideslip the leading-edge vortex on the windward side is pushed inward and downward, thus inducing additional vortex lift, while on the leeward side it is pushed outward and upward, thus inducing less vortex lift. To account for the increase in vortex lift on the windward side, a "displacement-type" vortex lift is introduced. In addition, vortex breakdown characteristics are also different from those of the symmetrical flow situation. The flow mechanism and computational methods for sideslip, yawing, and rolling motions are described below.

### 2.6.1 Vortex Lift of the Displacement Type in Sideslip

The leading-edge singularity parameter, defined in Equation (25), is proportional to the lifting pressure coefficient. As shown in Equation (84), due to sideslip, an extra term,  $\gamma_x \sin\beta$ , is added to the lifting pressure coefficient in symmetric flow. Since the vorticity near the leading-edge must be parallel to the leading edge, it follows that

$$C_{(\beta)} = C_\alpha (1 \pm \tan\Lambda_\lambda \sin\beta) \quad (103)$$

The leading-edge thrust coefficient in sideslip becomes

$$c_{t(\beta)} = (\pi/2)C_{\alpha}^2(\pm \tan\Lambda_{\ell}\sin\beta + \tan^2\Lambda_{\ell}\sin^2\beta) \frac{(1 - M_{\infty}^2\cos^2\Lambda_{\ell})^{1/2}}{\cos\Lambda_{\ell}} \quad (104)$$

### 2.6.2 Vortex Lift of the Displacement Type in Yawing

The induced sidewash due to yawing is

$$\beta_r = -2 \frac{x - x_{ref}}{b} \bar{r} \quad (105)$$

Therefore, the leading-edge singularity parameter due to yawing becomes

$$C_{(r)} = C_{\alpha}(1 \pm \beta_r \tan\Lambda_{\ell}) \quad (106)$$

### 2.6.3 Vortex Breakdown in Sideslip

With a sideslip angle  $\beta$ , the angles of attack for vortex breakdown on the windward side ( $\alpha_{BR}$ ) and the leeward side ( $\alpha_{BL}$ ) are calculated as follows:

1. Calculate  $\bar{y}_{\ell}$  from the symmetrical suction distribution with the leading-edge sweep angles  $\Lambda_{\ell} - \beta$  for the right wing and  $\Lambda_{\ell} + \beta$  for the left wing.
2. Assume that the maximum vortex strength before breakdown is unchanged by sideslip. Because of increase in vortex lift on the right wing in a positive sideslip, the maximum vortex strength would be reached at a lower  $\alpha$  (i.e.,  $\alpha_{BR}$ )

than  $\alpha_{BD}$  on the right wing. Since the vortex strength is represented by  $c_s$  which is proportional to  $\sin^2 \alpha$ ,  $\alpha_{BR}$  and  $\alpha_{BL}$  can be obtained by solving the following equation:

$$\sin^2 \alpha_{BD} = \sin^2 \alpha_{BR} + (\pm 2 \sin \beta + \tan \Lambda_\ell \sin^2 \beta) \sin^2 \alpha_{BR} \quad (107)$$

where "-" is for  $\alpha_{BL}$ .

Similar to lift recovery in a viscous separated flow mentioned earlier, vortex lift recovery is also possible. When a slender wing is at an  $\alpha$  greater than  $\alpha_{BD}$  and at a positive sideslip, vortex breakdown on the left wing may be suppressed, thereby recovering the symmetrical vortex lift to make the rolling moment less negative.

#### 2.6.4 Vortex Breakdown in Yawing

The effect of yawing on vortex breakdown is similar to that due to sideslip. Since the equivalent sideslip ( $\beta_r$ ) is variable along the leading edge, the average of  $\beta_r$  at a given y station and that at the tip is used to determine breakdown  $\alpha$ . In the program,  $\alpha_{BL}$  for the yawing motion is determined by a linear interpolation between  $\alpha_{BD}$  and  $\alpha_{BR}$  for sideslip.

#### 2.6.5 Vortex Breakdown in Rolling

Due to a positive roll, the local angle of attack on the right wing is increased. It seems that the vortex breakdown angle would

be decreased. However, rolling tends to move the centroid of the vortex lift distribution outboard (i.e., to increase  $\bar{y}_l$ ). Therefore, the vortex breakdown angle is increased. In the present code, the vortex breakdown angle for the rolling motion is assumed to be equal to  $\alpha_{BD}$  for the symmetrical loading.

### 3. NUMERICAL RESULTS AND DISCUSSION

Earlier applications of the methods described herein can be found in reference 22 for simple slender wings and in reference 9 for two complete configurations of airplanes. For simple slender wings, the main objective was to show the effect of vortex breakdown. On the other hand, for the airplane configurations it was imperative to account for the effect of boundary-layer separation. For the latter, nonlinear section data including post-stall characteristics are required.

The performance of some theoretical methods for predicting airfoil characteristics up to stall has been reviewed by Blascovich in reference 28. Rumsey found another method (i.e. the SAAP) to be accurate in predicting  $c_{l_{max}}$  (ref. 29). These methods are typically good for moderate to thick airfoils with angles of attack up to the stall angle. At post-stall angles of attack and for thin airfoils typically used on fighter wings, these methods are all questionable. On a thin airfoil, the flow separation is usually of the long bubble type. The latter is not well predicted by existing methods. In view of the fact that all thin airfoils tend to behave

in the same way as a flat plate (refs. 30 and 31), for the present purpose it was decided to modify Eppler's code (ref. 32) by including a modified free-wake theory (ref. 31). Typically, a thin airfoil will stall at about 8 to 8.5 degrees of angle of attack. After stall, the variation of  $c_l$ ,  $c_d$ , and  $c_m$  with angles of attack is assumed to be given by the modified free-wake theory.

To obtain a better understanding in determining how an airplane configuration should be modeled for both longitudinal and lateral calculation, several existing fighter configurations were investigated. They are

- (a) An F/A-18 configuration with and without leading edge flap deflection.
- (b) A generic fighter model.
- (c) An F-16 configuration.
- (d) An F-16XL configuration.
- (e) The F-5 and modified configurations.
- (f) An X-29A forward swept wing airplane.
- (g) An F-106B configuration.

In the following, some calculated results will be presented.

(a) An F/A-18 Configuration

The F/A-18 configuration is relatively complicated in geometry. It has highly cambered strakes so that not only is the viscous separation effect important on the wing at high angles of attack but also the vortex lift is significant.

The geometric model of the F/A-18 used in the calculation is illustrated in Figure 12. Based on calculations with the modified Eppler's code, the sectional characteristics shown in Figure 13 were used in the VORSTAB calculation.

In these calculations, it is assumed that there is no boundary-layer separation on the strakes. The strake vortex was observed to pass through the lower surface of the vertical tails at angles of attack lower than 20 degrees (ref. 33). Thus the characteristic length for the augmented-vortex lift ( $\tilde{c}$ ) to be used is negative. However, at angles of attack greater than or equal to 20 degrees, the augmented-vortex lift on the vertical tails should be positive. Forebody vortex lift is assumed to exist. However, interaction of the forebody vortices with the vertical tails in the lateral-directional motion is not modeled in the present code. No additional discrete vortices are placed at the strake-wing juncture in the modeling for this configuration or for the F-16 to be discussed later.

Longitudinal characteristics without the leading-edge flap deflection are presented in Figure 14. It is seen that  $C_L$  is slightly underpredicted and  $C_m$  is more negative for angles of attack in the range of 15 to 30 degrees. This is perhaps caused by the predicted vortex breakdown being too early in  $\alpha$  and viscous separation on the wing. Because of a relatively low sweep angle (26 degrees), the wing is predicted to have vortex breakdown at an angle of attack of 12 degrees, instead of merely being displaced upwards due to the influence of strake vortices (ref. 35).



Lateral-directional coefficients  $C_{y\beta}$ ,  $C_{l\beta}$ , and  $C_{n\beta}$  of the same configuration are presented in Figure 15. At angles of attack below 15 degrees, the VORSTAB code was capable of predicting well the lateral-directional characteristics. However, discrepancy occurs at higher angles, most probably due to the strong strake vortex passing through the vicinity of the vertical tails. In a positive sideslip, the positive side force on the right vertical tail produced by the right strake vortex may be greater than the negative side force on the left vertical tail produced by the left vortex, thus generating a more negative  $C_{n\beta}$  and a more positive  $C_{l\beta}$  in the test results. Another possible reason is the effect of wing wake on the vertical tails (ref. 36). At present, these types of interference between lifting surfaces still can not be accurately predicted by the program.

To see the effect of leading-edge flaps, nonlinear section data are needed. The lift data are presented in Figure 16. Longitudinal characteristics are well predicted, as shown in Figure 17, except the pitching moment coefficients again are more negative at moderate angles of attack. Since the leading-edge flap will delay the wing separation effect,  $C_{n\beta}$  is now more positive due to the reduced effect of wing wake on the vertical tails and is shown to be more accurately predicted as shown in Figure 18. The discrepancy in  $C_{l\beta}$  is mainly due to the predicted vortex-breakdown  $\alpha$  of the wing in sideslip being inaccurate. They are 24.7 and 25.9 degrees for the right and left wings, respectively, compared with possible values of

20 and 30 degrees in the data. Of course, the strake vortex interaction again plays a role in the  $C_{l\beta}$  variation.

(b) A Generic Fighter Configuration

This is an airplane model tested in the 12-foot tunnel at NASA Langley Research Center (ref. 37). As shown in Figure 19, the model includes a cylindrical body with lifting and control surfaces made of flat plates. Nonlinear sectional data from reference 31 were used in the calculation (Fig. 20). In the calculation for the viscous effect, an overrelaxation factor was used for the wing. However, the horizontal tail required an underrelaxation factor to achieve convergence. This is most probably due to a coplanar wing-tail interaction. In this case, not only should the vortex strips on the wing and tail be lined up to avoid unrealistic downwash induced on the tail, but also the relaxation factor on the tail must be reduced to avoid divergence. Based on the experience with other configurations, an underrelaxation factor of 0.5 for both surfaces should also work well as an initial trial value. Because of a relatively long forebody, body vortex lift is assumed to exist in the calculation. This latter effect mainly affects the pitching moment calculation in the present code.

Longitudinal characteristics are presented in Figure 21. It is seen that the predicted results agree well with data, except that the predicted  $C_m$  is more negative. Sideslip derivatives are shown in Figure 22. At angles of attack greater than 22 degrees, both  $C_{n\beta}$

and  $C_{l_\beta}$  are not correctly predicted. This is probably due to the contribution of asymmetric forebody vortices to  $C_{n_\beta}$  at high  $\alpha$ . At a positive sideslip, the asymmetric forebody vortices tend to produce a positive side force near the nose and hence a more positive  $C_{n_\beta}$  for the whole configuration. The reason for the large change in  $C_{l_\beta}$  at  $\alpha > 25$  degrees is not precisely known and could be the result of interaction between asymmetric forebody vortices with the vertical tail.

(c) An F-16 Configuration

As seen in Figure 23, this airplane has a slender leading-edge extension (or strake). Also, the sectional data (Fig. 24) are used only on the wing. Body vortex lift is included in the calculation. Like other airplanes which have been modeled, there is no difficulty in modeling the lifting surfaces. However, the F-16 has a distinct inlet which makes the cross sections of an equivalent body of revolution change too rapidly. Note that only a body of revolution is allowed in the code. In addition, the inlet makes it more difficult for the predicted fuselage aerodynamic characteristics to be reasonable if the real body shape with the nacelle is used. Therefore, smooth body cross sections are assumed. As shown in Figure 25, the longitudinal characteristics are reasonably well predicted, up to an  $\alpha$  of 25°.

Unlike the F/A-18 configuration, the strake for the F-16 model was assumed noncambered and untwisted. Therefore, the predicted  $\alpha_{BD}$  was lower than that for the F/A-18 (31 vs 33

degrees). This might have affected the lift prediction at high  $\alpha$ . Another reason for the drop in  $C_L$  is that the k-factor for the strake could be too low (see Eq. 70). Note that an inviscid theory would overpredict the lift.

The strake of this configuration is not as large as the one on the F/A-18. Therefore, the influence of strake vortices on the vertical tail is not as significant. The predicted lateral characteristics agree well with the data, as shown in Figure 26.

(d) An F-16XL Configuration

This configuration (Fig. 27) consists of the fuselage and the horizontal tail of the F-16A and a highly swept cranked wing. As described in modeling the F-16A configuration, smooth body cross sections are assumed. The inboard and outboard leading-edge swept angles are 70 to 50 degrees, respectively. Because the vortex flow is expected to be strong, nonlinear sectional data were not used in the model. Body vortex lift is not modeled for this configuration.

Predicted results for longitudinal aerodynamics without viscous effect are shown in Figure 28. Again, the prediction agrees well with data. When sectional data were specified over the outboard portion of the cranked wing, the predicted lift coefficient was too low by about 14% at high  $\alpha$  (not shown in the figure). However, all other characteristics, including the lateral-directional parameters, were well predicted. Sideslip derivatives are presented in Figure 29. Except at  $\alpha \geq 30$  degrees, both  $C_{n_\beta}$  and  $C_{l_\beta}$  are accurately computed. At high  $\alpha$ , the

discrepancy is most likely caused by the burst vortex flow on the right side inducing positive side force on the vertical tail. The latter would produce more negative  $C_{n\beta}$  and positive  $C_{l\beta}$ . The predicted  $\alpha$  for vortex breakdown for the inboard portion of the wing in a positive sideslip ( $\alpha_{BR}$ ) is about 32 degrees.

(e) The F-5 and Modified Configurations

There are three wing configurations in this series of models: the basic F-5, an F-5 fuselage with a swept wing, and an F-5 fuselage with a delta wing (Figs. 30 and 31). The F-5 configuration is well known for its long forebody, which can generate strong forebody vortices. For strong wing-dominated vortex flow, the forebody vortex effect on longitudinal characteristics is minor compared with the wing vortex lift. On the other hand, for a moderate aspect-ratio wing, the body vortex may induce strong enough spanwise pressure gradient on the wing to delay vortex breakdown on the latter, in much the same way as a strake does.

In examining these three configurations, the swept angles of the basic and swept wing configurations are not large. Thus they do not have strong vortex lift effect and may be subjected to boundary separation which is influenced by the forebody vortices. Since there is no theoretical method available to determine the degree of influence exerted by the forebody vortex on the wing flow field, at the present time this can only be done empirically.

The basic assumption made in this regard is that the forebody vortex is to produce a favorable pressure gradient on the wing to delay vortex breakdown and the fuselage downstream of the wing

leading edge is to cause earlier vortex breakdown. The magnitude of these effects is assumed to be proportional to a distance equal to the projected area of the corresponding portion of the fuselage on the x-y plane divided by the fuselage radius at the strake region plus the strake width if it is present. The increase or decrease in  $\alpha_{BD}$  is then taken to be the  $\Delta\alpha$  by which a vortex burst point will move over that distance.

The sectional data used in the calculation are again generated with the revised Eppler's code and are shown in Figure 32. Longitudinal characteristics of the basic configuration are shown in Figure 33. The prediction is seen to agree well with the data. Again, including the nonlinear section data improves significantly the agreement of the lift curve. Sideslip derivatives for both  $C_{n\beta}$  and  $C_{l\beta}$  are also well predicted (Fig. 34). Note that the nonlinearity of  $C_{n\beta}$  with  $\alpha$  is mainly predicted by the following mechanisms. A positive sideslip will produce a negative side force as usual. However, the freestream (i.e.  $V_\infty \sin\alpha$ ) results in a negative sideslip to the vertical tail producing a positive side force. The wing downwash, viewed as a positive sideslip to the vertical tail, will produce a negative side force. In earlier versions of the VORSTAB, the wing downwash effect was not included so that  $C_{n\beta}$  would be decreased rather quickly as  $\alpha$  is increased. With both  $V_\infty \sin\alpha$  and wing downwash included,  $C_{n\beta}$  will decrease more gradually. As  $\alpha$  is further increased, the wing vortex will burst and the boundary layer will separate to decrease the wing downwash at the vertical tail. At the same time, the local dynamic pressure

would be lower. All of these effects are to reduce the negative side force at the vertical tail. In the present code, an assumption is made to remove the wing downwash effect on the vertical tail as soon as  $\alpha_{BD}$  is reached. This assumption appears to work well for the basic F-5 configuration. At  $\alpha \geq 30$  degrees, the forebody vortices will have a dominating effect by producing forces on the forebody and interference on the vertical tail and are not modeled in the code.

For the F-5 configuration with a swept wing ( $\Lambda = 51$  degrees), both vortex lift and viscous separation are important. The wing has a snag which is known to generate a vortex at high  $\alpha$  that produces downwash on the outboard wing section and divides the wing vortex system into two. Each system is assumed to generate augmented vortex lift on the inboard or the outboard section of the wing, as the case may be. As shown in Figure 35, the longitudinal characteristics are well predicted. The total augmented vortex lift is only about 6 percent of the total lift at  $\alpha = 30$  degrees. Sideslip derivatives are presented in Figure 36. As shown, calculations with or without viscous effect are seen to give similar results which agree reasonably well with the data. Note that the effect of vortex breakdown is quite important for this configuration and was included in both sets of calculations.

For the configuration with a delta wing, the wing sweep ( $\Lambda = 59$  degrees) is expected to produce a vortex-dominated flow field. Therefore, the viscous effects were neglected in the calculation. As shown in Figure 37,  $C_L$ ,  $C_D$  and  $C_m$  are underestimated

at  $\alpha > 20$  degrees (Fig. 37), mainly because  $\alpha_{BD}$  is underpredicted. For the sideslip derivatives (Fig. 38), since  $C_{n\beta}$  is well calculated, the discrepancy of  $C_{l\beta}$  must be caused by early unloading at the wing tip. It is known that tip loading of a delta wing may be reduced by either vortex inboard migration or viscous separation because of high loading, or both.

(f) An X-29A Forward Swept Wing Configuration

The geometry of the model is presented in Figure 39. The model wing is made of a flat plate with a leading-edge radius equal to 1.3% of the root chord. The control surfaces include the canard, wing trailing-edge flaperons, and the fuselage-mounted straked flaps. The flaperons and strake flaps were deflected to their full-down positions (17.5 degrees and 30 degrees, respectively). The calculations are based on the inviscid flow with and without vortex breakdown. The deflection angle of the flaperons in the streamwise direction was calculated to be 13.6 degrees. It is seen from Figure 40 that both  $C_L$  and  $C_D$  are underpredicted perhaps because the geometric representation in the calculation is not accurate. All necessary geometric quantities for input were measured from Figure 39.

In the VORSTAB code, the vortex bursting is implemented to progress from the wing tip toward the apex. In the swept-forward wing situation, the leading-edge vortex separation starts at the wing tip; and its bursting may start at the wing root and move toward the tip, which is opposite to the progression direction assumed in the program. In Figure 41, the  $C_{l\beta}$  prediction without vortex breakdown appears better than the one with vortex breakdown.



(g) An F-106B Configuration

As shown in Figure 42, the basic F-106B configuration has a highly swept wing which is dominated by vortex flow at high angles of attack. Therefore, inviscid flow is assumed in the calculation. Figure 43 shows good agreement with data for the longitudinal characteristics.  $C_D$  is underpredicted at high  $\alpha$  perhaps because the thrust component of lift acting on the conical camber is overpredicted by the code. In the lateral-directional calculation (Fig. 44), predicted  $C_{n_\beta}$  and  $C_{l_\beta}$  match well with experimental data up to  $\alpha = 30$  degrees. However,  $C_{y_\beta}$  is not as well predicted, probably due to the wing and fuselage interference. Figures 45 and 46 show the lateral-directional derivatives due to rolling and yawing. The experimental data measured in forced-oscillation tests and taken from Reference 32 to compare with the predicted  $C_{y_p}$ ,  $C_{n_p}$ , and  $C_{l_p}$  are  $(C_{y_p} + C_{y_\beta} \sin\alpha)$ ,  $(C_{n_p} + C_{n_\beta} \sin\alpha)$ , and  $(C_{l_p} + C_{l_\beta} \sin\alpha)$ . The test results taken from the same reference to compare with  $C_{y_r}$ ,  $C_{n_r}$ , and  $C_{l_r}$  are  $(C_{y_r} - C_{y_\beta} \cos\alpha)$ ,  $(C_{n_r} - C_{n_\beta} \cos\alpha)$ , and  $(C_{l_r} - C_{l_\beta} \cos\alpha)$ , respectively. This code is not designed for unsteady calculation. Therefore, discrepancy at high angles of attack is expected. In forced-oscillation tests, damping derivatives tend to be higher because of aerodynamic lag effect (e.g. viscous and vortex lag). Figure 47 shows the aileron control power at an aileron deflection of 7 degrees. The rolling moment is mainly contributed by the antisymmetric wing lift due to aileron deflection and is correctly computed. The yawing moment is not as well predicted at low angles of attack. Figure 48 shows the

rudder control power at a rudder deflection of 25 degrees. In this case, the yawing moment is more accurately calculated than the rolling moment.

#### 4. CONCLUSIONS

The VORSTAB code has been shown to be capable of accounting for, but not limited to, vortex breakdown effect, viscous effect, vortex lift, and suction force, etc. The viscous separation effect was included through the use of nonlinear section data. The nonlinear section data were calculated with a revised Eppler's code for thin airfoils based on a modified free wake theory for post-stall characteristics. Calculated results for complete airplane configurations showed the longitudinal aerodynamics and the lateral-directional derivatives predicted by the VORSTAB code gave reasonable results compared with wind-tunnel test data up to an angle of attack at which wake interference and forebody vortex effect were not significant. Such an angle of attack was found to be configuration dependent and might be different for longitudinal and lateral-directional aerodynamics. Good results could be expected for those configurations dominated either by vortex flow or viscous separation. Overall, predicted results for longitudinal characteristics agreed better with wind-tunnel data than with lateral-directional results. One possible reason for the disagreement is wake interference between lifting surfaces. Also the forebody vortex might transgress the flowfield of the vertical

tail leading to an inaccurate prediction of lateral-directional derivatives at high angles of attack. In addition, asymmetrical forebody vortices in a sideslip would produce significant effect on directional derivatives and were not accounted for in the present code.

Based on the experience gained in this investigation, a successful modeling for the VORSTAB code would require

- (1) good judgment as to whether a configuration was vortex-flow dominated or might require nonlinear section data;
- (2) a good estimate of where the augmented vortex lift might occur and the amount of favorable or adverse pressure gradient to cause the change in vortex-breakdown angles of attack; and
- (3) an accurate geometric representation of a configuration, including camber shapes, airfoil geometry, leading-edge sweep, etc.

Typically, forebody and strake vortices were favorable to vortex stability of the wing. But the strake vortex would burst earlier due to the presence of wing adverse pressure gradient.

To improve the code, the interference of forebody and strake vortices on the vertical tail must be determined. This would require the calculation of the locations of these vortices. In addition, the effect of wing wake and vortex-burst flow field on the empennage would be an important factor in predicting static lateral-directional characteristics. For dynamic lateral-directional characteristics at high angles of attack, an appropriate unsteady aerodynamic theory would be needed.

## REFERENCES

1. Magnus, A. E.; and Epton, M. E.: PAN AIR--A Computer Program for Predicting Subsonic or Supersonic Linear Potential Flows about Arbitrary Configurations Using a Higher Order Panel Method; Volume 1: Theory Document (Version 1.0). NASA CR-3251, April 1980.
2. Carmichael, R. L.; and Erickson, L. L.: PAN AIR--A Higher Order Panel Method for Predicting Subsonic or Supersonic Linear Potential Flows about Arbitrary Configurations. AIAA Paper 81-1255, June 1981.
3. Johnson, F. T.; Tinoco, E. N.; Lu, P.; and Upton, M. A.: Three-Dimensional Flow over Wings with Leading-Edge Vortex Separation. AIAA Journal, Vol. 18, April 1980, pp. 367-380.
4. Maskew, B.: Prediction of Subsonic Aerodynamic Characteristics: A Case for Low-Order Panel Methods. Journal of Aircraft, Vol. 19, Feb. 1982, pp. 157-163.
5. Maskew, B.; and Rao, B. M.: Calculation of Vortex Flows on Complex Configurations. ICAS-82-6.2.3, 1982.
6. Dusto, A. R., et al.: A Method for Predicting the Stability Characteristics of Control Configured Vehicles. AFFDL-TR-74-91, Nov. 1974.
7. De Hart, J. H.; Gilchrist, I. J.; and Jenkins, J. E.: Development of a Stability and Control Data Prediction Capability Using an Advanced Aerodynamic Paneling Program. Presented at National Aerospace and Electronics Conference, Dayton, Ohio, May 20, 1987.

8. Lan, C. E.: VORSTAB--A Computer Program for Calculating Lateral-Directional Stability Derivatives with Vortex Flow Effect. NASA CR-172501, January 1985.
9. Lan, C. E.: Theoretical Prediction of Wing Rocking. AGARD CP-386, 1985.
10. Lan, C. E.: A Quasi-Vortex-Lattice Method in Thin Wing Theory. Journal of Aircraft, Vol. 11, Sept. 1974, pp. 518-527.
11. Lan, C. E.; and Chang, J. F.: Calculation of Vortex Lift Effect for Cambered Wings by the Suction Analogy, NASA CR-3449, July 1981.
12. Wards, G. N.: Linearized Theory of Steady High-Speed Flow. Cambridge University Press, 1955.
13. Lan, C. E.: Calculation of Lateral-Directional Stability Derivatives for Wing-Body Combinations with and without Jet-Interaction Effects. NASA CR-145251, August 1977.
14. Finck, R. D., et al.: USAF Stability and Control Datcom. U.S. Air Force Flight Dynamics Laboratory, Wright-Patterson Air Force Base, Ohio, Contracts AF33 (616)-6460 and F33615-76-C-3061, McDonald Douglas Corp., October 1960. (Revised Apr. 1978).
15. Polhamus, E. C.: A Concept of the Vortex Lift of Sharp-Edge Delta Wings Based on a Leading-Edge-Suction Analogy. NASA TN D-3767, Dec. 1966.
16. Lamar, J. E.: Recent Studies of Subsonic Vortex Lift Including Parameters Affecting Stable Leading-Edge Vortex Flow. Journal of Aircraft, Vol. 14, Dec. 1977, pp. 1205-1211.

17. Kulfan, R. M.: Wing Airfoil Shape Effects on the Development of Leading-Edge Vortices. AIAA Paper 79-1675, 1979.
18. Kulfan, R. M.: Wing Geometry Effects on Leading-Edge Vortices. AIAA Paper 79-1872, 1979.
19. Lan, C. E.; and Su, I: Effect of a Round Airfoil Nose on Leading-Edge Suction. Journal of Aircraft, Vol. 24, July 1987, pp. 472-474.
20. Robinson, A.; and Laurmann, J. A.: Wing Theory. Cambridge University Press, 1956.
21. Wentz, W. H., Jr.: Wind Tunnel Investigations of Vortex Breakdown on Slender Sharp-Edged Wings. Also NASA CR-98737, 1968.
22. Lan, C. E.; and Hsu, C. H.: Effects of Vortex Breakdown on Longitudinal and Lateral-Directional Aerodynamics of Slender Wings by the Suction Analogy. AIAA Paper 82-1385, 1982.
23. Earnshaw, P. B.: Measurement of the Effects of Thickness on Vortex Breakdown Position on a Series of Sharp-Edged Delta Wings. British ARC C.P. No. 1018, 1968.
24. Almosnino, P.; and Rom, J.: Calculation of Symmetric Vortex Separation Affecting Subsonic Bodies at High Incidence. AIAA Journal, Vol. 21, March 1983, pp. 398-406.
25. Lan, C. E.: Extensions of the Concept of Suction Analogy to Prediction of Vortex Lift Effect. NASA CP-2416, Vortex Flow Aerodynamics, Vol. I, 1986, pp. 65-84.

26. Nguyen, L. T.; Yip, L.; and Chambers, J. R.: Self-Induced Wing Rock of Slender Delta Wings. AIAA Paper 81-1883, Aug. 1981.
27. Harvey, J. K.: Some Measurements on a Yawed Slender Delta Wing with Leading-Edge Separation. British ARC R&M No. 3160, Oct. 1958.
28. Blascovich, J. D.: A Comparison of Separated Flow Airfoil Analysis Methods. Journal of Aircraft, Vol. 22, March 1985, pp. 208-215.
29. Rumsey, C. L.: Evaluation of a Stalled Airfoil Analysis Program. Journal of Aircraft, Vol. 22, February 1985, pp. 156-157.
30. Stivers, L. S., Jr.: Effects of Subsonic Mach Numbers on the Forces and Pressure Distributions on Four NACA 64A-Series Airfoil Sections at Angles of Attack. NACA TN-3162, 1954.
31. Wick, B. H.: Study of the Subsonic Forces and Moments on an Inclined Plate of Infinite Span. NACA TN-3221, 1954.
32. Eppler, R.; and Somers, D. M.: A Computer Program for the Design and Analysis of Low-Speed Airfoils. NASA TM-80210, 1980.
33. Lan, C. E.; and Lee, I. G.: Investigation of Empennage Buffetting. NASA CR-179426, January 1987.
34. Lutze, F. H.: Curved Flow Wind Tunnel Test of F-18 Aircraft. VPI-Aero-108, April 1980.
35. Lamar, J. E.; and Frink, N. T.: Experimental and Analytical Study of the Longitudinal Aerodynamic Characteristics of Analytically and Empirically Designed Strake-Wing Configurations at Subcritical Speeds. NASA TP-1803, June 1981.

36. Chambers, J. R.; and Anglin, E. L.: Analysis of Lateral-Directional Stability Characteristics of a Twin-Jet Fighter Airplane at High Angles of Attack. NASA TN D-5361, August 1969.
37. Nguyen, L. T.; Whipple, R. D.; and Brandon, J. M.: Recent Experiments of Unsteady Aerodynamic Effects on Aircraft Flight Dynamics at High Angles of Attack. AGARD CP-386, 1985.
38. Nguyen, L. T.; Ogburn, M. E.; Gilbert, W. P.; Kibler, K. S.; Brown, P. W.; and Deal, P. L.: Simulator Study of Stall/Post-Stall Characteristics of a Fighter Airplane with Relaxed Longitudinal Static Stability. NASA TP-1538, December 1979.
39. Grafton, S. B.: Low-Speed Wind-Tunnel Study of the High Angle-of-Attack Stability and Control Characteristics of a Cranked-Arrow-Wing Fighter Configuration. NASA TM-85776, May 1984.
40. Grafton, S. B.; Chambers, J. R.; and Coe, P. L., Jr.: Wind-Tunnel Free-Flight Investigation of a Model of a Spin-Resistant Fighter Configuration. NASA TN D-7716, 1974.
41. Murri, D. G.; Nguyen, L. T.; and Grafton, S. B.: Wind-Tunnel Free-Flight Investigation of a Model of a Forward-Swept-Wing Fighter Configuration. NASA TP-2230, February 1984.
42. Yip, L. P.: Wind-Tunnel Free-Flight Investigation of a 0.15-Scale Model of the F-106B Airplane With Vortex Flaps. NASA TP-2700, 1987.



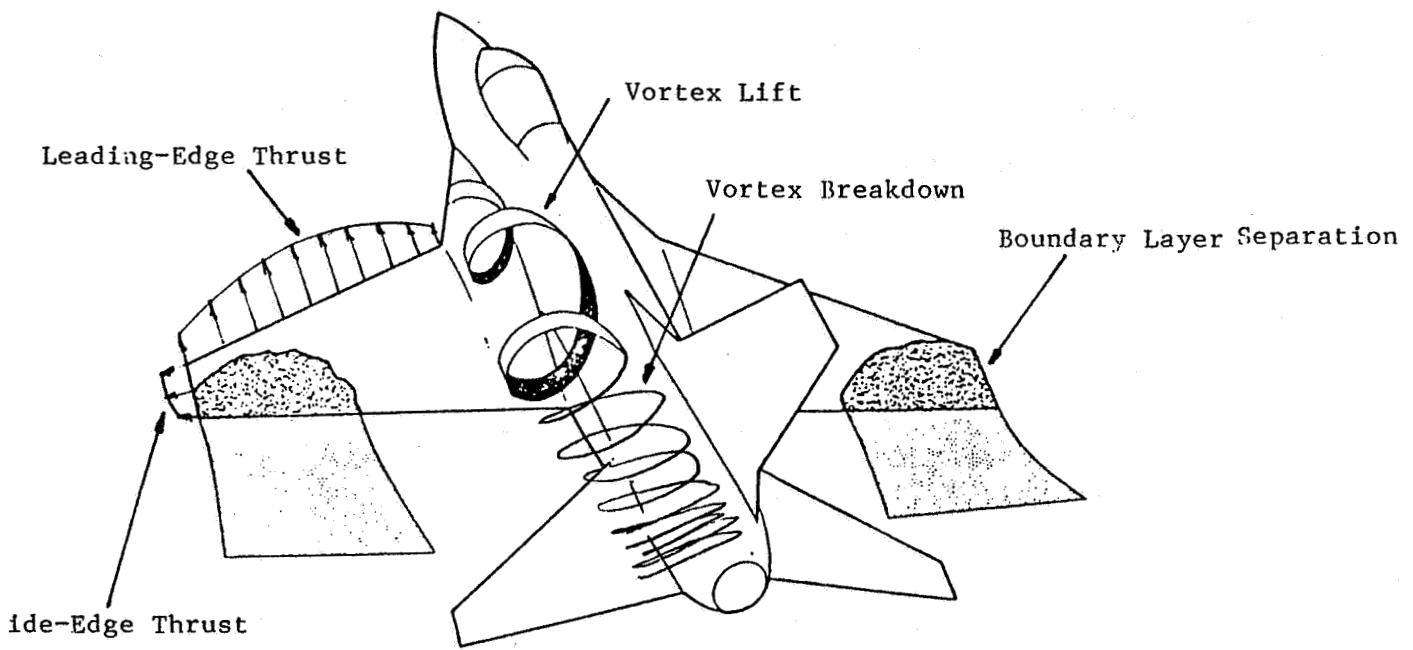


Figure 1. Illustration of Aerodynamic Characteristics at High Angles of Attack

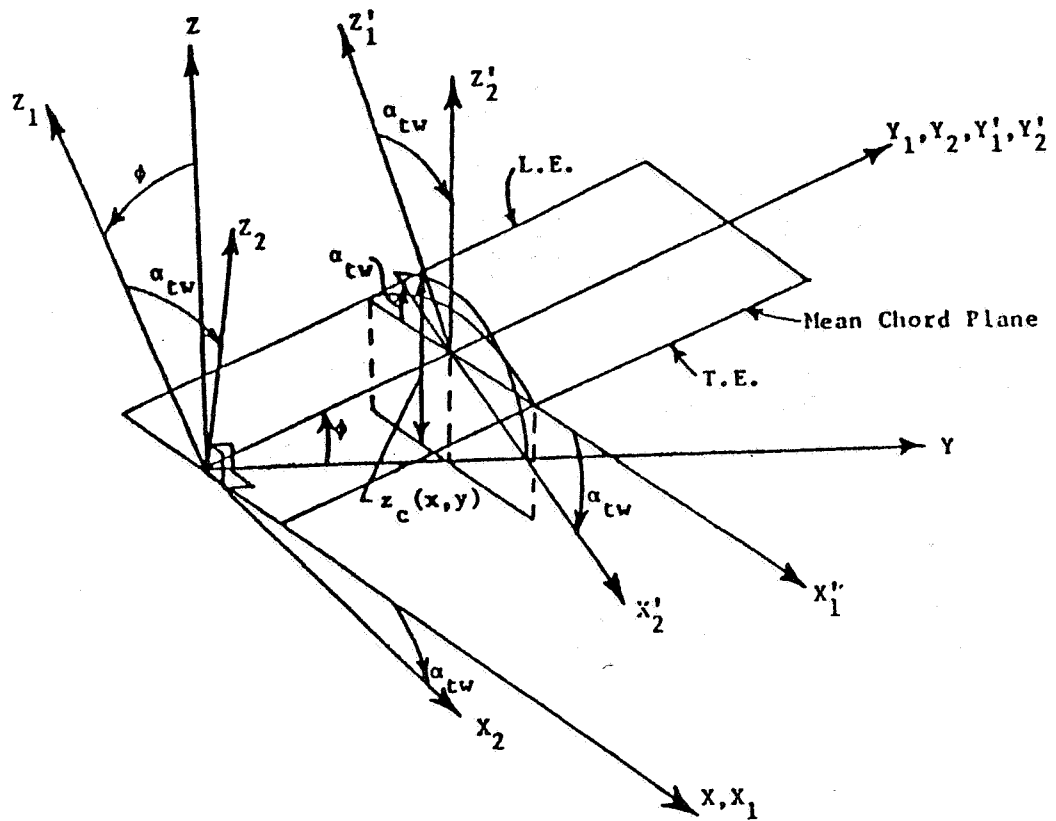


Figure 2. Definition of Variables Defining a Nonplanar Wing Surface (Ref. 11)

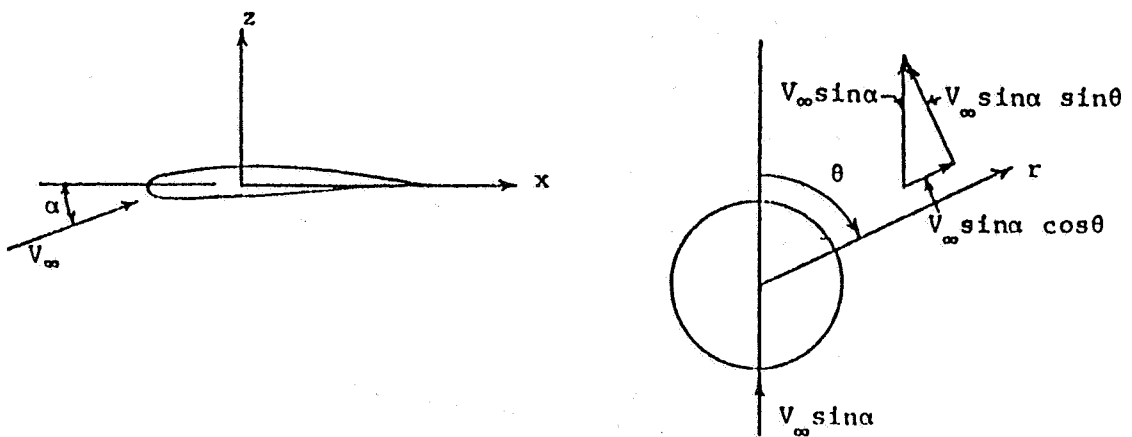


Figure 3. Fuselage Cylindrical Coordinates System

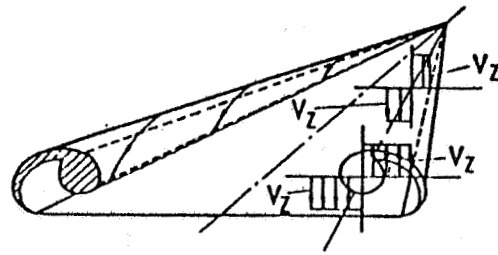


Figure 4. Illustration of Leading-Edge Vortex Separation (Ref. 11)

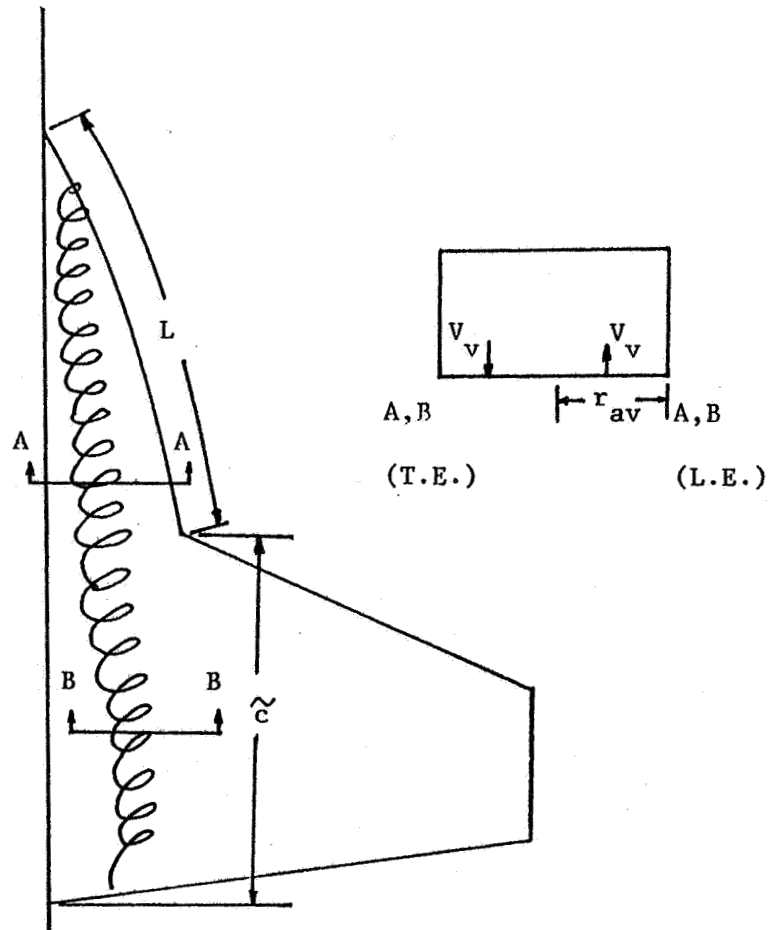


Figure 5. Geometry Illustrating Augmented Vortex Lift

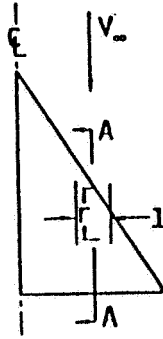


Figure 6. Wing Section for Defining Vortex Action Point (Ref. 11)

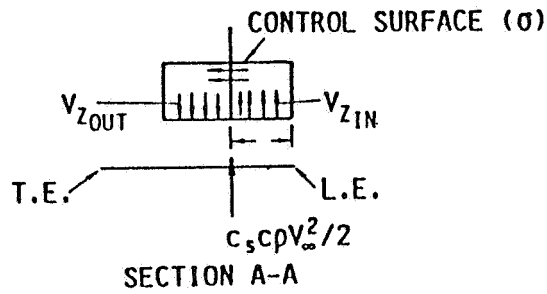


Figure 7. A Control Surface Taken in Cross-Flow Plan (Ref. 11)

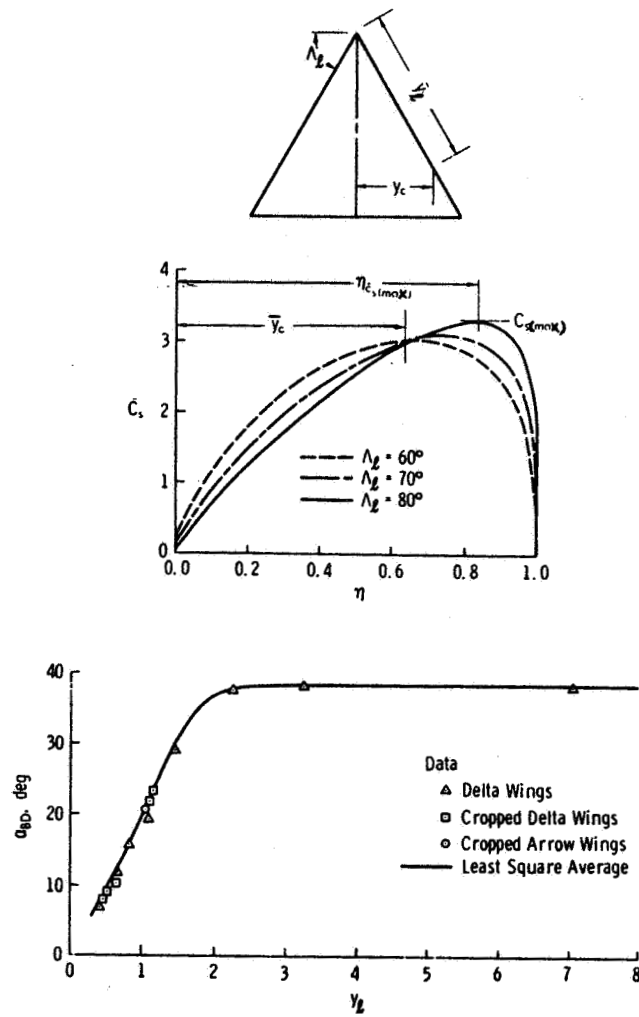


Figure 8a. Vortex Breakdown Angle for Different Planforms (Ref. 22)

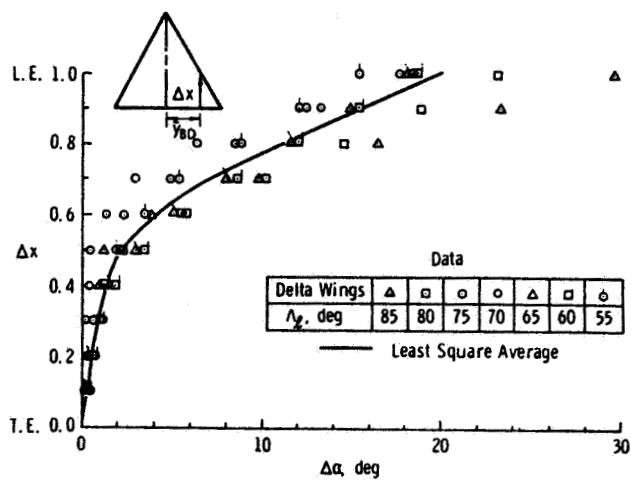


Figure 8b. Progression Rate of Vortex Breakdown Points for Different Planforms (Ref. 22)

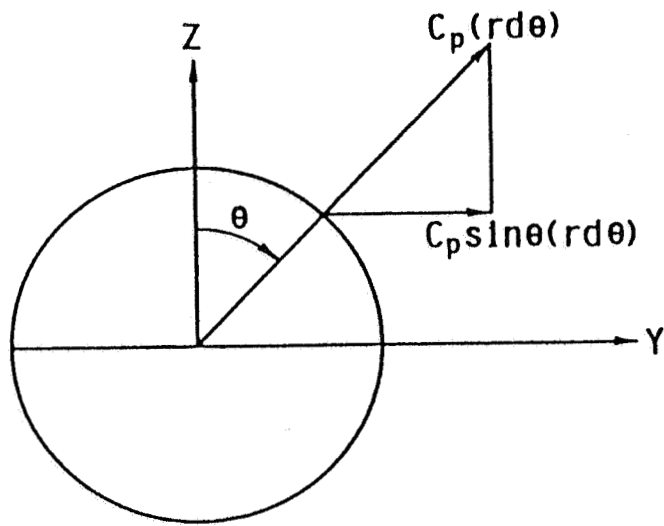


Figure 9. Calculation of Positive Side Force

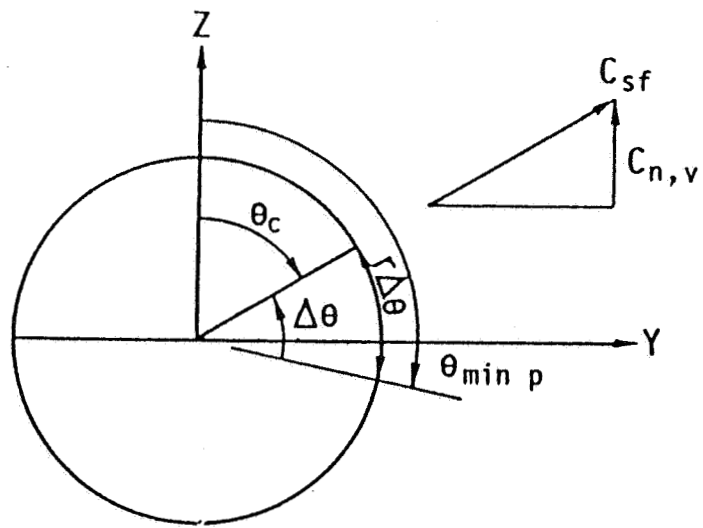


Figure 10. Vortex Action Point and Vortex Normal Force on a Body

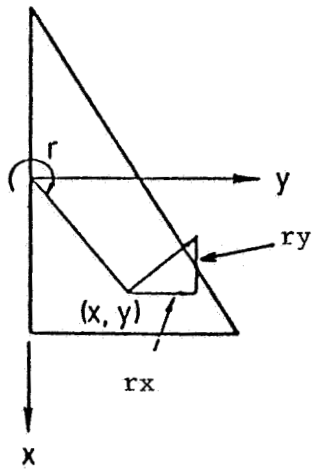


Figure 11. Variable Sideslip Effect Due to Yaw Rate

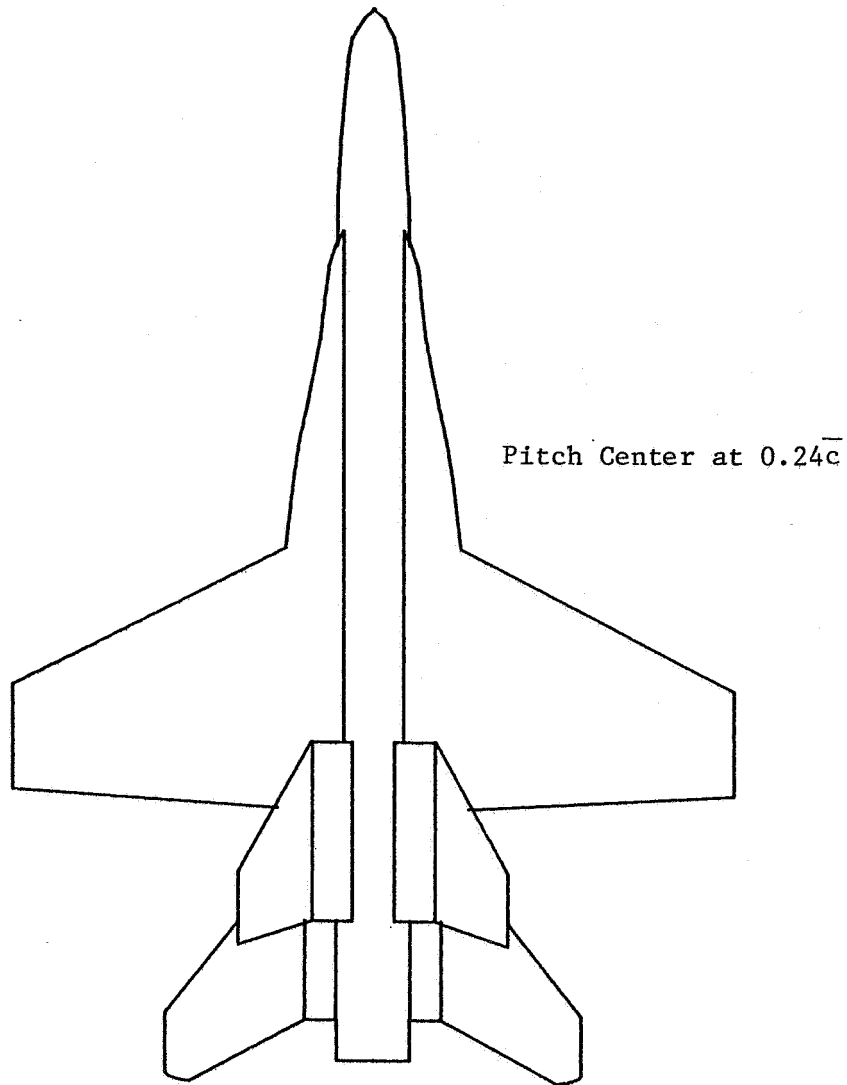


Figure 12. The Geometry of the F/A - 18 Configuration



--- Flat Plate (Ref. 31)  
— NACA 65A (X) 05.0 (Mod) at  $RN=0.6 \times 10^6$

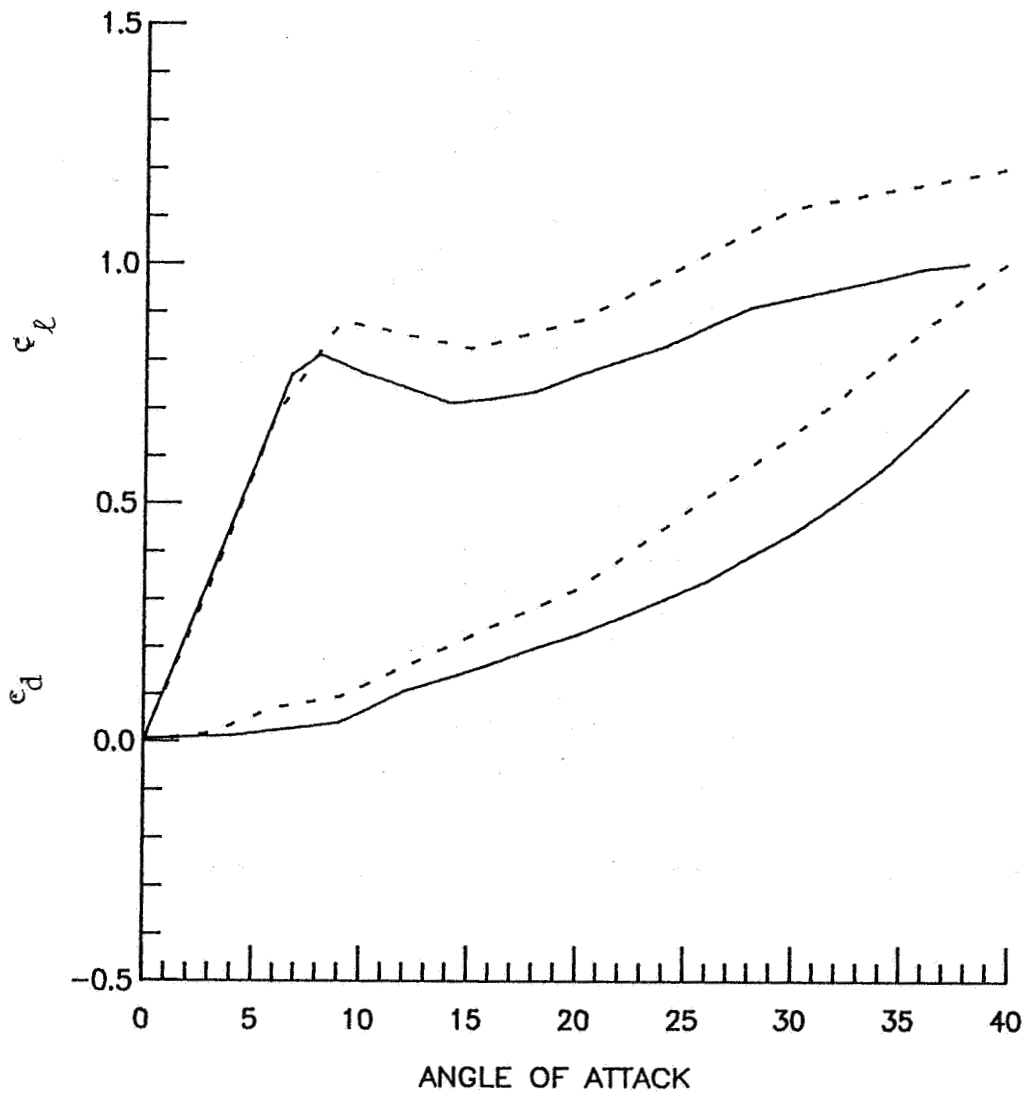
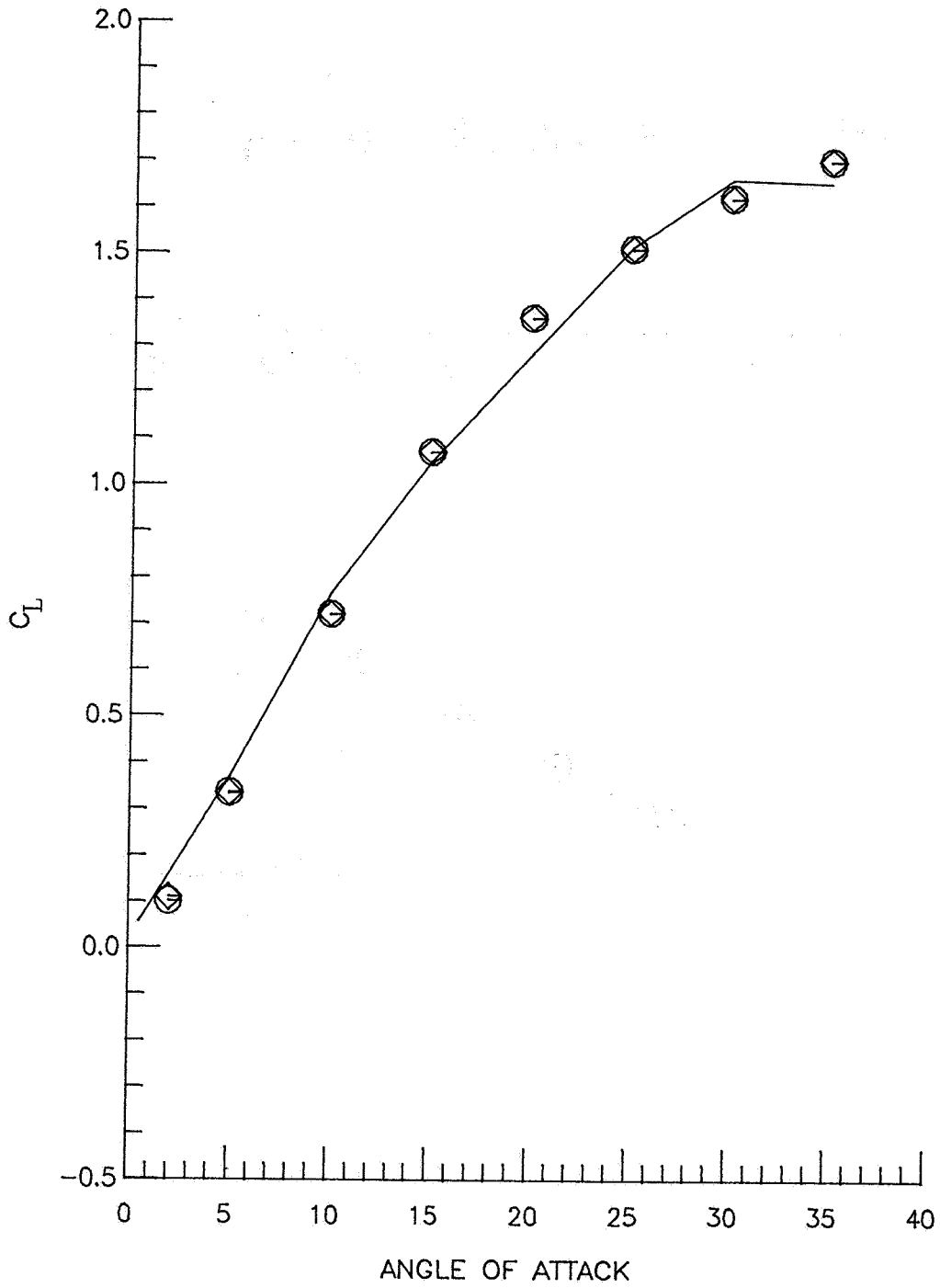


Figure 13. Wing Sectional Characteristics for the F/A - 18

⊙ — Experimental Data (Ref. 34)  
 ◇ — Navy Simulation Data  
 — VORSTAB Calculation



(a)  $C_L$  vs  $\alpha$

Figure 14. Longitudinal Characteristics of an F/A-18 Configuration Without Leading-Edge Flap Deflection

- ⊖ — Experimental Data (Ref. 34)
- ◇ — Navy Simulation Data
- — VORSTAB Calculation

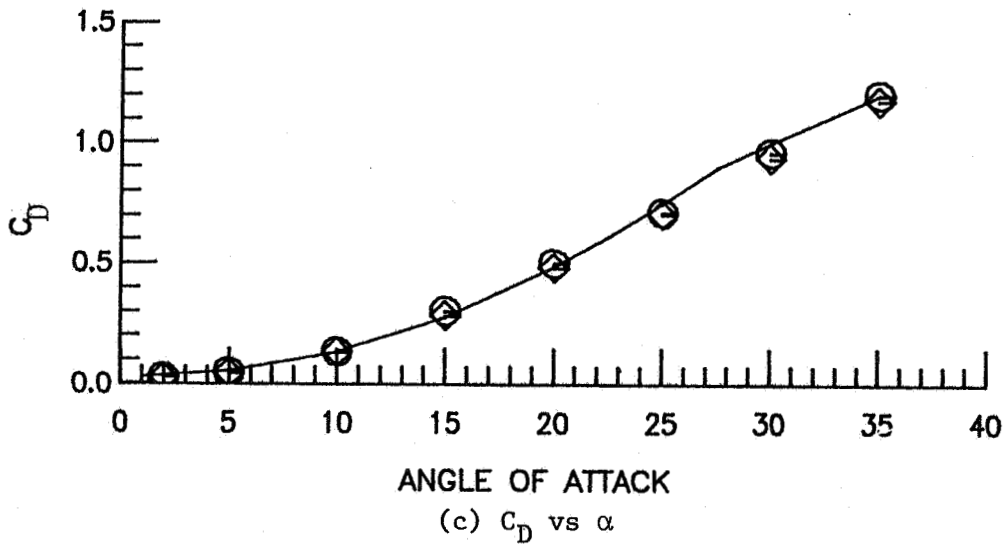
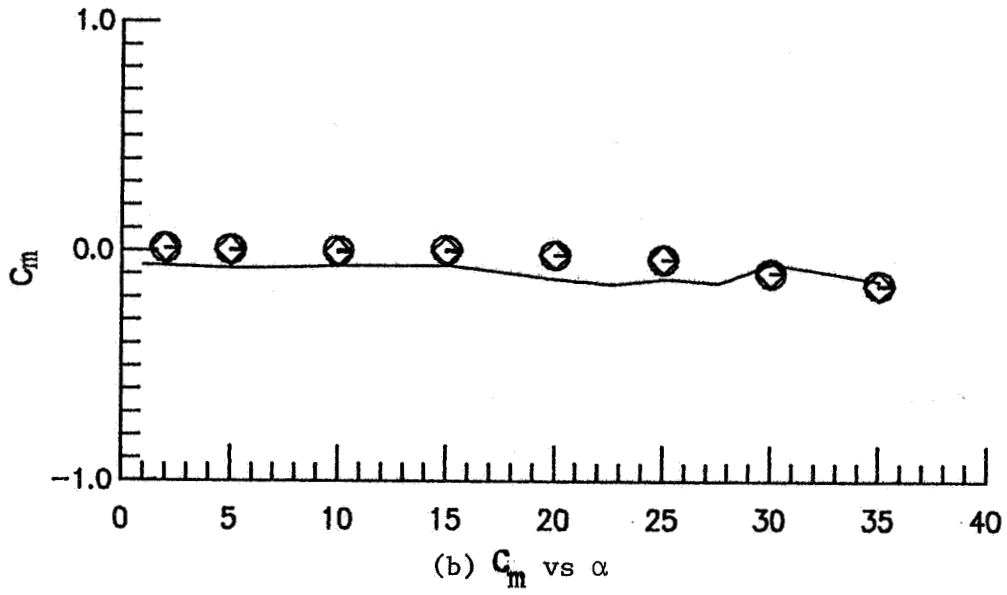


Figure 14. Continued

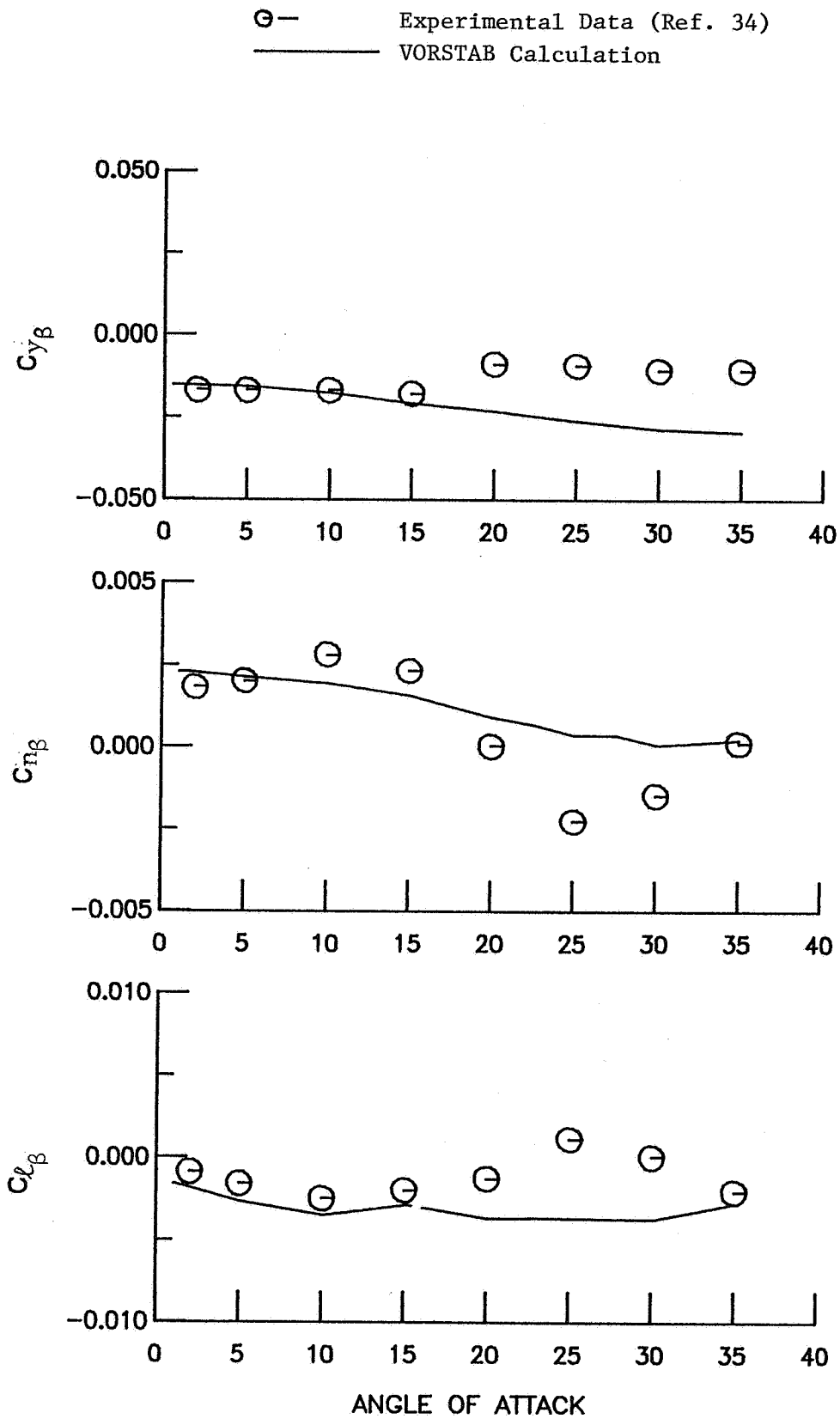


Figure 15. Lateral-Directional Derivatives Calculation of an F/A-18 Configuration Without Leading-Edge Flap Deflection

- - - Flat Plate (Ref. 31)  
 — NACA 65A (X) 05.0 (Mod) with leading-edge flap deflection assumed

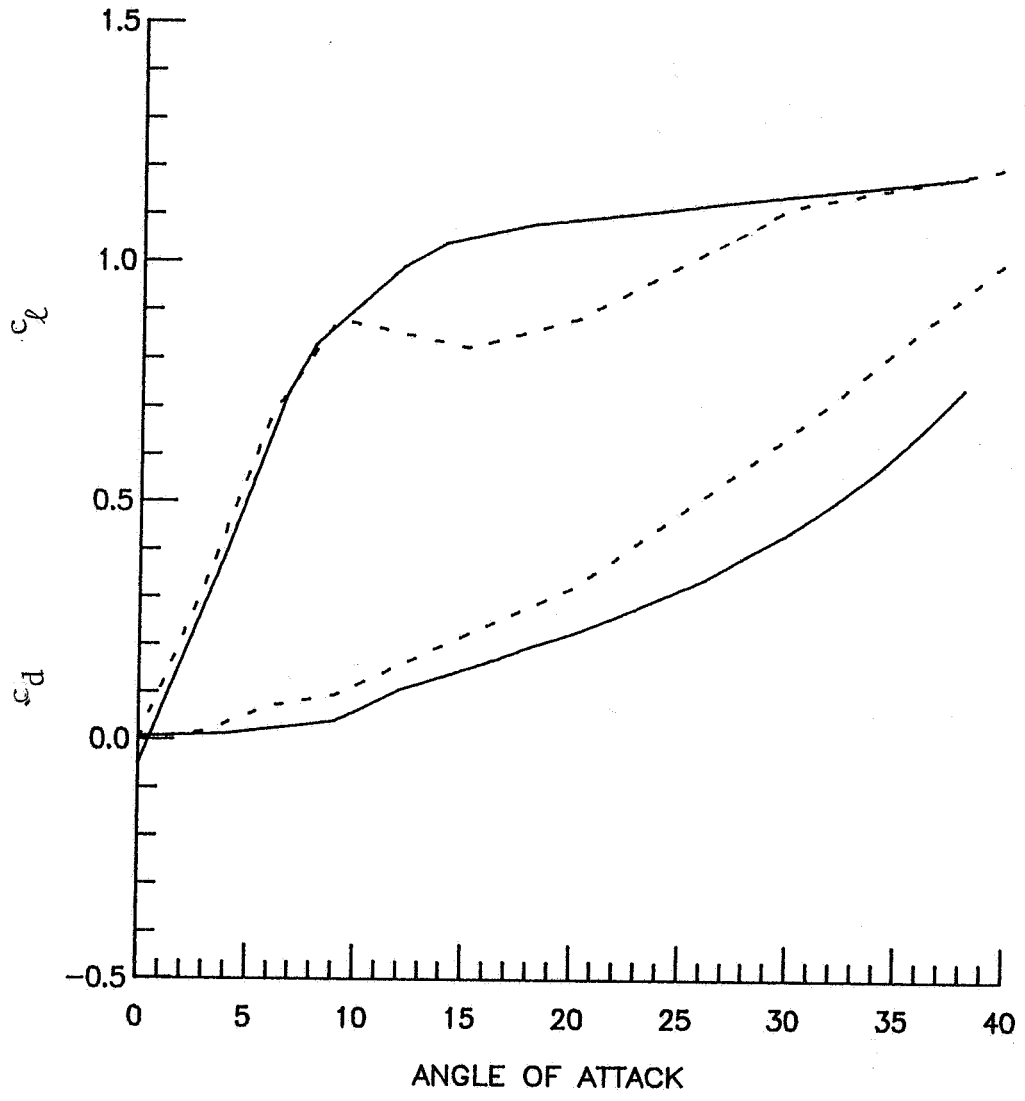


Figure 16. Nonlinear Sectional Data for an F/A-18 Configuration with Leading-Edge Flap Deflected at 25 Degrees

⊖ — Experimental Data (Ref. 34)  
— VORSTAB Calculation

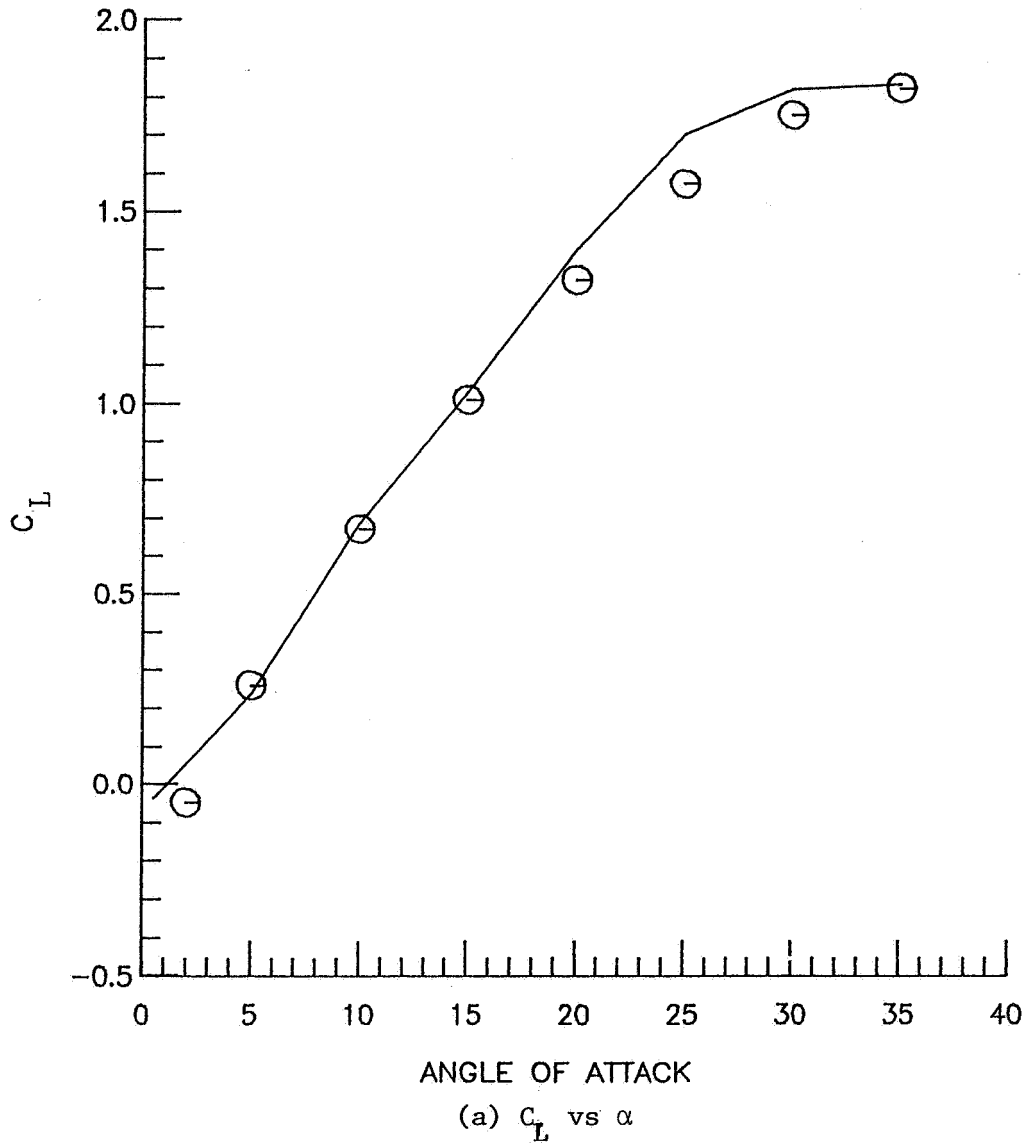
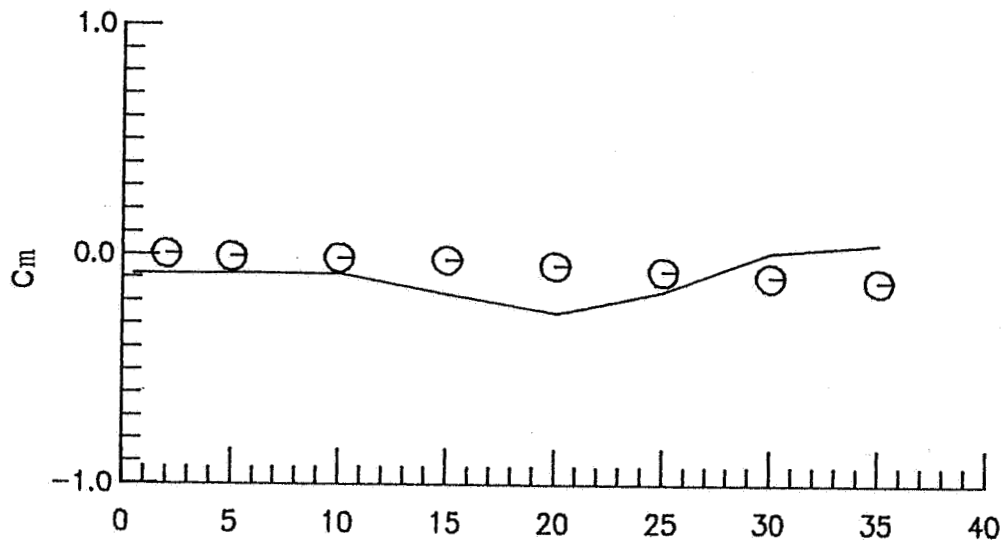
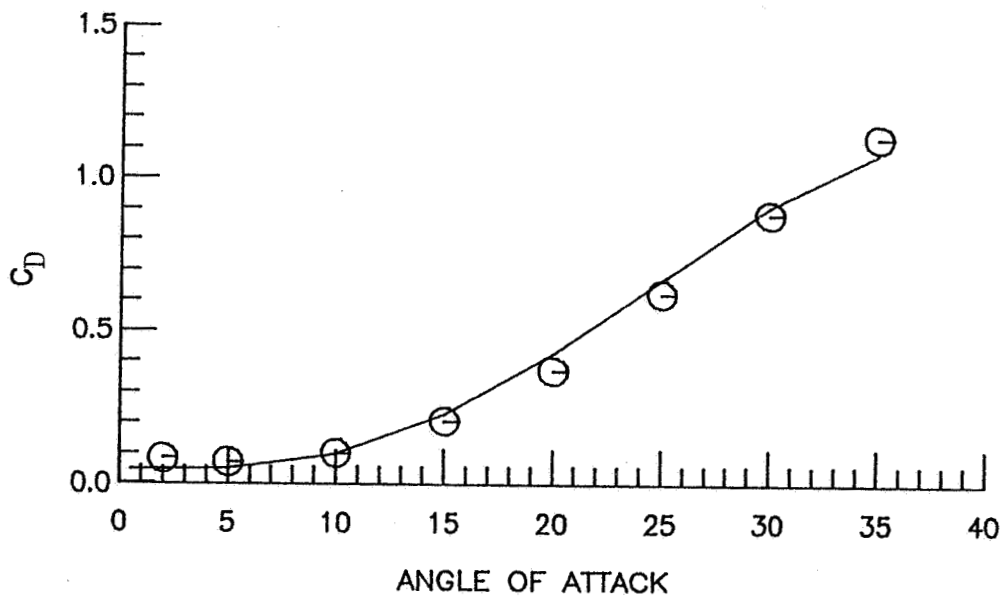


Figure 17. Longitudinal Characteristics of an F/A-18 Configuration with Leading-Edge Flap Deflected at 25 Degrees

⊖ — Experimental Data  
— VORSTAB Calculation



(b)  $C_m$  vs  $\alpha$



(c)  $C_D$  vs  $\alpha$

Figure 17. Continued

⊖ — Experimental Data (Ref. 34)  
 ——— VORSTAB Calculation

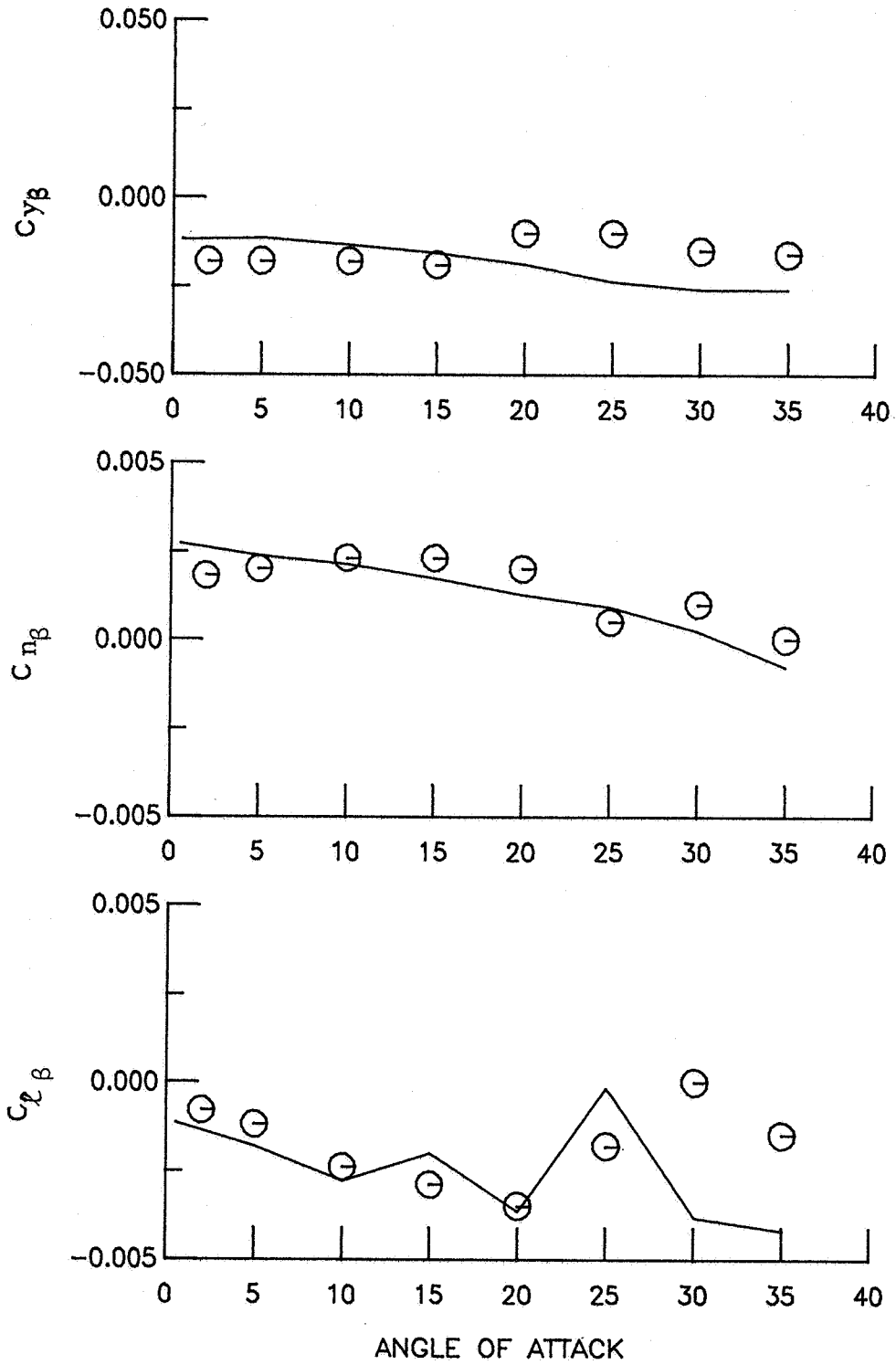
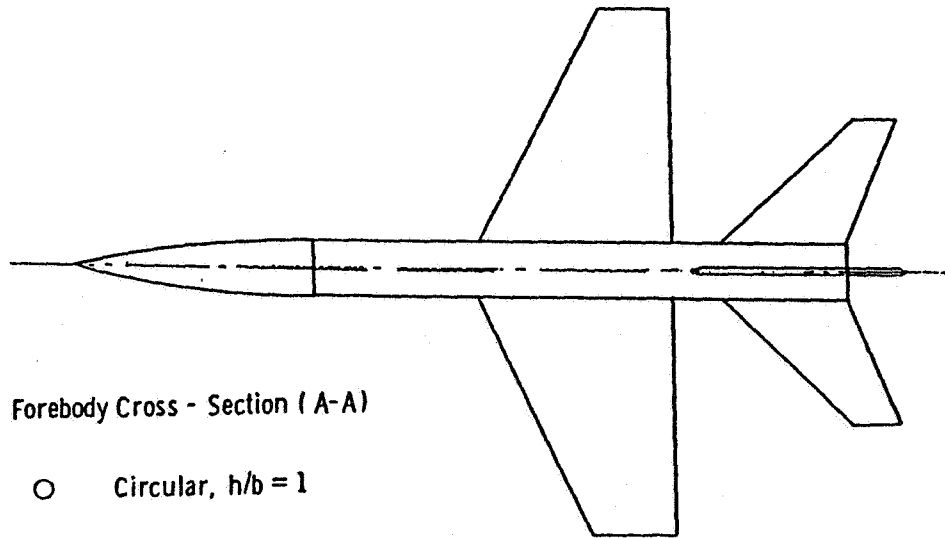


Figure 18. Lateral-Directional Derivatives for an F/A-18 Configuration with Leading-Edge Flap Deflected at 25 Degrees





Forebody Cross - Section ( A-A)

○ Circular,  $h/b = 1$

Pitch Center at 3.2 ft from the Nose

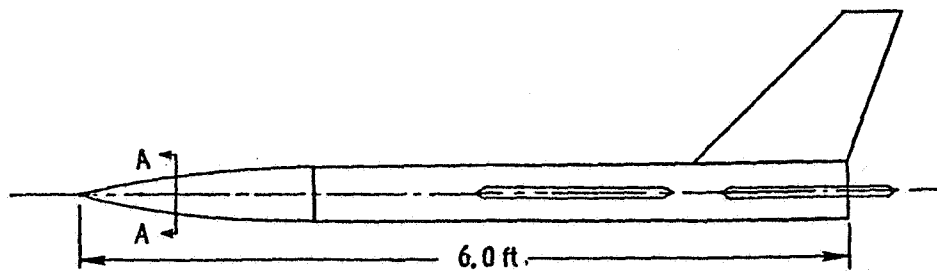


Figure 19. A Generic Fighter Model Tested in the 12-ft Tunnel at NASA Langley Research Center (Ref. 37)

— Flat Plate Sectional Data (Ref. 31)

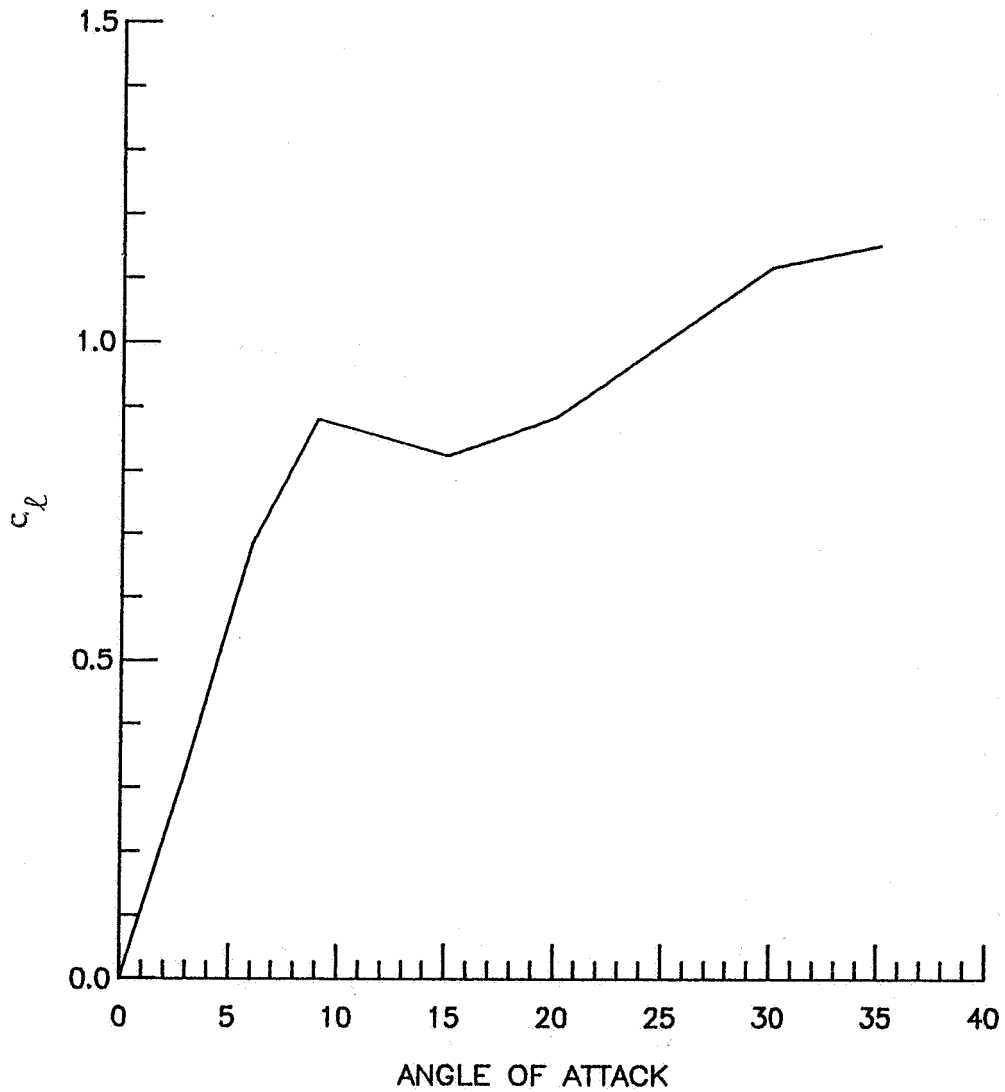
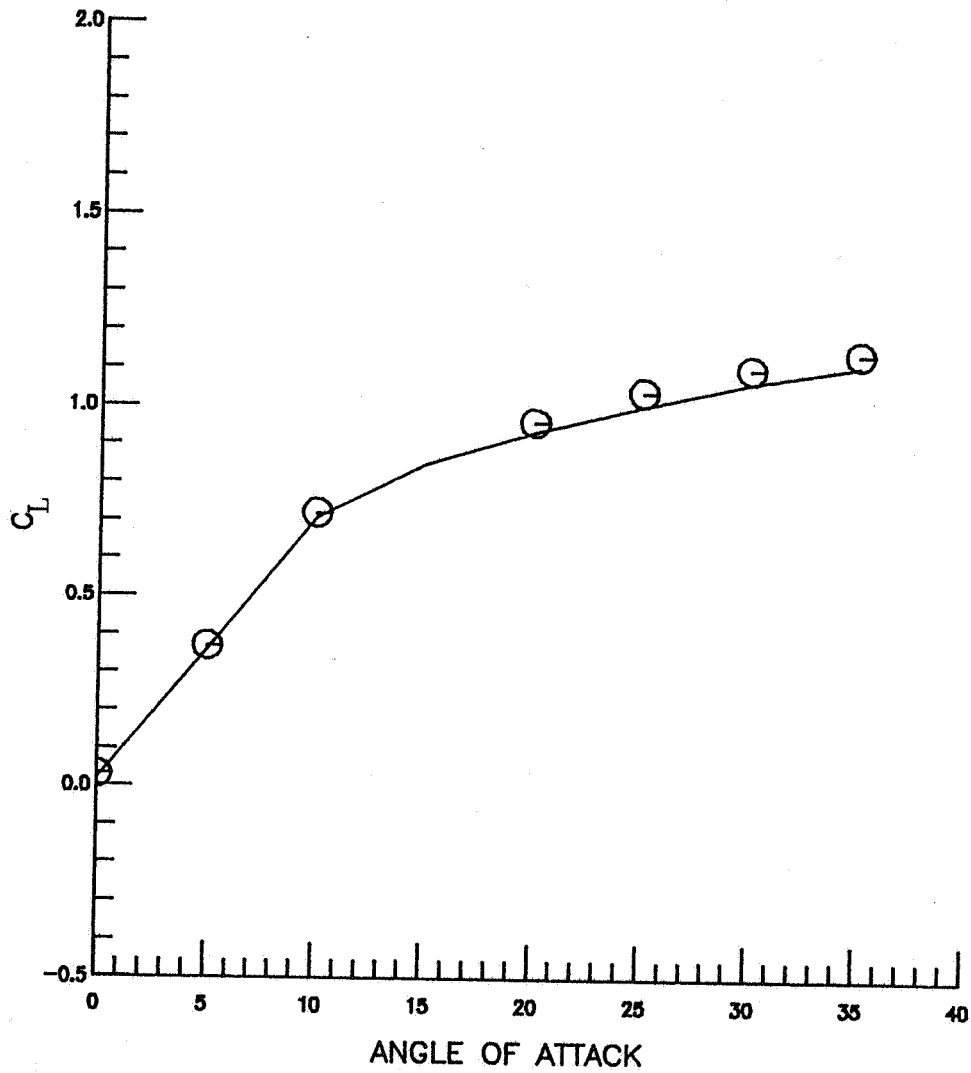


Figure 20. Sectional Lift Coefficients Used in the Generic Fighter Calculation

⊖ Experimental Data (Ref. 37)  
— VORSTAB Calculation



(a)  $C_L$  vs  $\alpha$

Figure 21. Longitudinal Aerodynamic Characteristics for a Generic Configuration

⊖ Experimental Data (Ref. 37)  
— VORSTAB Calculation

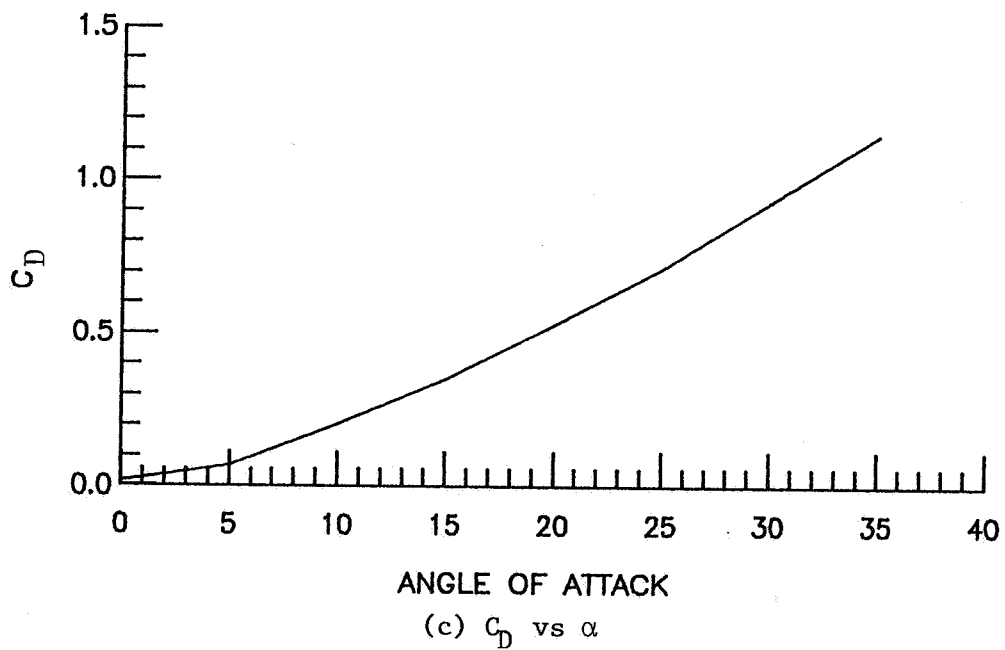
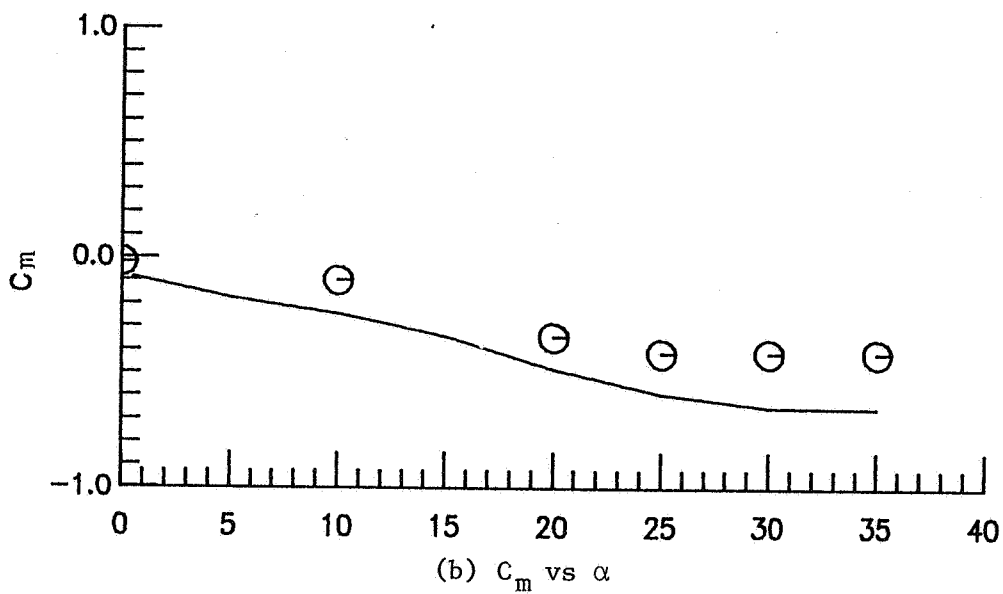


Figure 21. Continued

⊖— Experimental Data (Ref. 37)  
 ——— VORSTAB Calculation

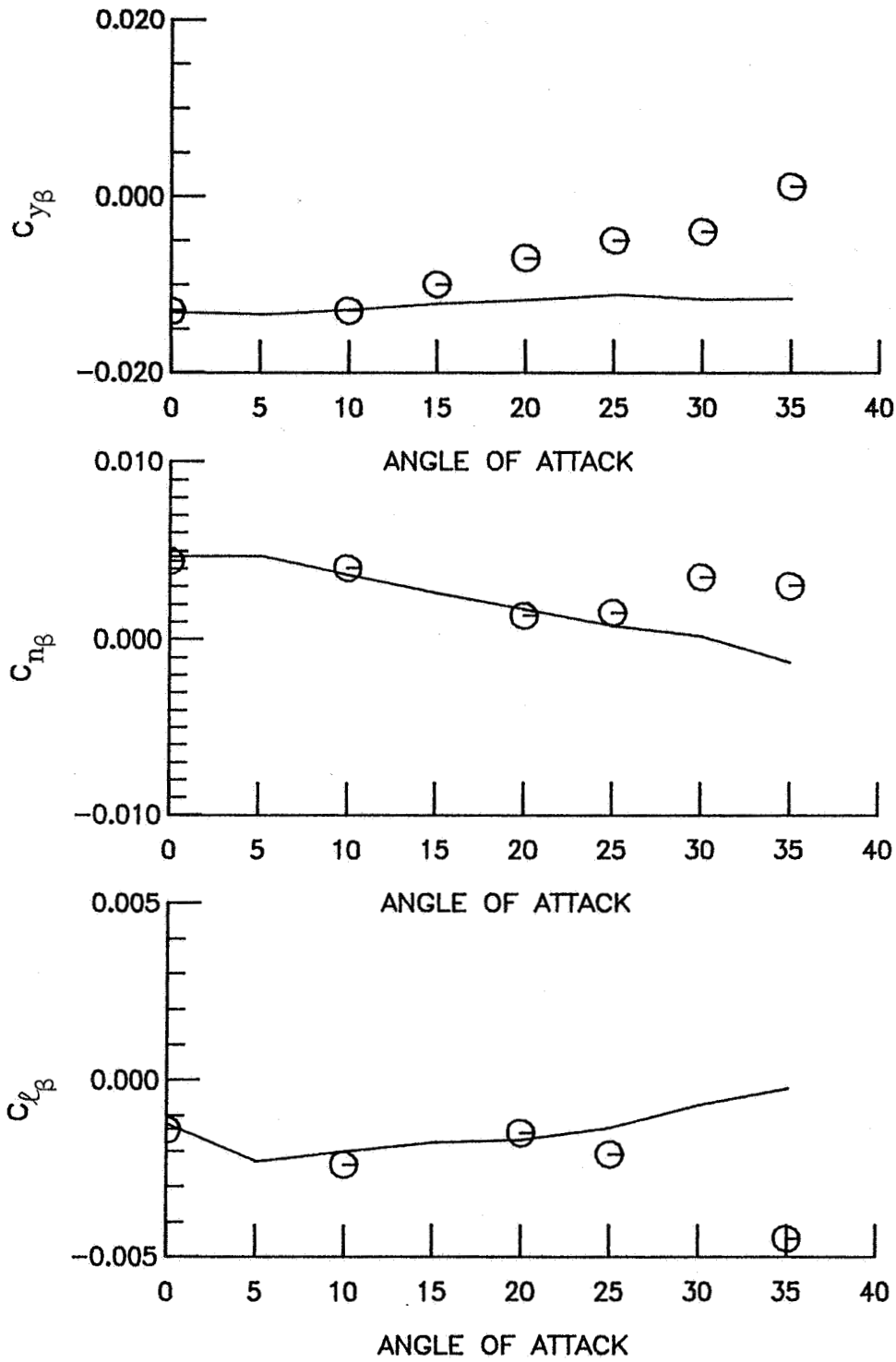
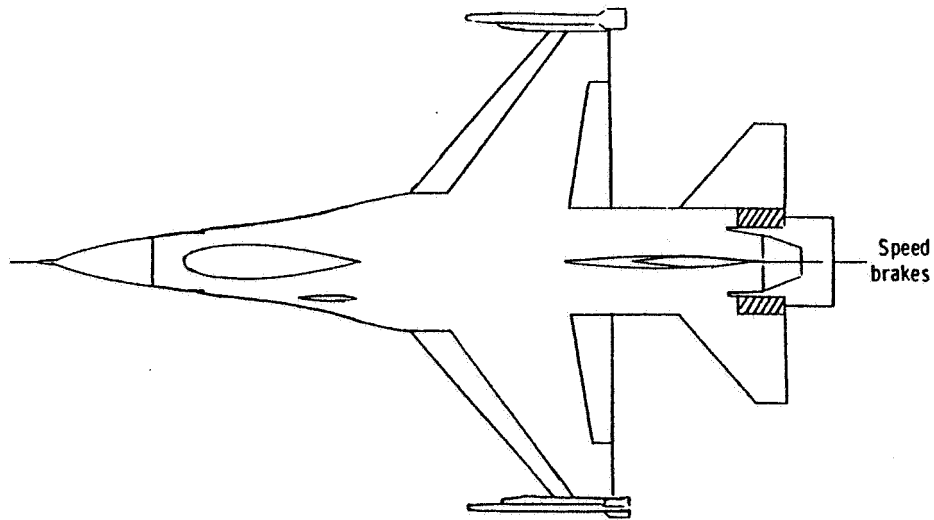
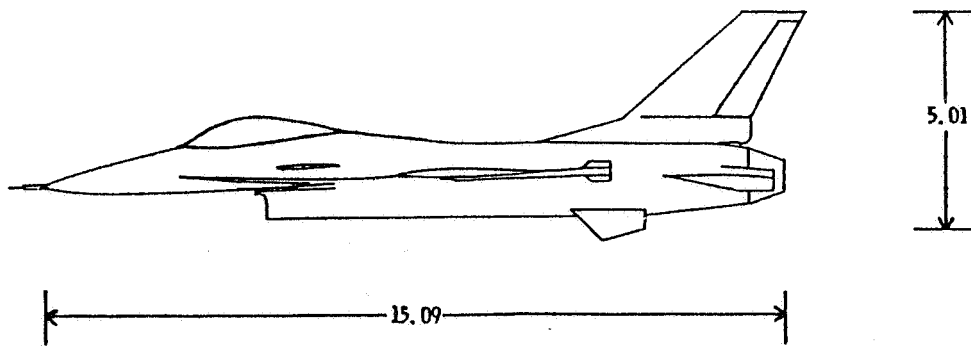
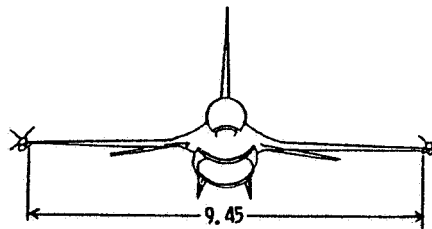


Figure 22. Lateral-Directional Derivatives Calculation of a Generic Fighter Based on the Body Axis at  $\beta = 4$  Degrees



Pitch Center at  $0.35\bar{c}$



Dimensions are given in meters.

Figure 23. Three-view Sketch of the F-16 Configuration (Ref. 38)

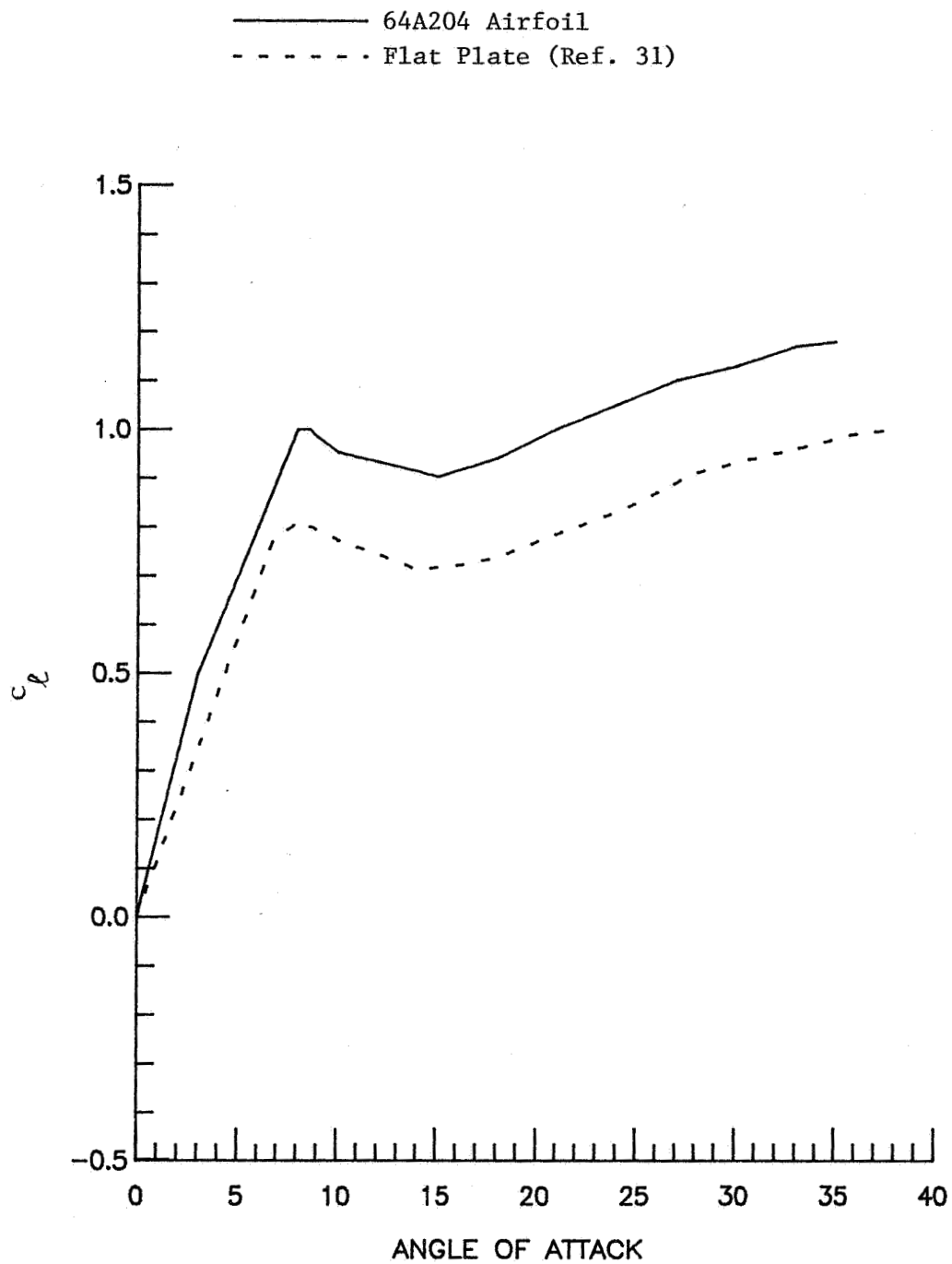
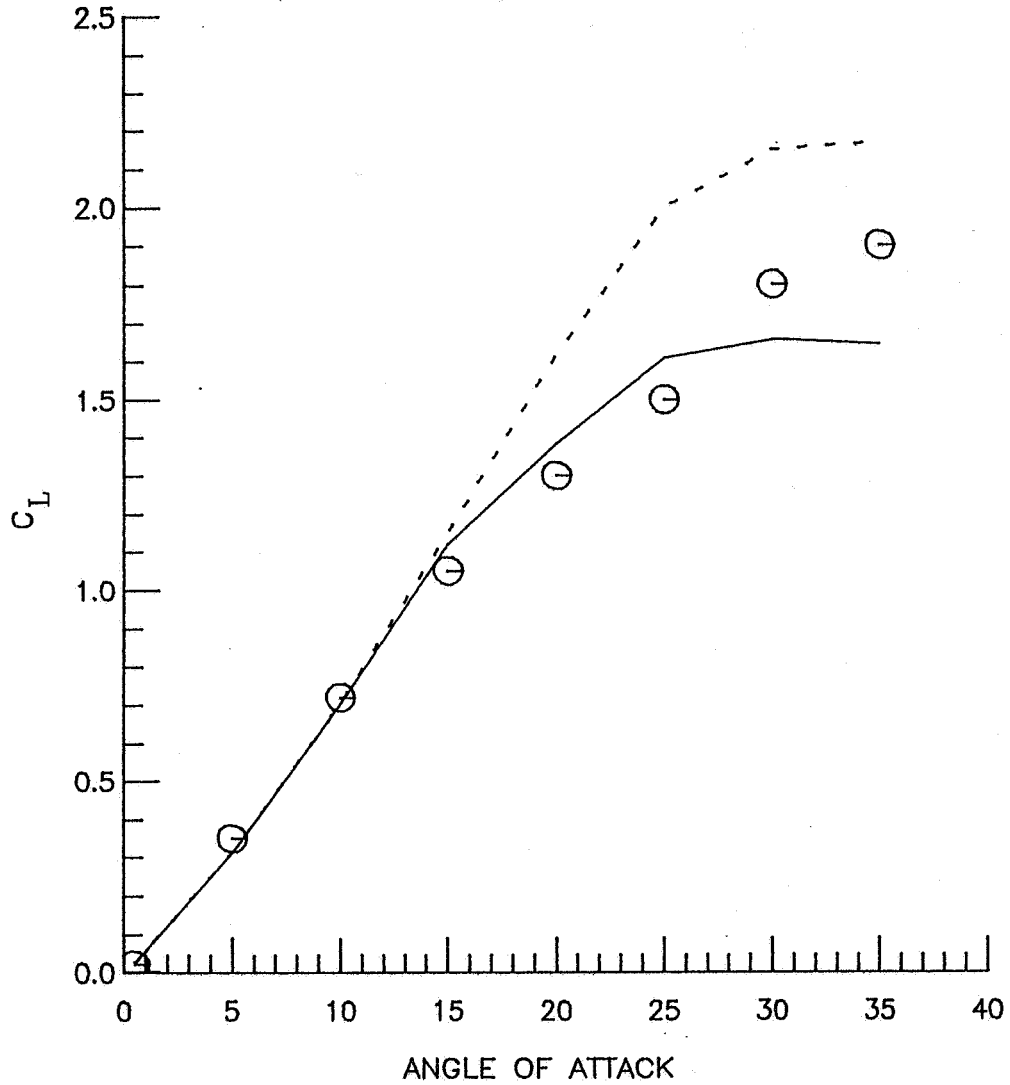


Figure 24. Sectional Lift Curve for an NACA 64A204 Airfoil

- ⊖ — Experimental Data (Ref. 38)
- VORSTAB Calculation with Viscous Effect
- - - - VORSTAB Calculation without Viscous Effect



(a)  $C_L$  vs  $\alpha$

Figure 25. Longitudinal Aerodynamic Characteristics of an F-16 Configuration



⊖ — Experimental Data (Ref. 38)  
 — VORSTAB Calculation with Viscous Effect  
 - - - VORSTAB Calculation without Viscous Effect

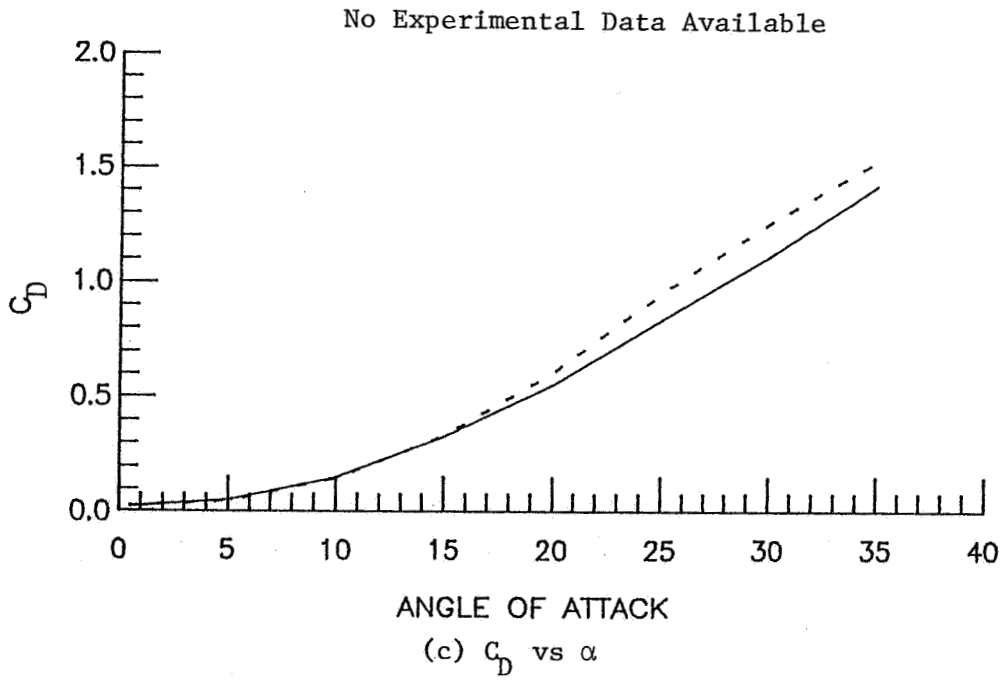
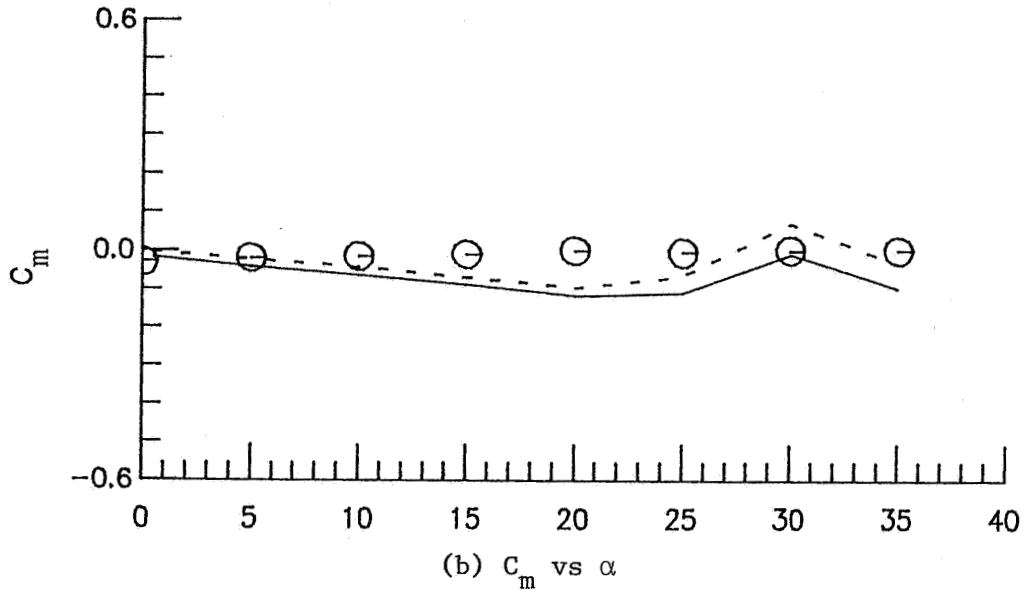


Figure 25. Continued

- — Experimental Data (Ref. 38)
- VORSTAB Calculation with Viscous Effect
- - - VORSTAB Calculation without Viscous Effect

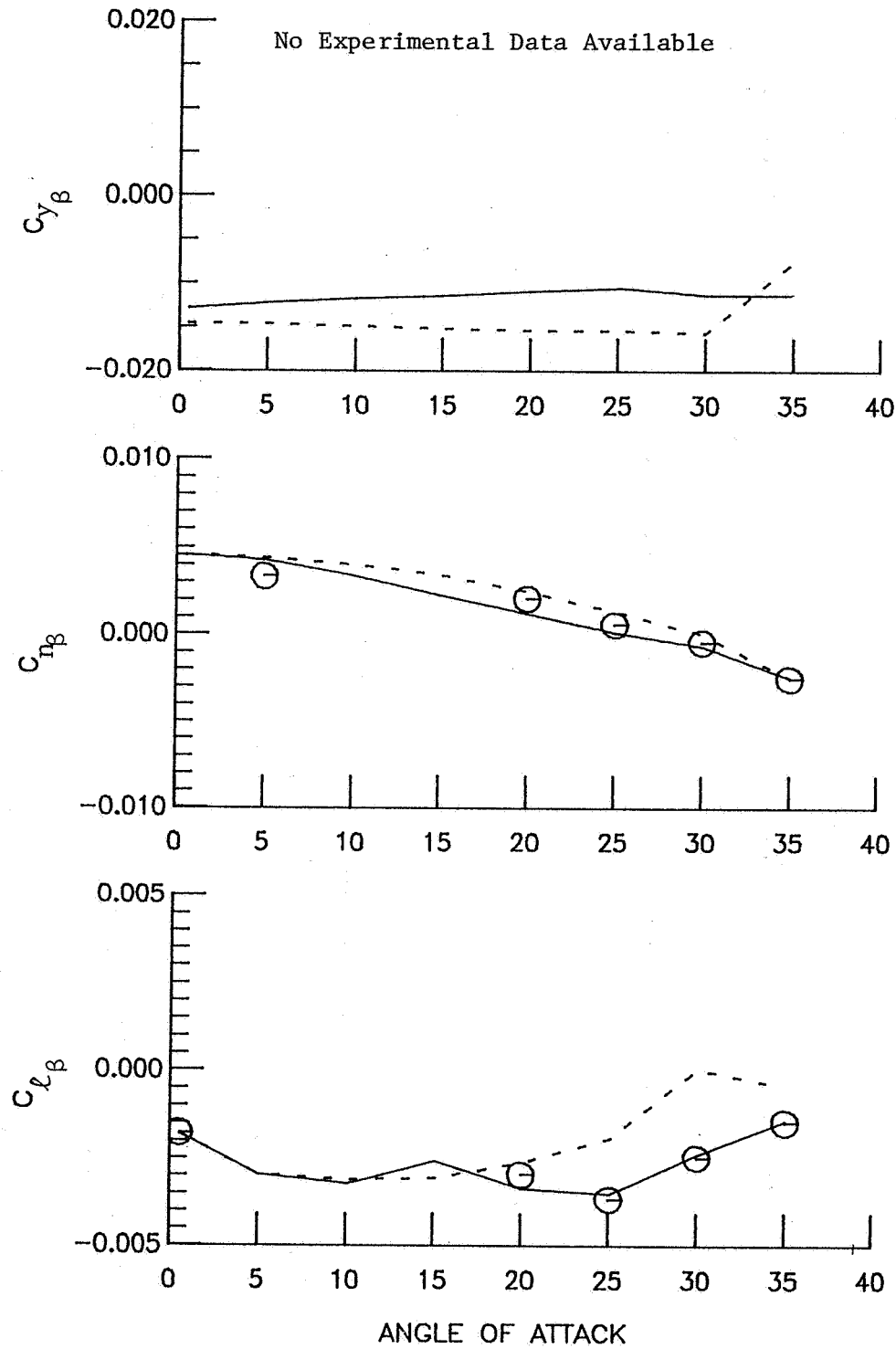
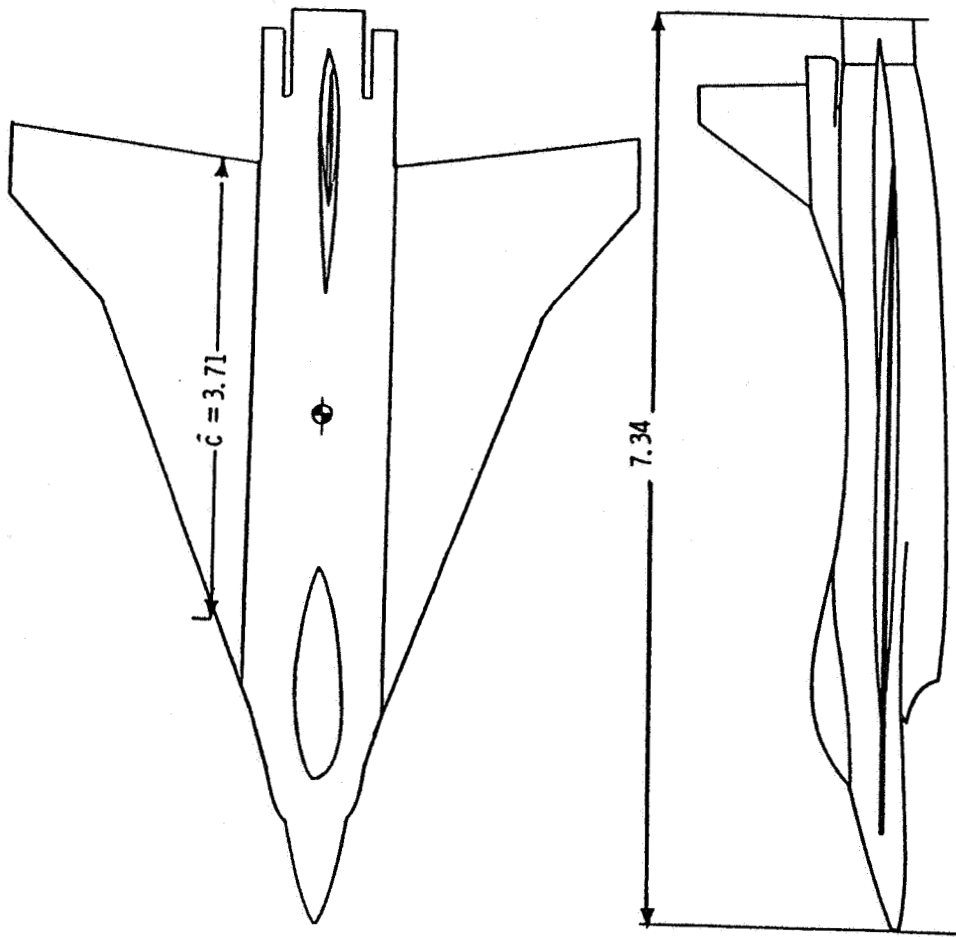


Figure 26. Lateral-Directional Derivatives Calculation of an F-16 Configuration Based on the Body Axis at  $\beta = 5$  Degrees



Dimensions are given in feet.

Pitch Center at  $0.45\bar{c}$

Figure 27. Three-view Sketch of the F-16XL Model (Ref. 39)

⊖— Experimental Data (Ref. 39)  
— VORSTAB Calculation without Viscous Effect

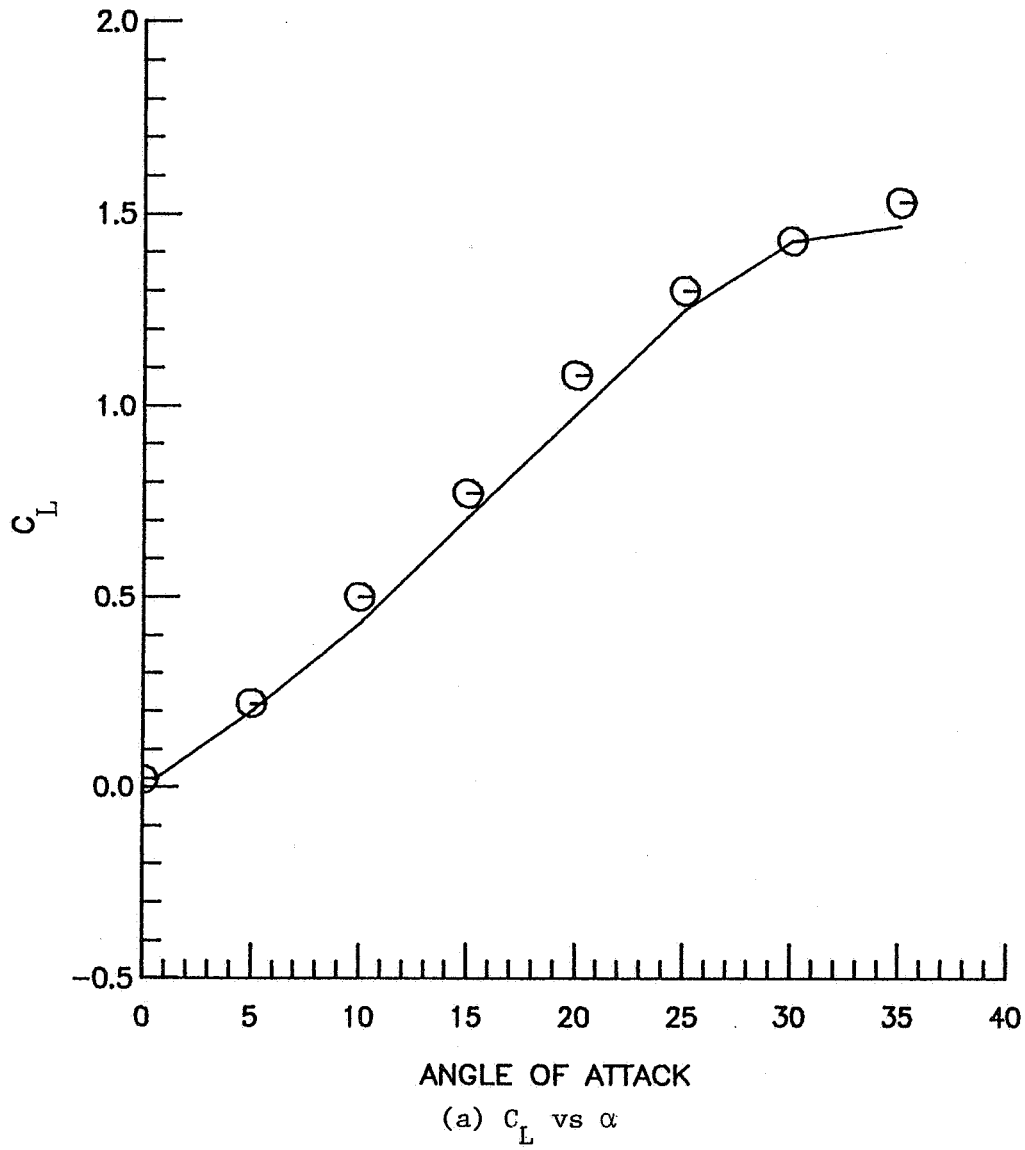


Figure 28. Longitudinal Aerodynamic Characteristics of an F-16XL Configuration

⊖ — Experimental Data (Ref. 39)  
— — — — — VORSTAB Calculation without Viscous Effect

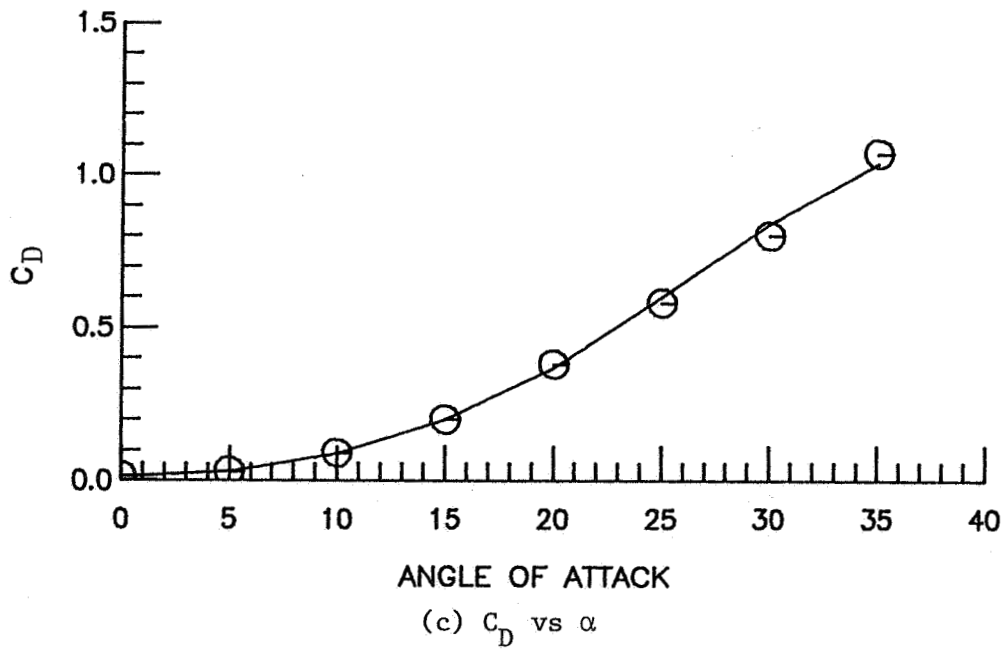
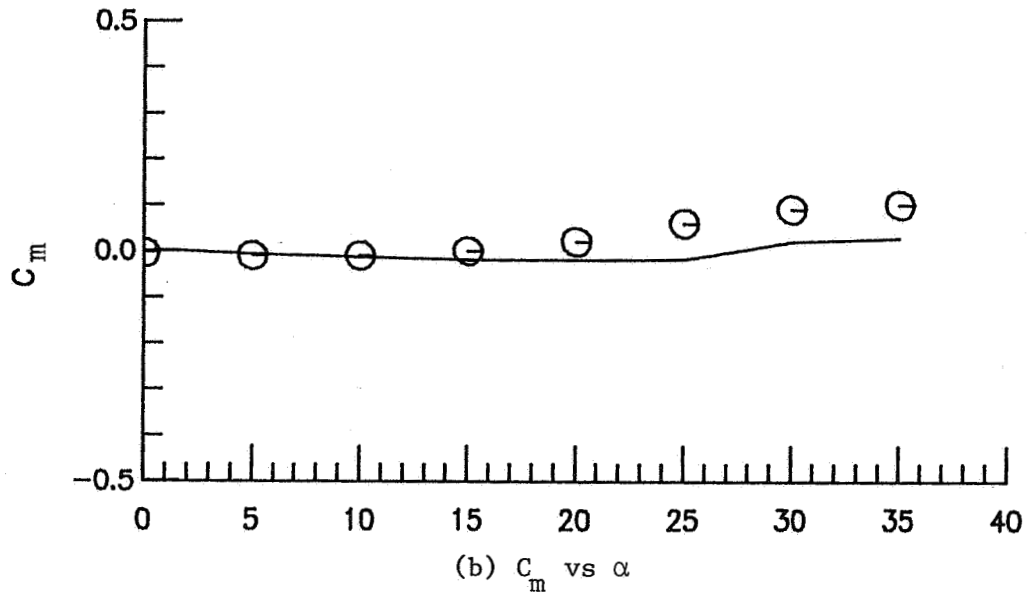


Figure 28. Continued

$\ominus$  — Experimental Data (Ref. 39)  
 ——— VORSTAB Calculation without Viscous Effect

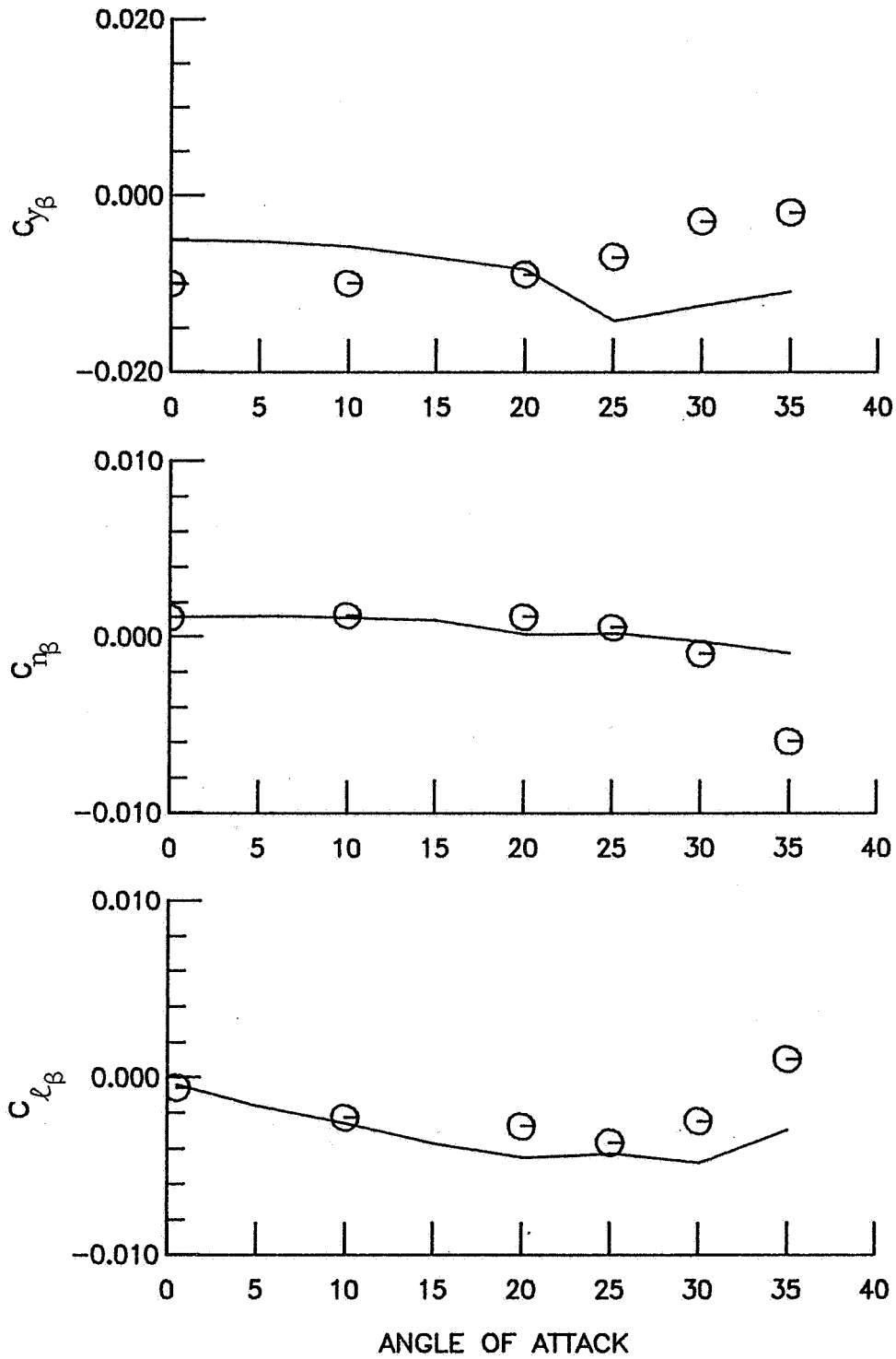
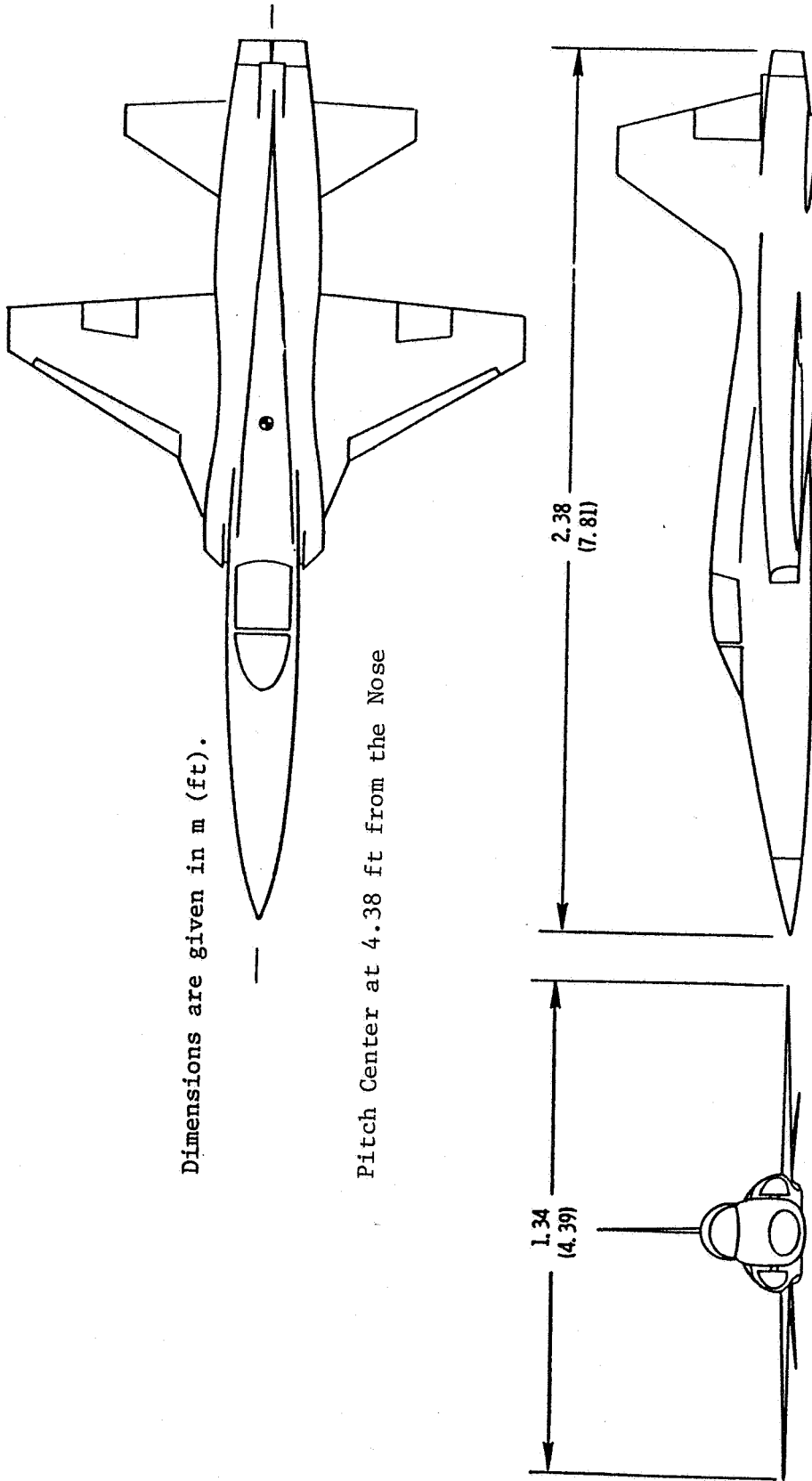


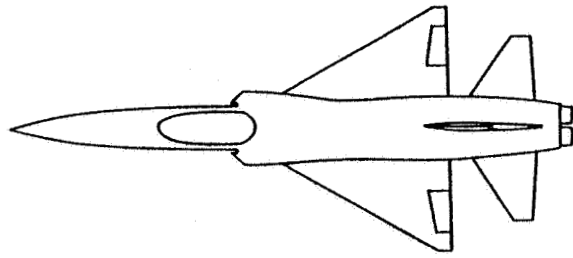
Figure 29. Lateral-Directional Derivatives Calculation of an F-16XL Configuration Based on the Body Axis at  $\beta = 5$  Degrees



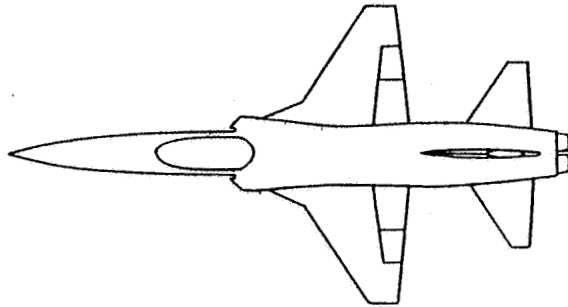
Dimensions are given in m (ft).

Pitch Center at 4.38 ft from the Nose

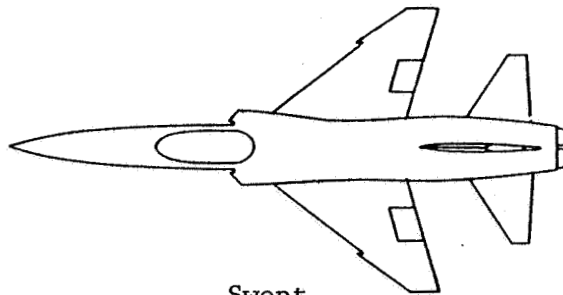
Figure 30. Three-view Sketch of the F-5 Basic Model (Ref. 40)



Delta



Basic



Swept

Figure 31. Top-view Sketches of the F-5 Configurations (Ref. 40)



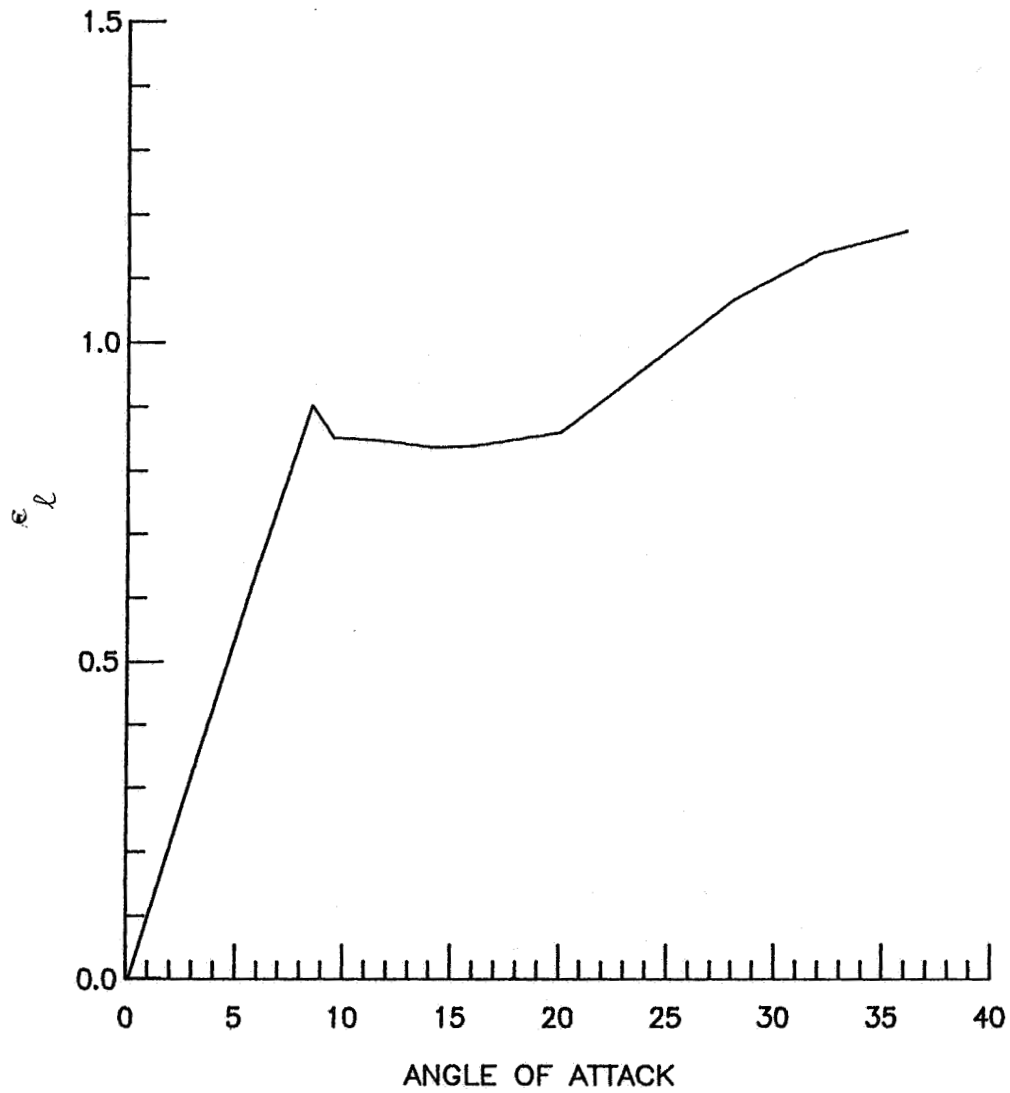


Figure 32. Sectional Lift Curve for the F-5 Configuration

⊖ — Experimental Data (Ref. 40)  
 ——— VORSTAB, with Viscous Effect  
 - - - - - VORSTAB, without Viscous Effect

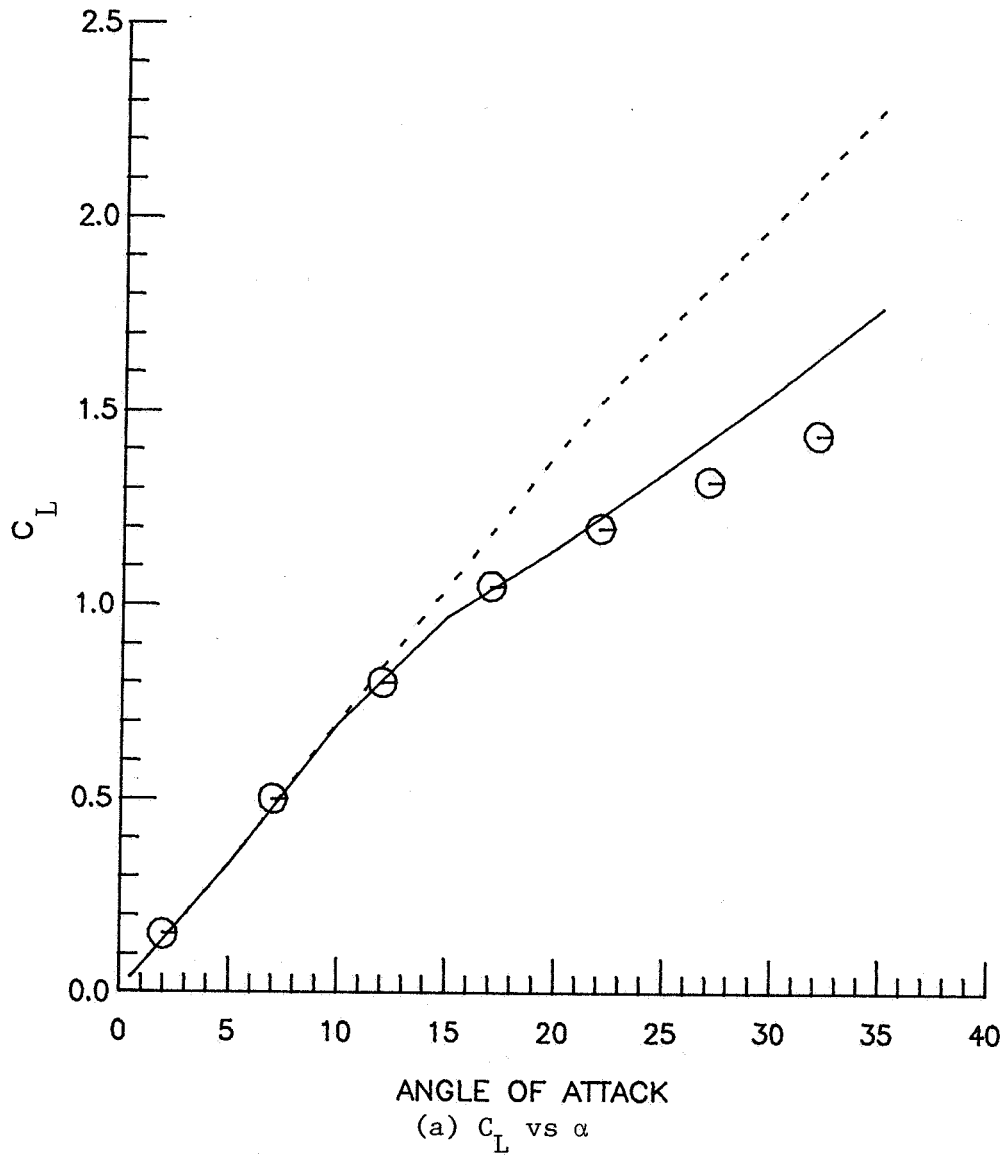


Figure 33. Longitudinal Aerodynamic Characteristics of an F-5 Basic Configuration

⊖ — Experimental Data (Ref. 40)  
 ——— VORSTAB Calculation with Viscous Effect  
 - - - - - VORSTAB Calculation without Viscous Effect

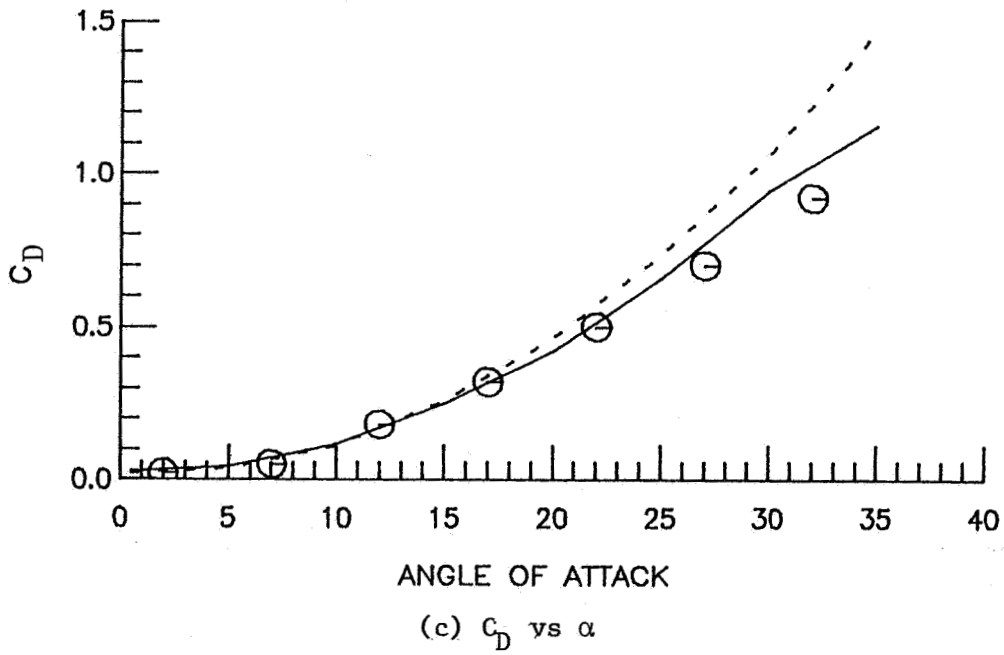
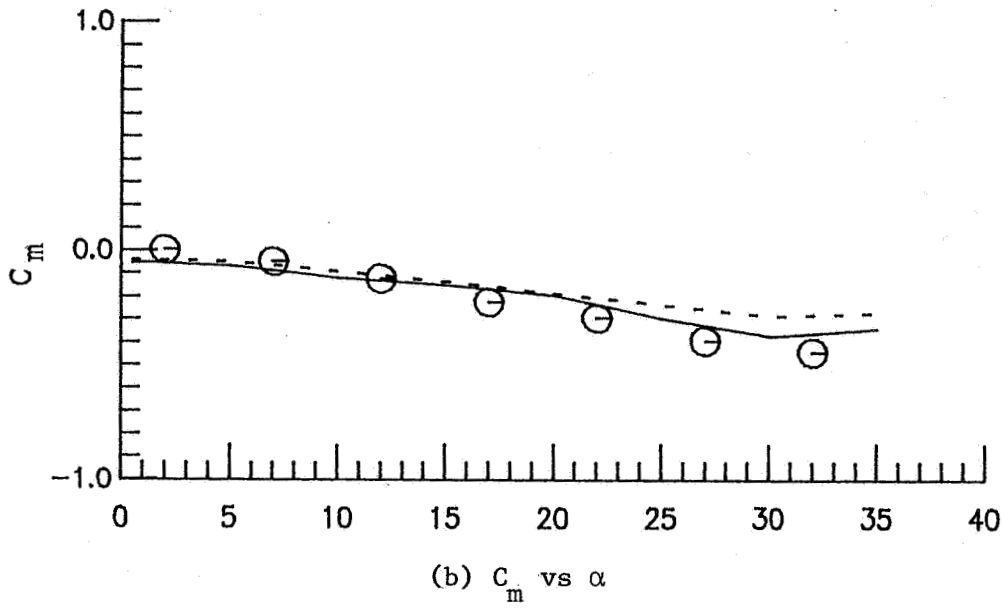


Figure 33. Continued

⊖ — Experimental Data (Ref. 40)  
 ——— VORSTAB Calculation with Viscous Effect  
 - - - - - VORSTAB Calculation without Viscous Effect

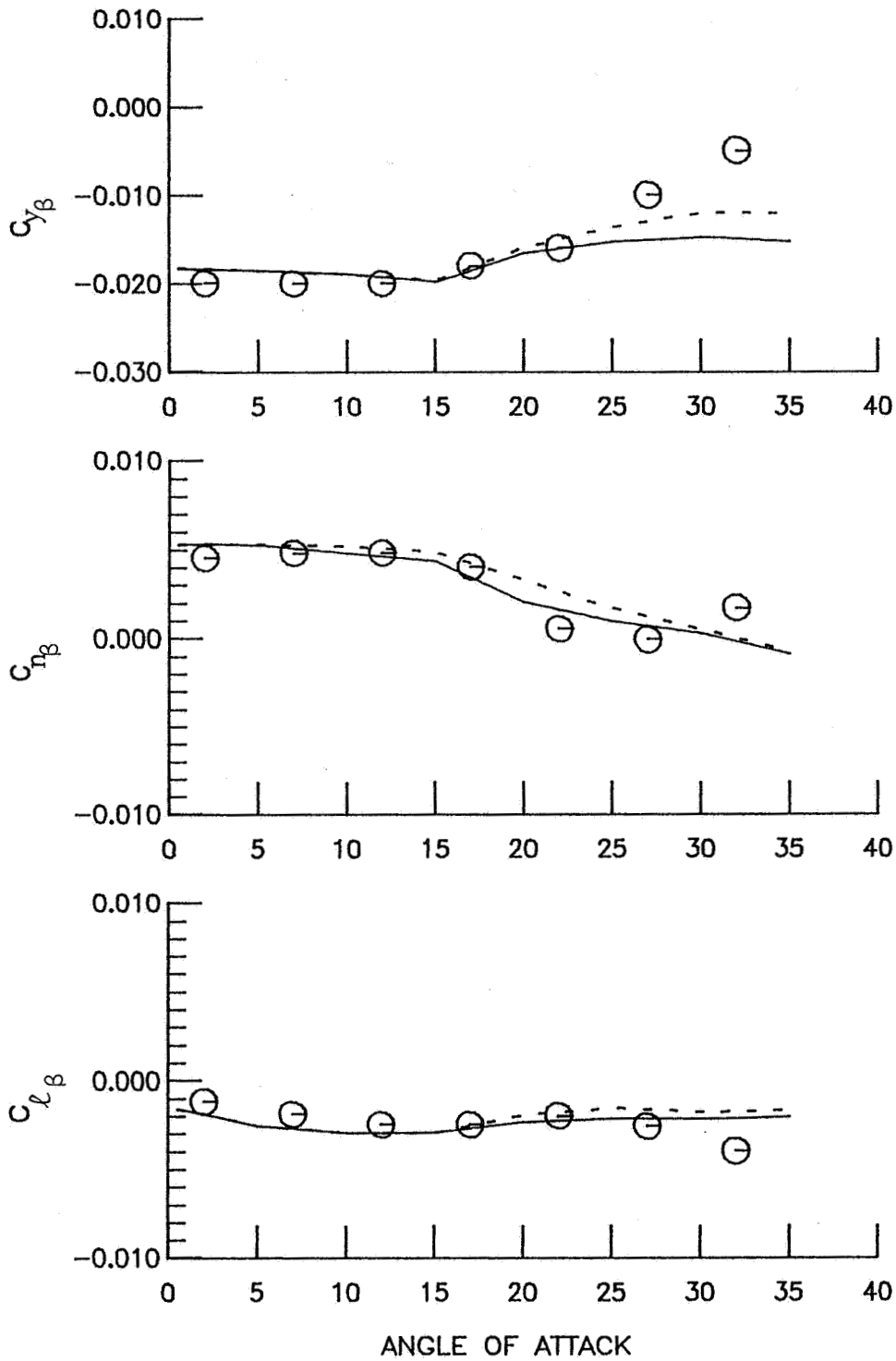
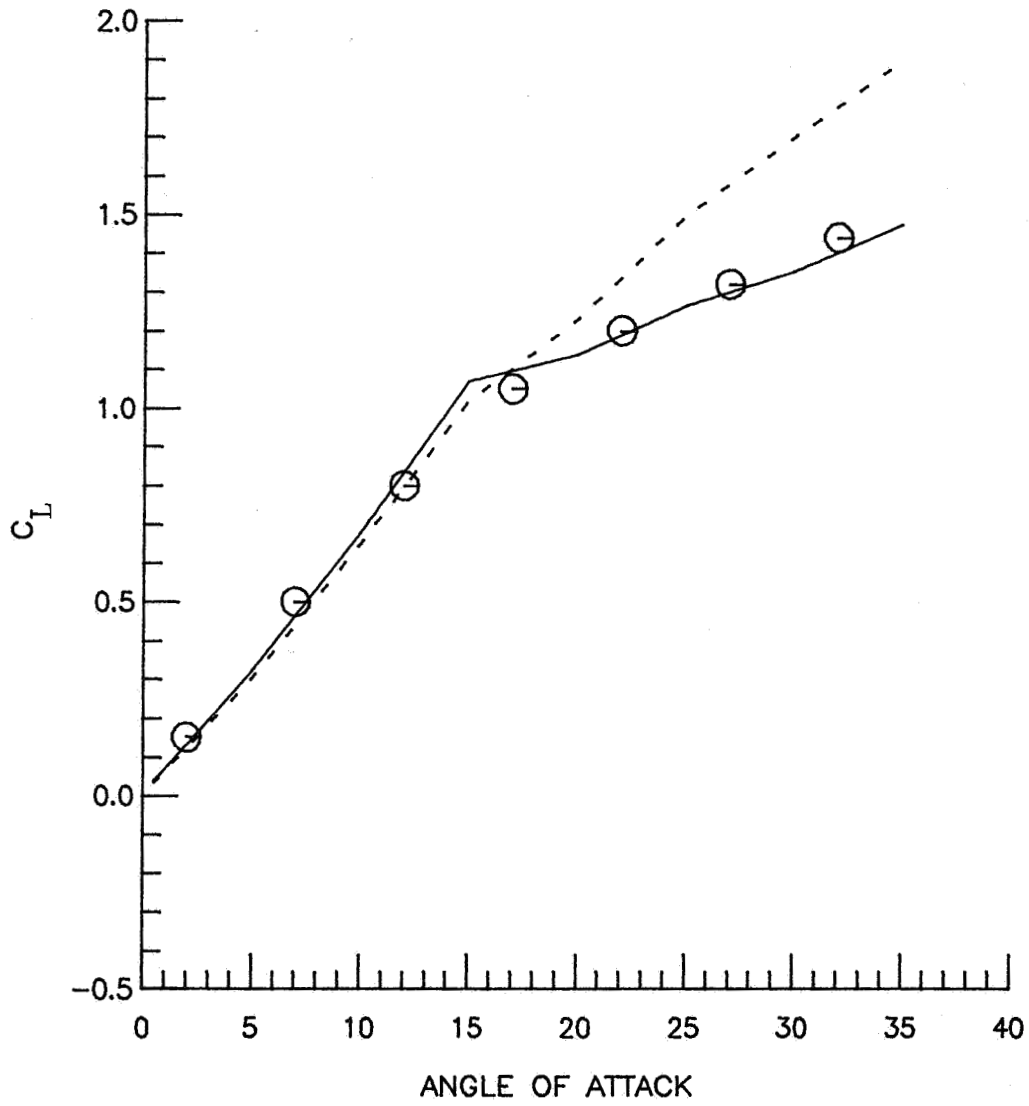


Figure 34. Lateral-Directional Derivatives Calculation of an F-5 Basic Configuration Based on the Body Axis at  $\beta = 5$  Degrees

⊖ — Experimental Data (Ref. 40)  
 ——— VORSTAB, with Viscous Effect  
 - - - - VORSTAB, without Viscous Effect



(a)  $C_L$  vs  $\alpha$

Figure 35. Longitudinal Aerodynamic Characteristics of an F-5 Swept Wing Configuration

○ — Experimental Data (Ref. 40)  
 ——— VORSTAB Calculation with Viscous Effect  
 - - - - VORSTAB Calculation without Viscous Effect

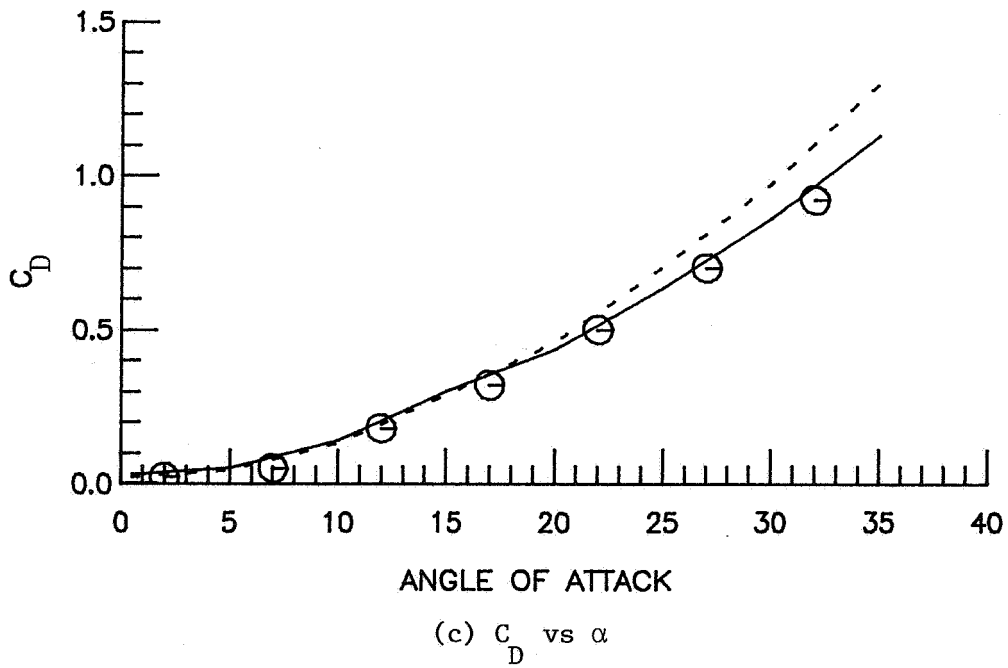
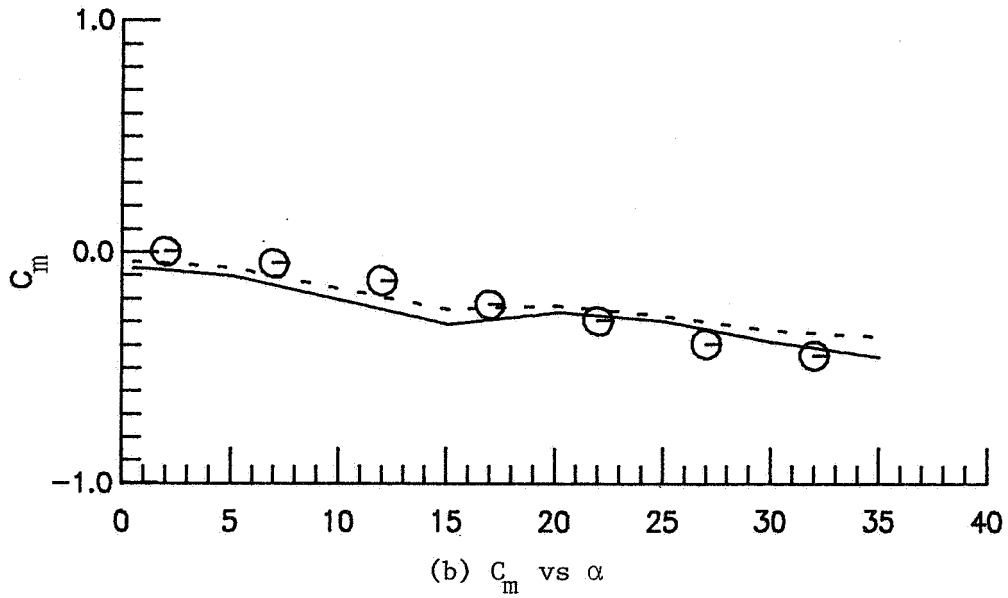


Figure 35. Continued

○— Experimental Data (Ref. 40)  
 ——— VORSTAB, with Viscous Effect  
 - - - - - VORSTAB, without Viscous Effect

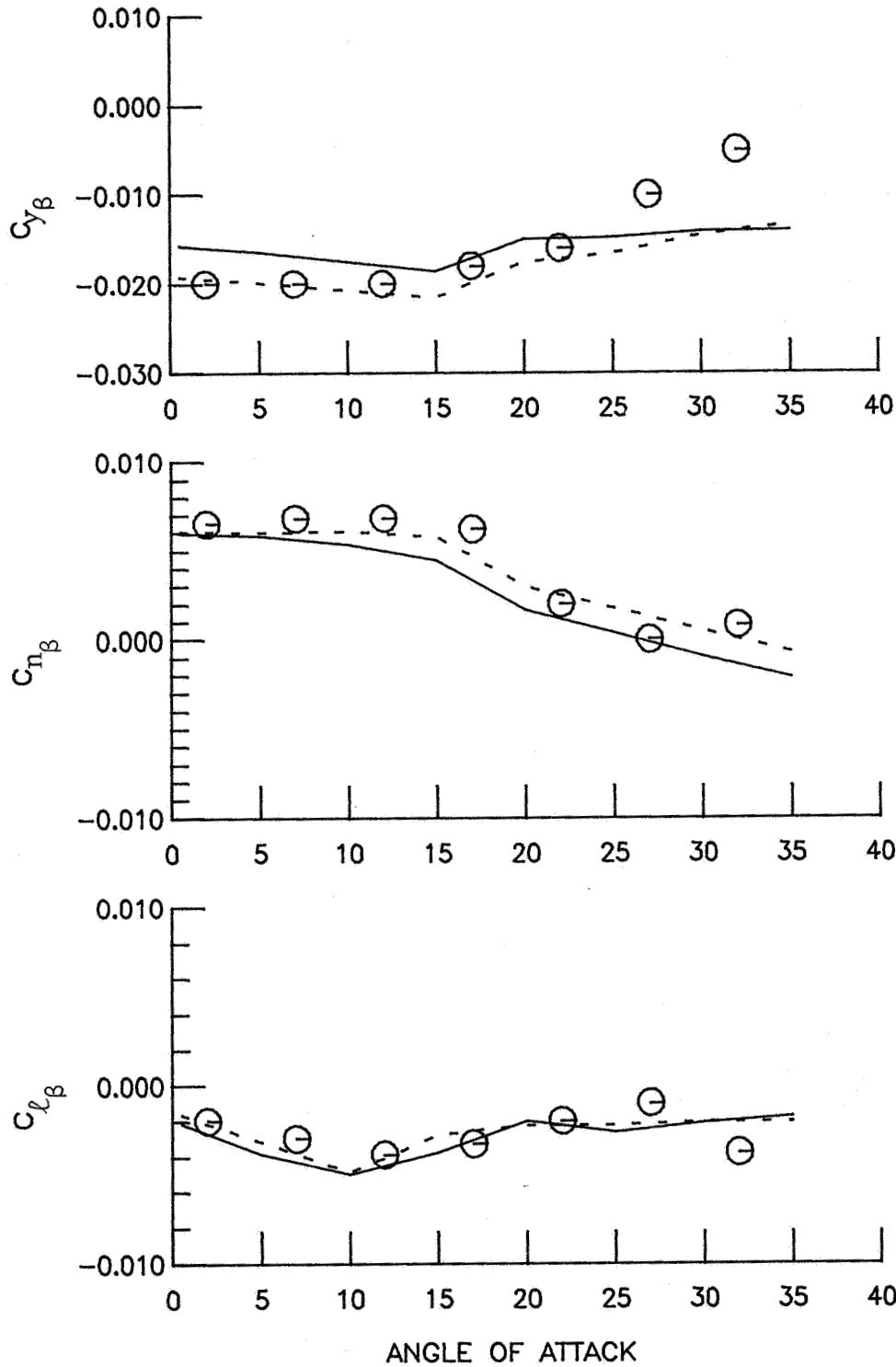


Figure 36. Lateral-Directional Derivatives of an F-5 Swept Wing Configuration Based on the Body Axis at  $\beta = 5$  Degrees

⊖ — Experimental Data (Ref. 40)  
— — — — — VORSTAB Calculation without Viscous Effect

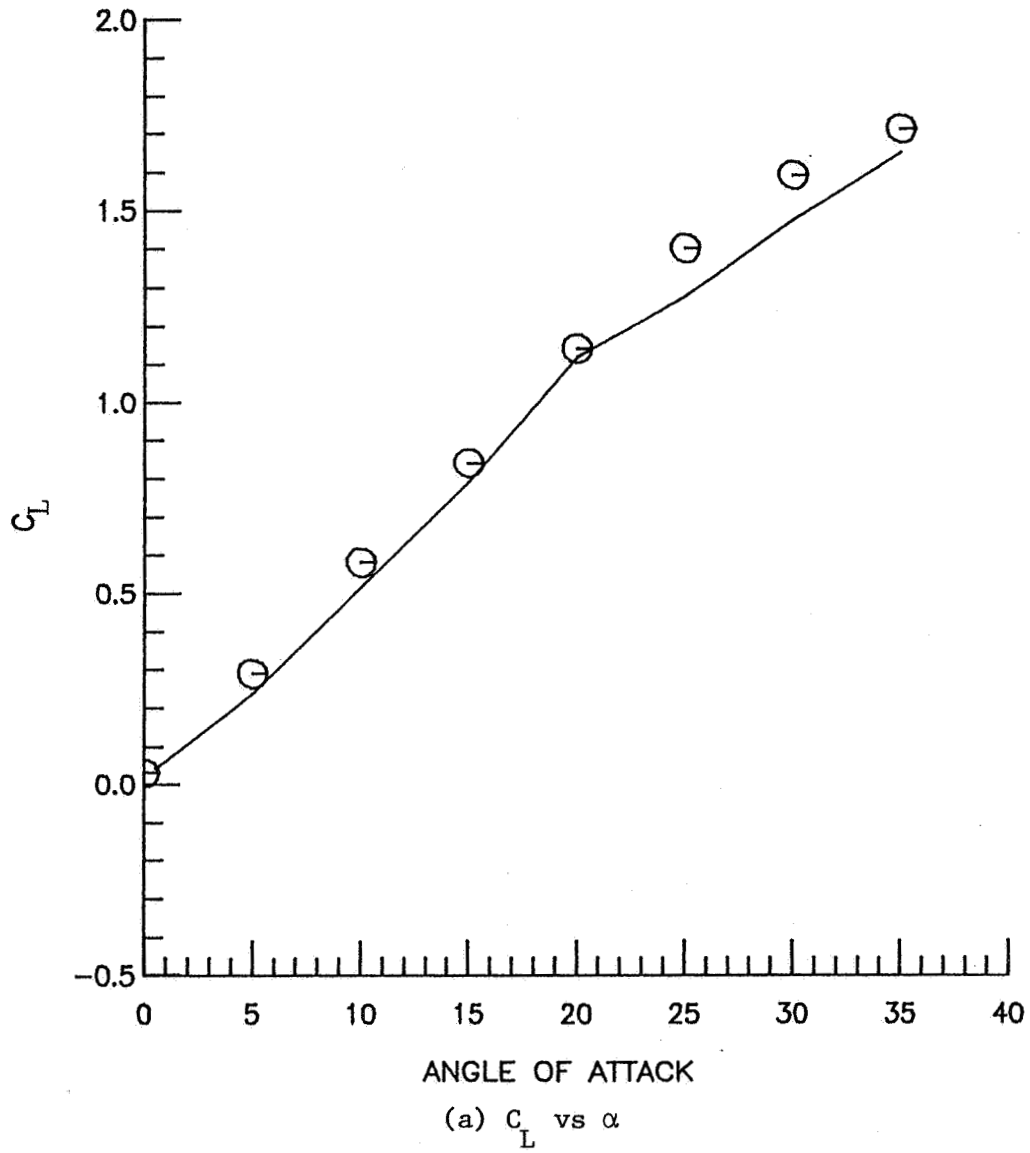


Figure 37. Longitudinal Aerodynamic Characteristics of an F-5 Delta Wing Configuration



$\ominus$ — Experimental Data (Ref. 40)  
 ——— VORSTAB Calculation without Viscous Effect

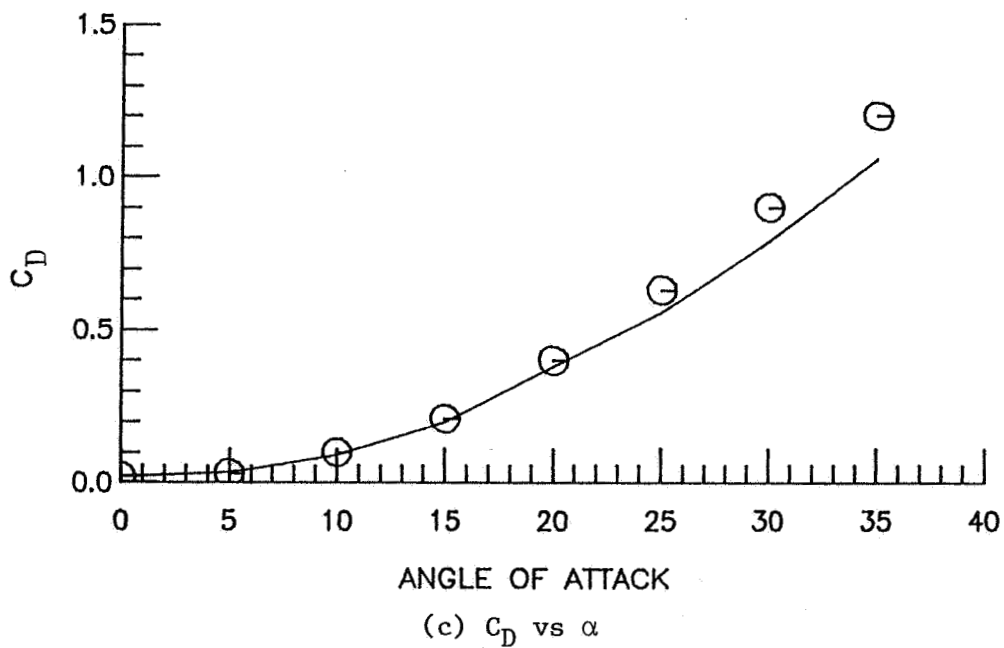
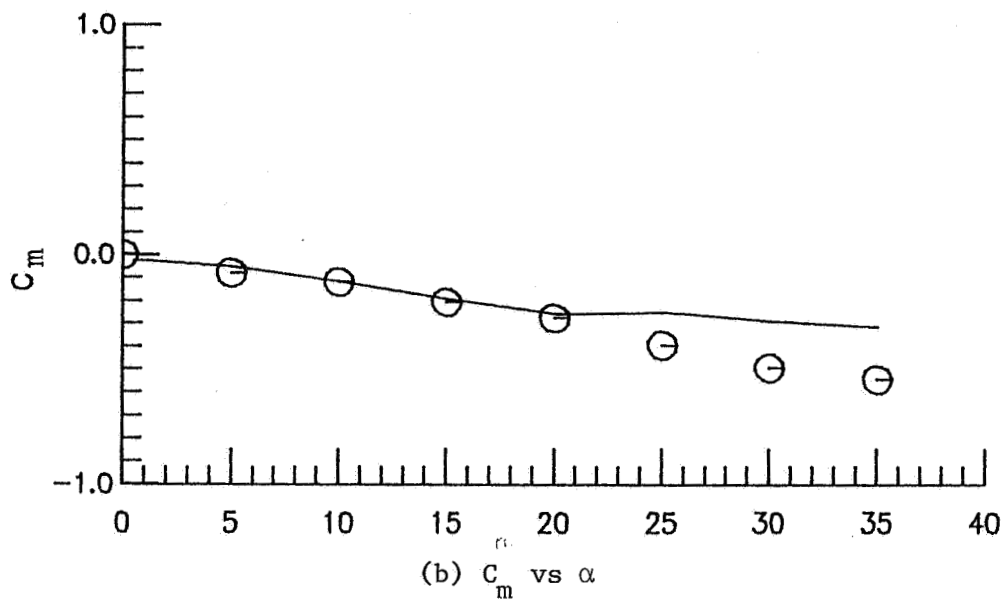


Figure 37. Continued

$\ominus$  — Experimental Data (Ref. 40)  
 ——— VORSTAB Calculation without Viscous Effect

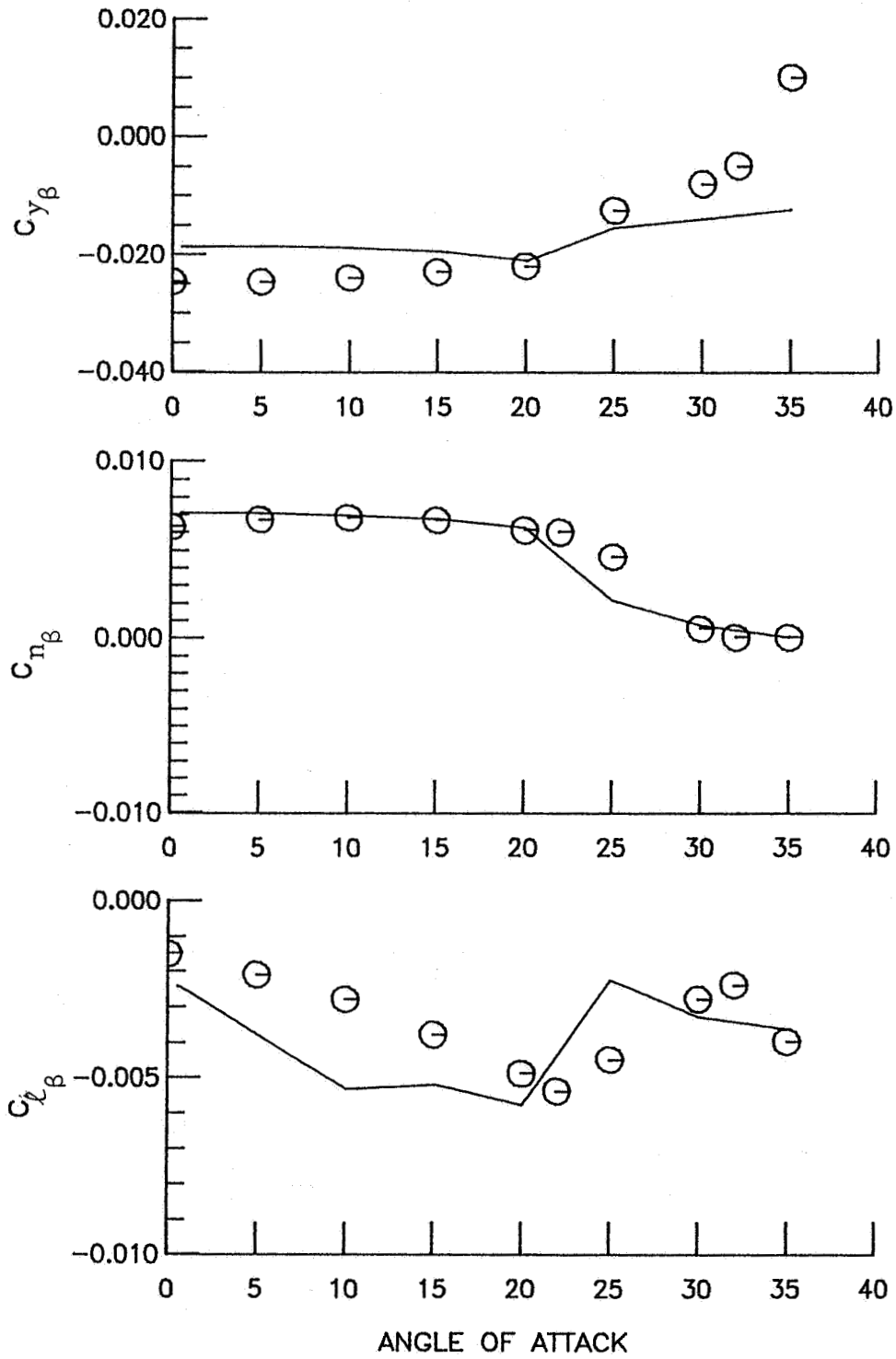


Figure 38. Lateral-Directional Derivatives Calculation of an F-5 Delta Wing Configuration Based on the Body Axis at  $\beta = 5$  Degrees

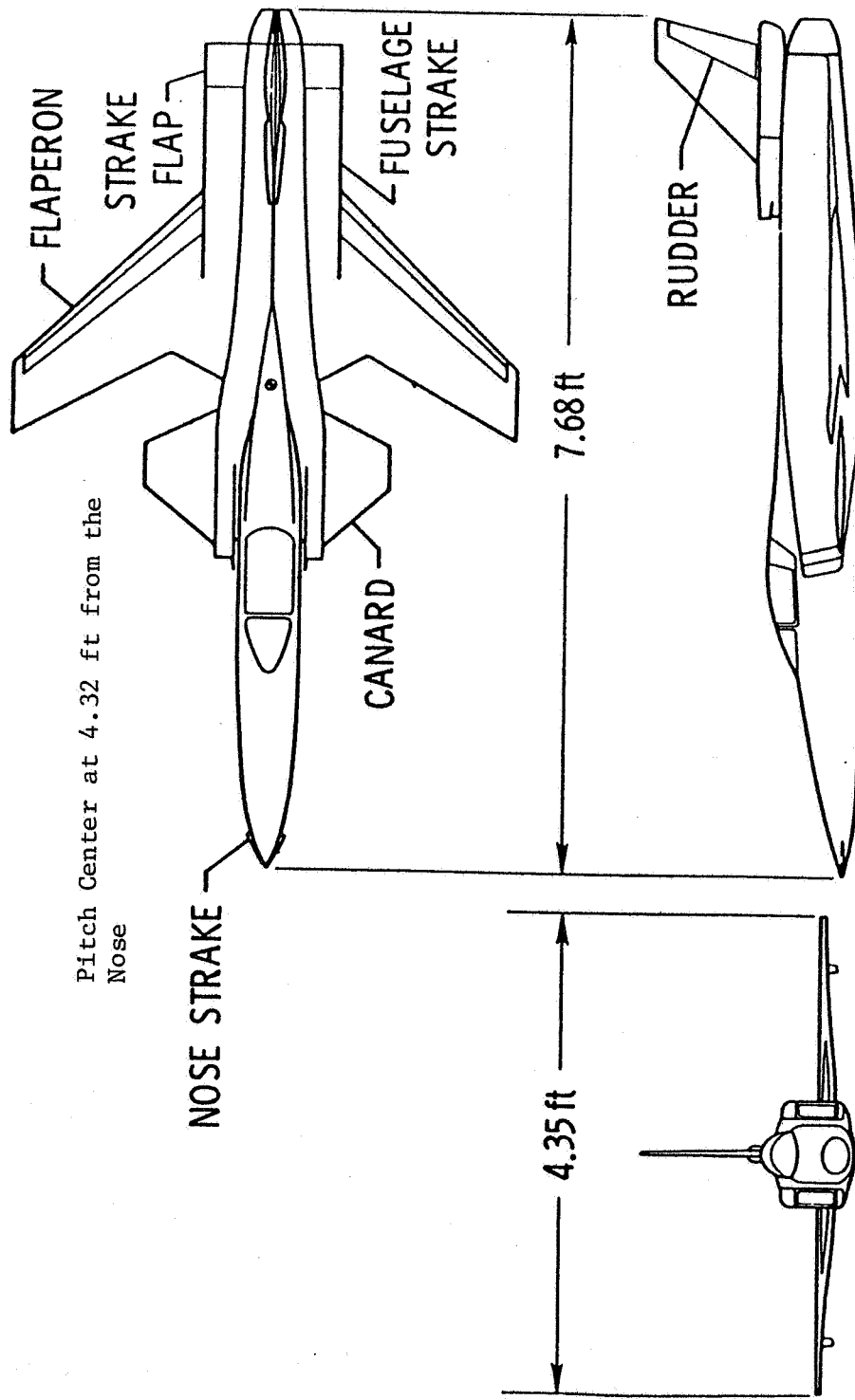
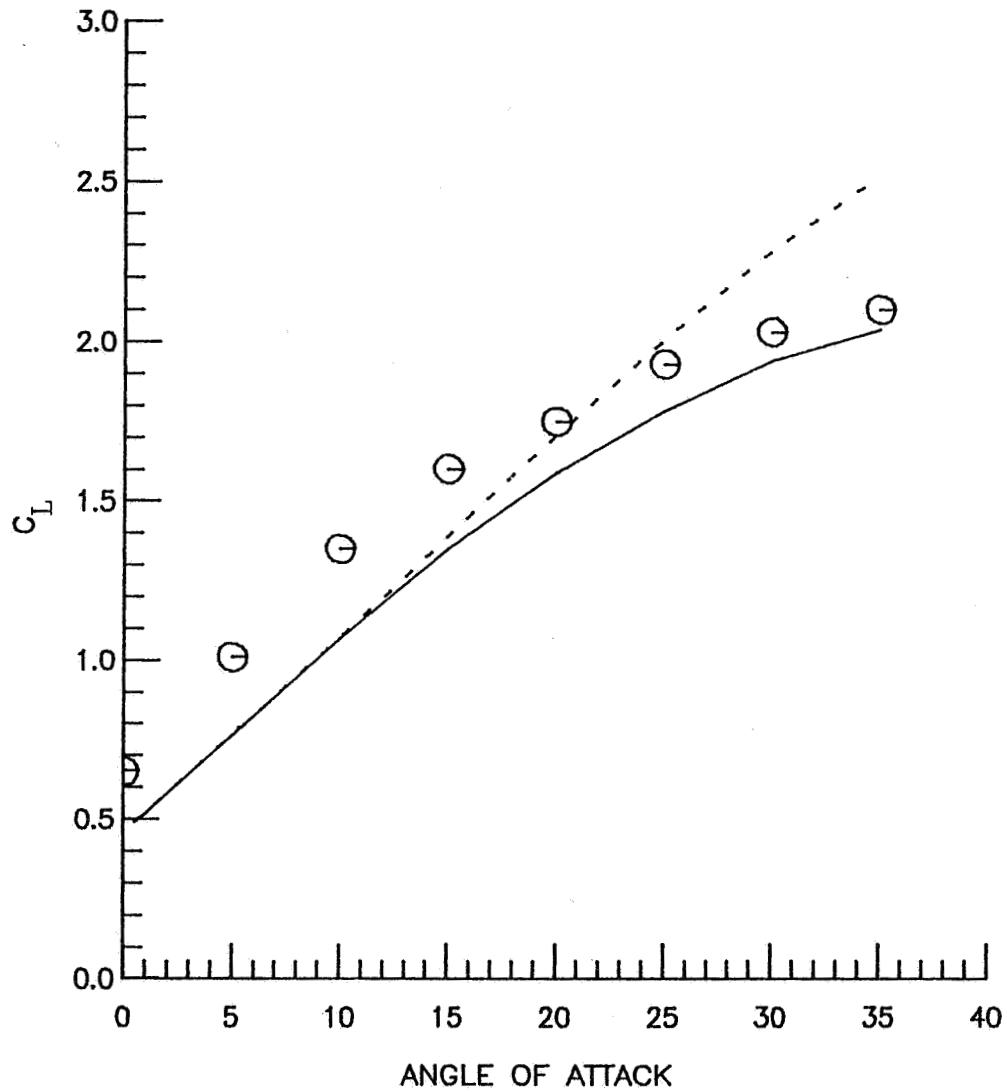


Figure 39. Three-view Sketch of the X-29 Model 1 (Ref. 41)

⊖ — Experimental Data (Ref. 41)  
 — VORSTAB Calculation with Vortex Breakdown Effect  
 - - - - VORSTAB Calculation without Vortex Breakdown Effect



(a)  $C_L$  vs  $\alpha$

Figure 40. Longitudinal Aerodynamic Characteristics of an X-29 Configuration

⊖ — Experimental Data (Ref. 41)  
 — VORSTAB Calculation with Vortex Breakdown Effect  
 - - - VORSTAB Calculation without Vortex Breakdown Effect

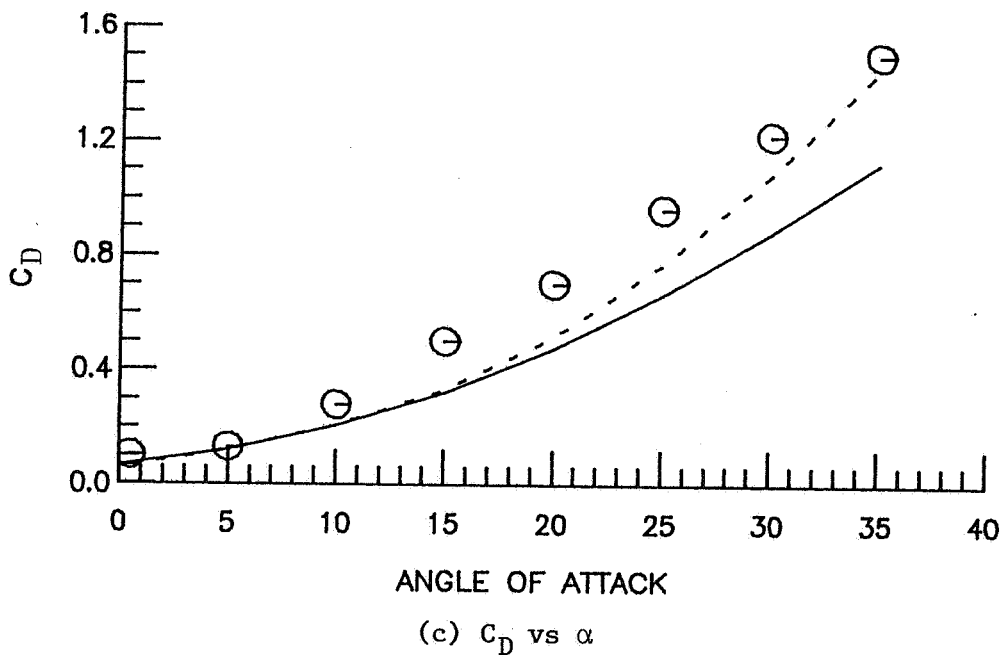
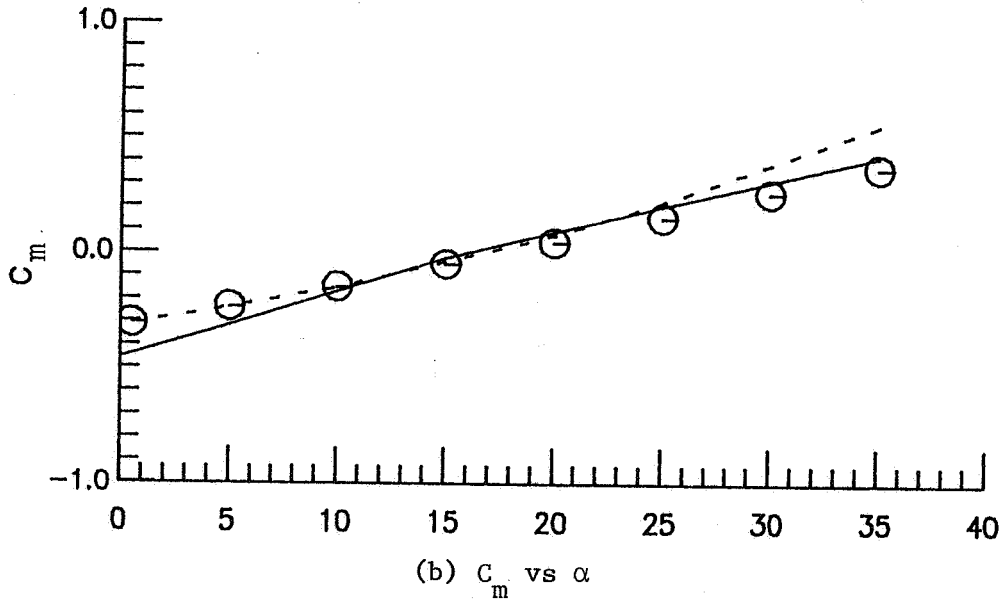


Figure 40. Continued

⊖ — Experimental Data (Ref. 41)  
 — VORSTAB Calculation with Vortex Breakdown Effect  
 - - - VORSTAB Calculation without Vortex Breakdown Effect

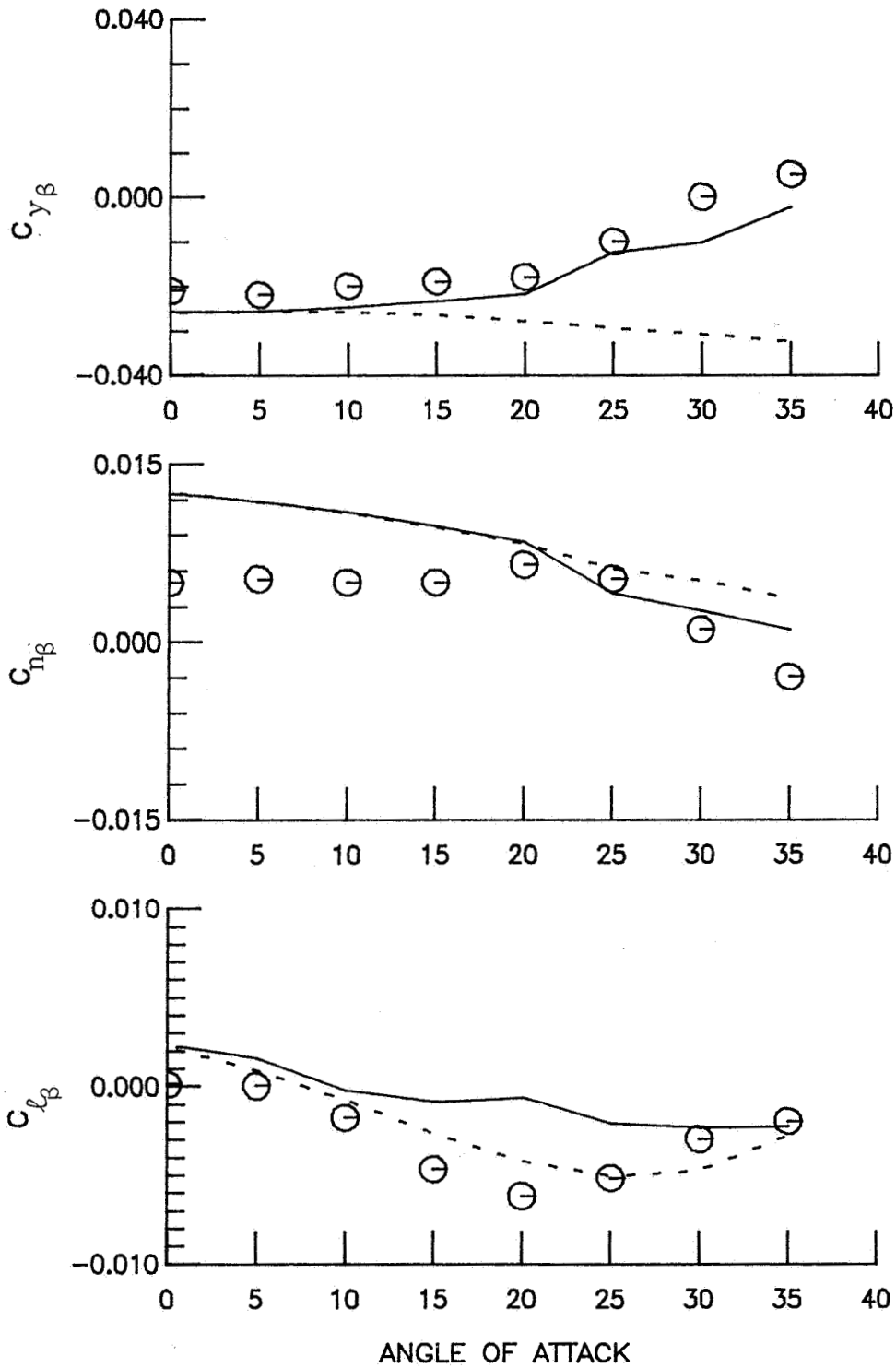


Figure 41. Lateral-Directional Derivatives Calculation of an X-29 Configuration Based on the Body Axis at  $\beta = 5$  Degrees

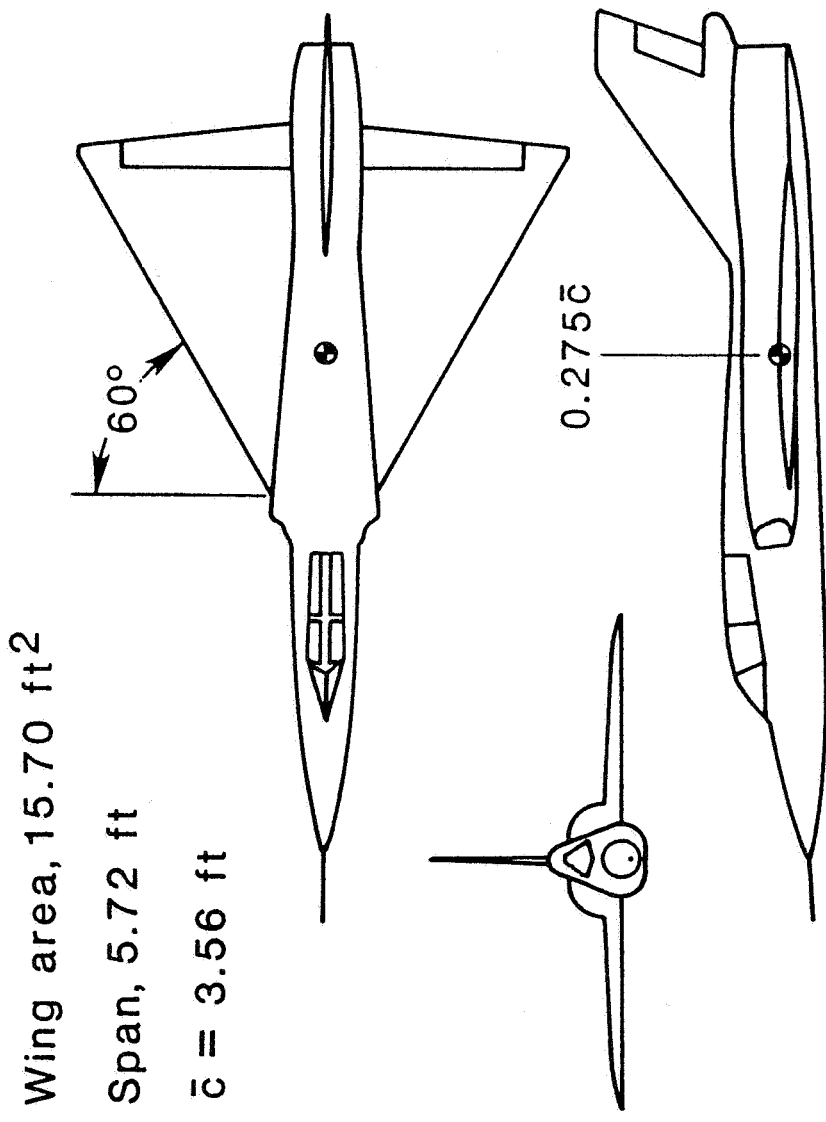


Figure 42. Three-view Sketch of the F-106B Configuration (Ref. 42)

⊖— Experimental Data (Ref. 42)  
—— VORSTAB Calculation without Viscous Effect

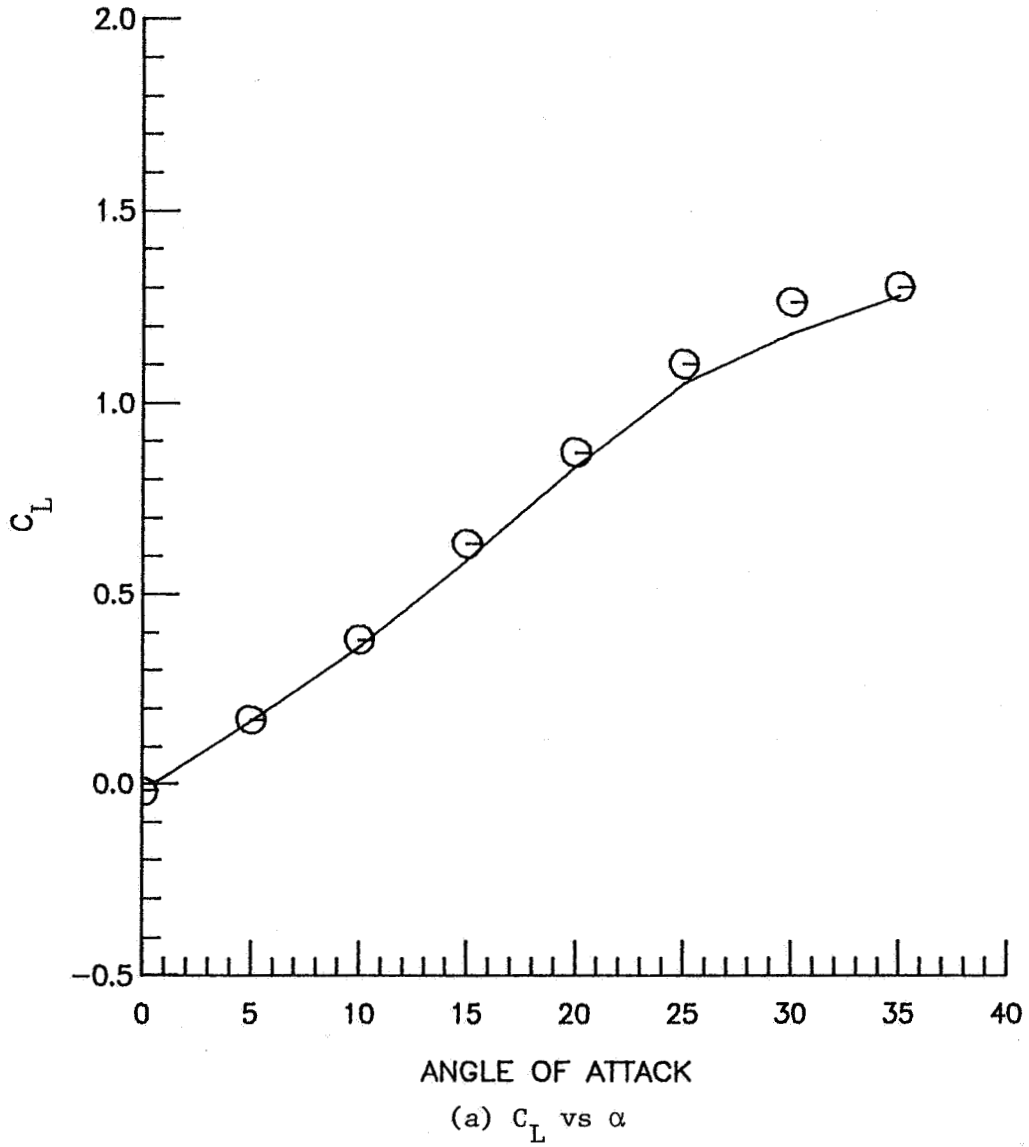


Figure 43. Longitudinal Aerodynamic Characteristics of an F-106B Basic Configuration



⊖ — Experimental Data (Ref. 42)  
 — VORSTAB Calculation without Viscous Effect

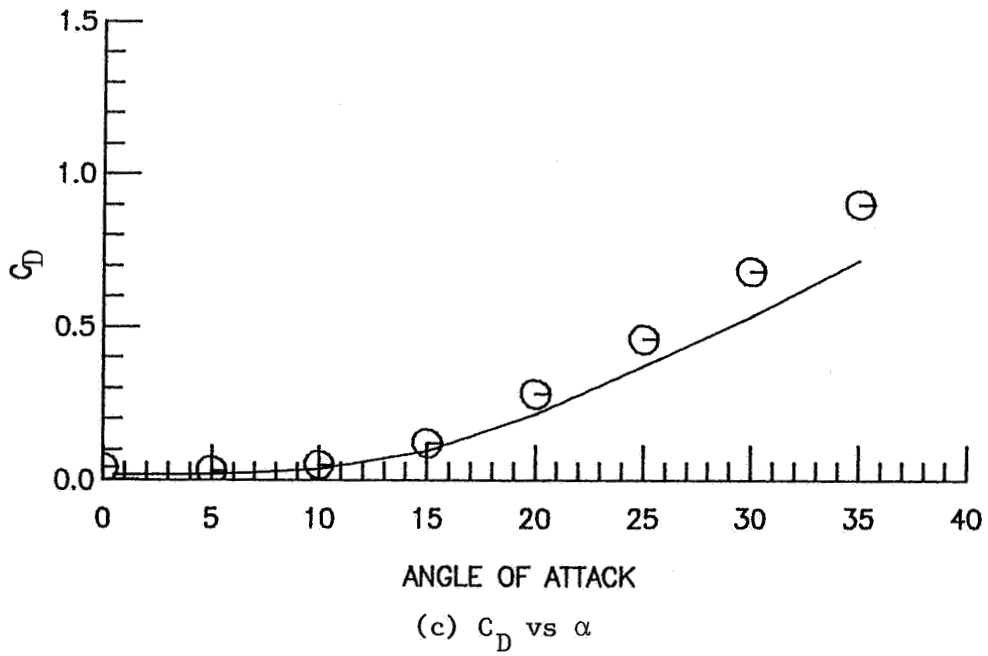
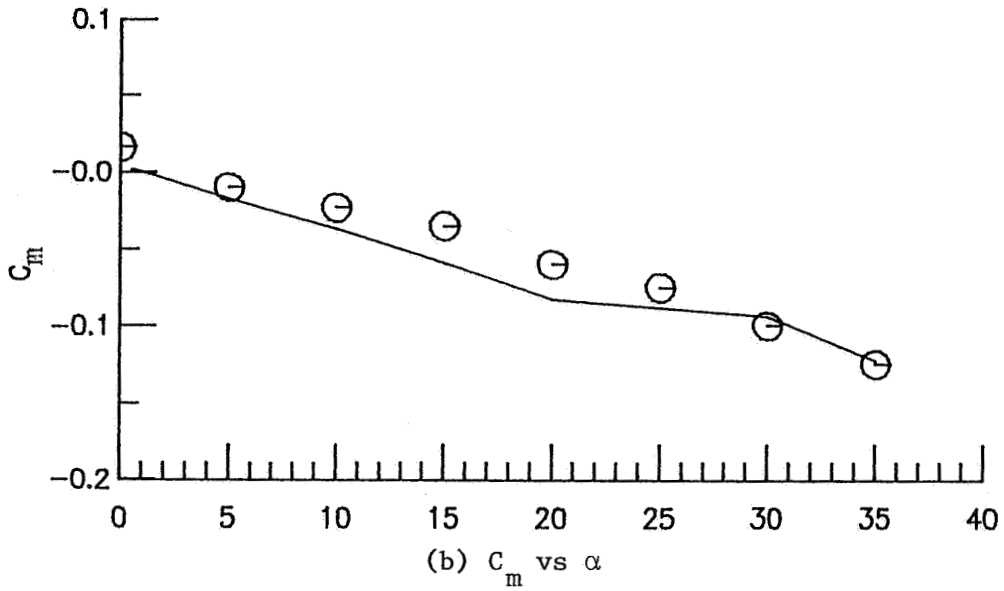


Figure 43. Continued

⊖ — Experimental Data (Ref. 42)  
 ———— VORSTAB Calculation without Viscous Effect

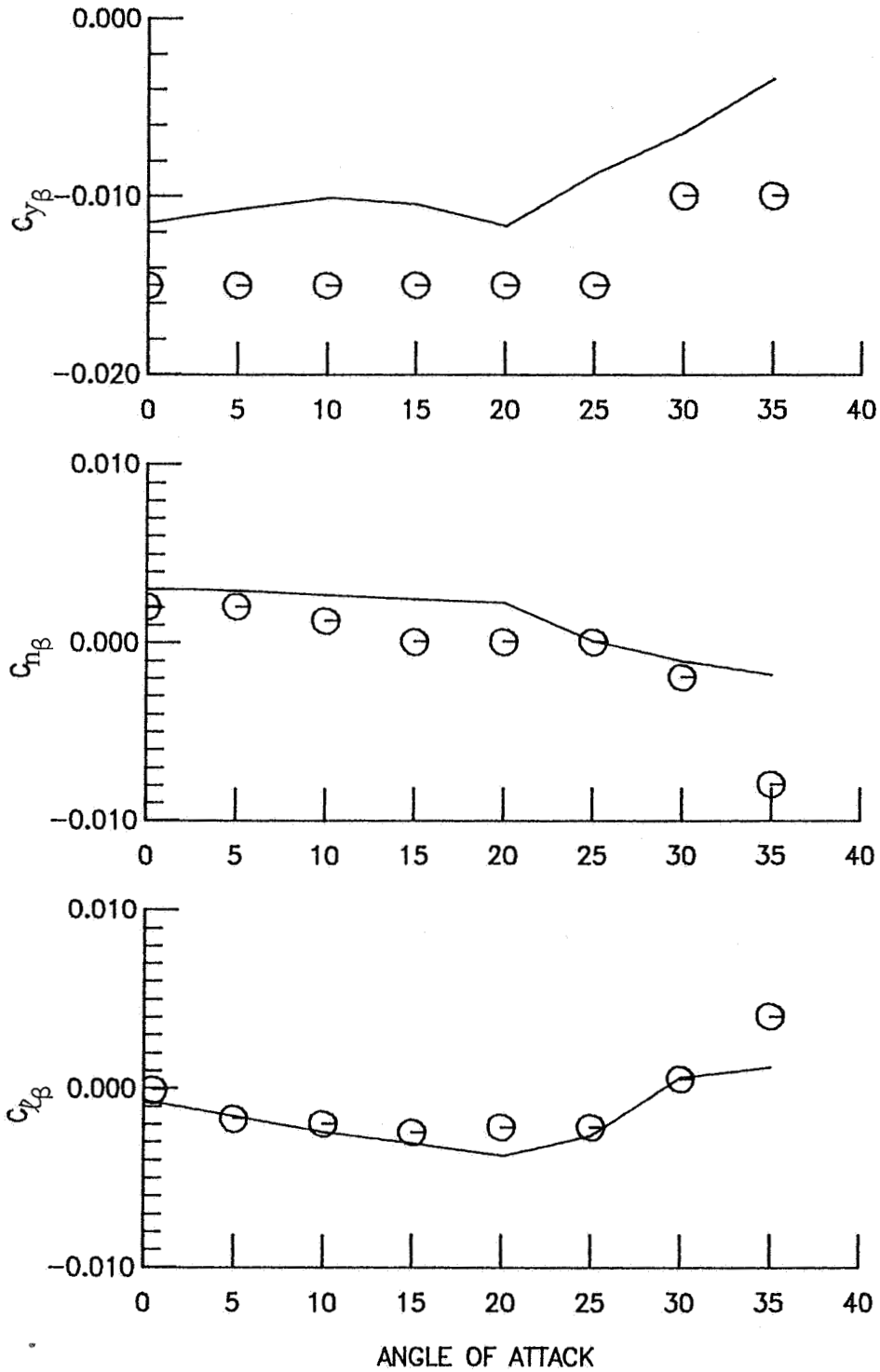


Figure 44. Lateral-Directional Derivatives Calculation of an F-106B Configuration Based on the Body Axis at  $\beta = 5$  Degrees

$\ominus$ — Forced Oscillation Data (Ref. 42)  
 ——— VORSTAB Calculation without Viscous Effect

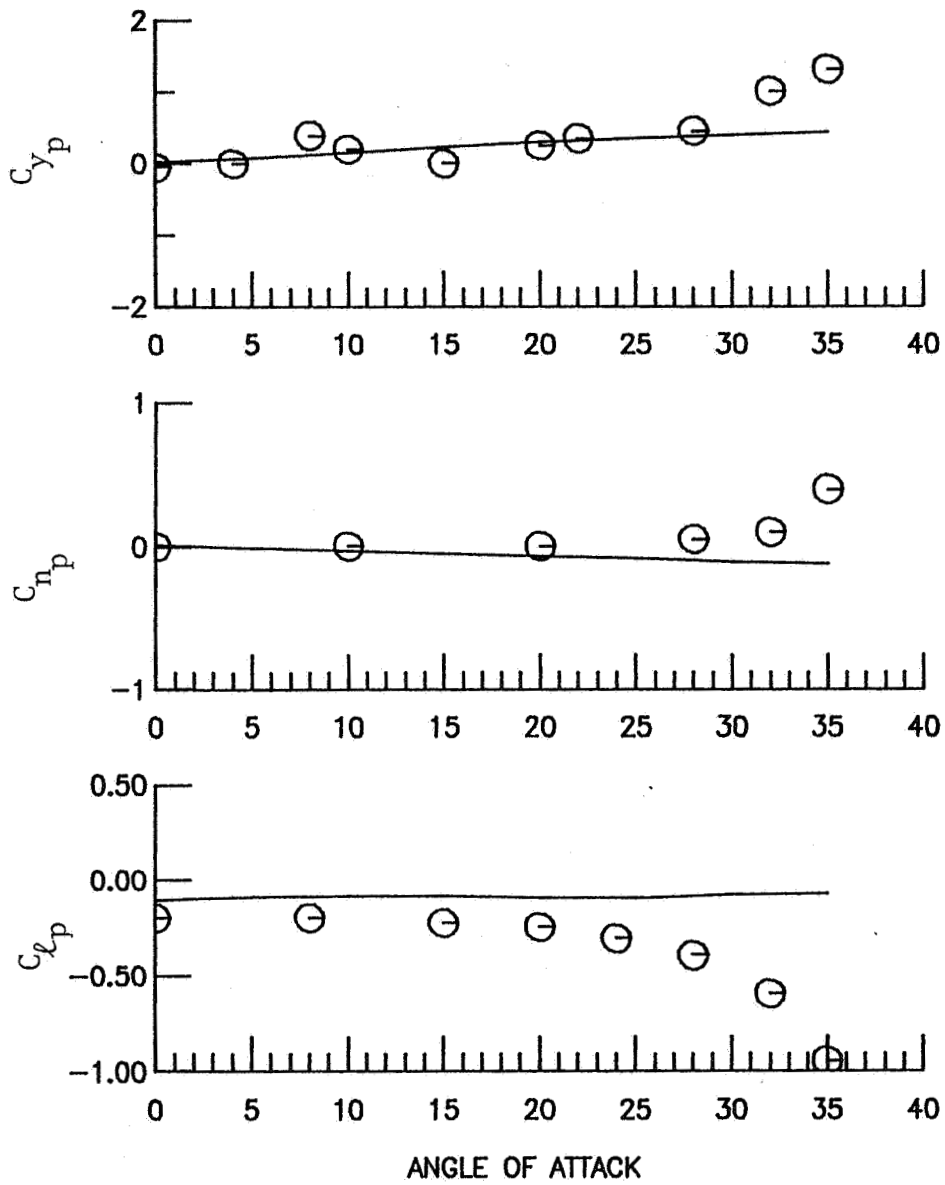


Figure 45. Lateral-Directional Derivatives Calculation of an F-106B Configuration Based on the Stability Axis at  $\bar{p} = 0.02$

⊖ — Forced Oscillation Data (Ref. 42)  
 ——— VORSTAB Calculation without Viscous Effect

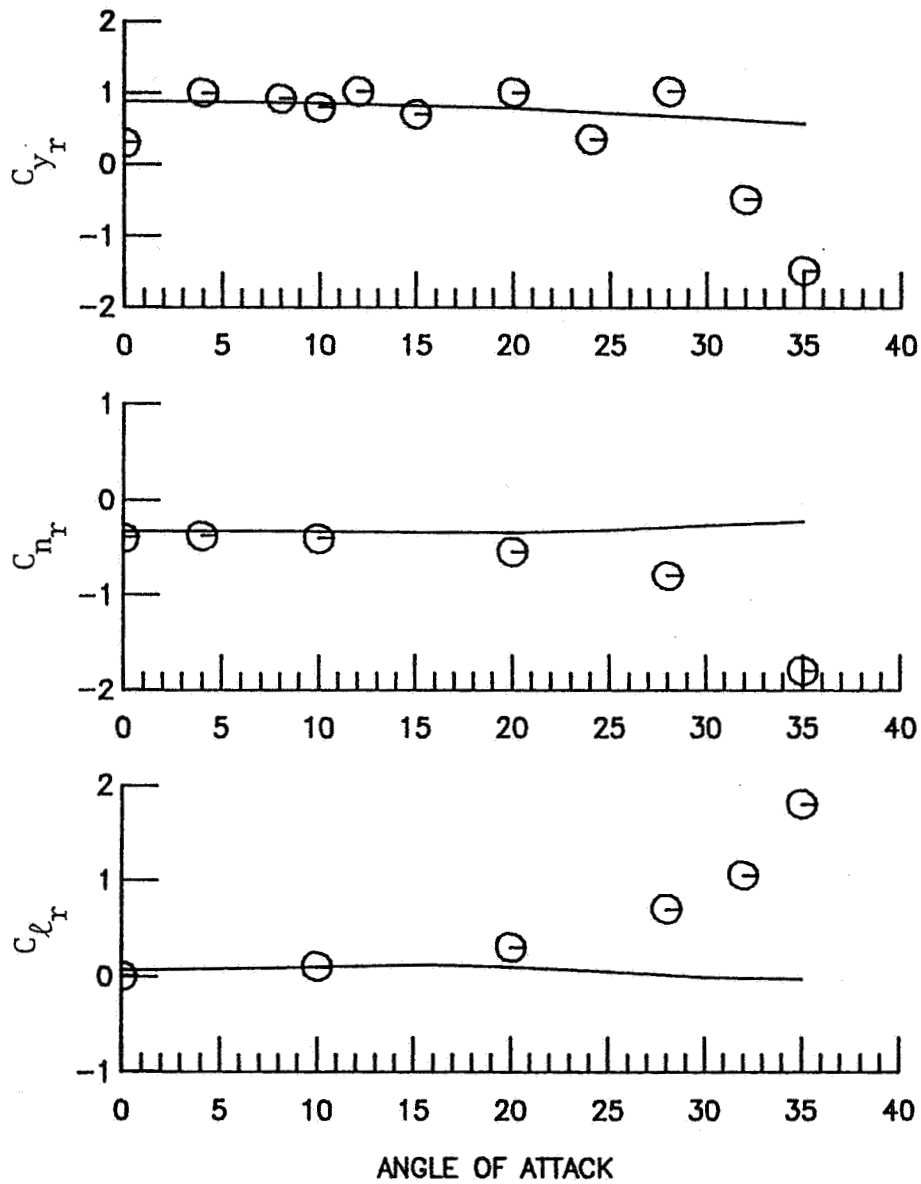


Figure 46. Lateral-Directional Derivatives Calculation of an F-106B Configuration Based on the Stability Axis at  $\bar{M} = 0.02$

⊖ — Experimental Data (Ref. 42)  
 ———— VORSTAB Calculation without Viscous Effect

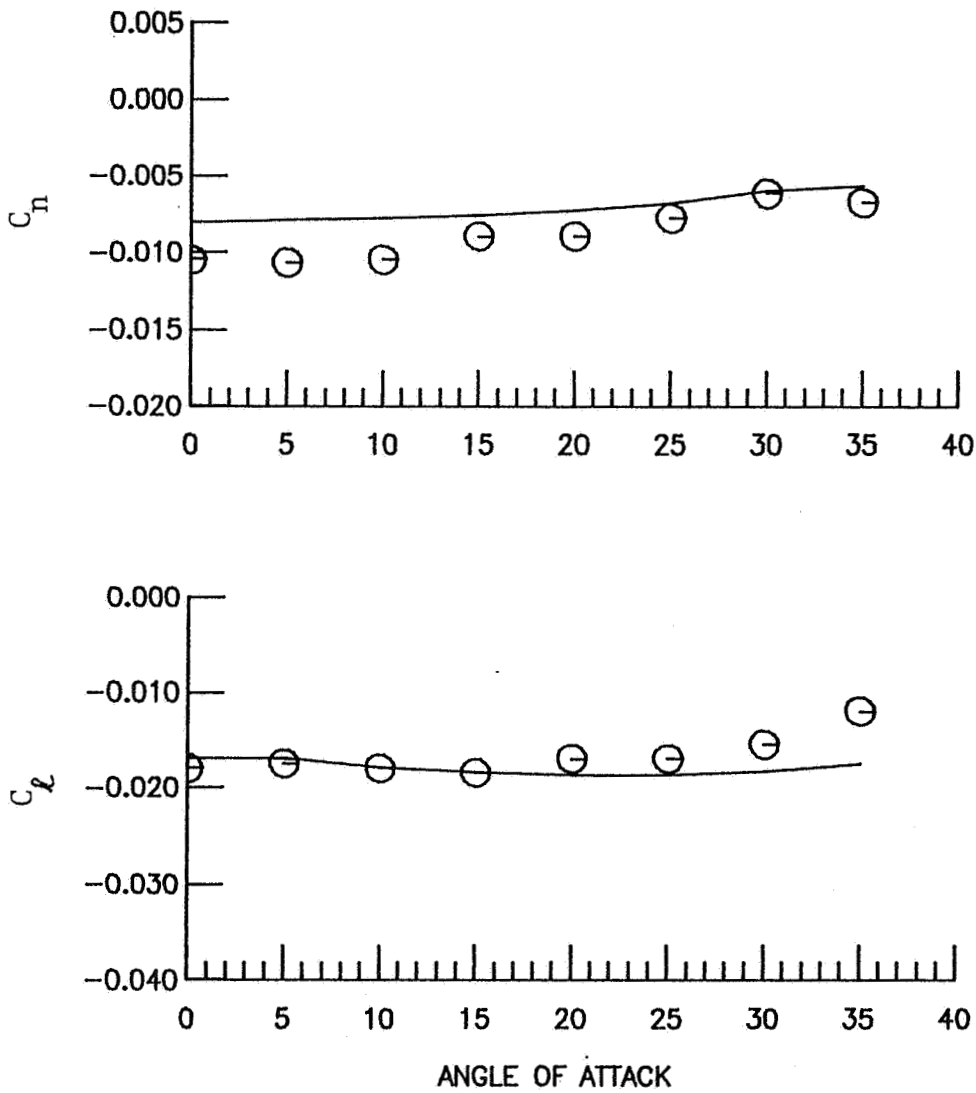


Figure 47. Calculation of an F-106B Aileron Control Power,  
 $\delta_A = 7$  Degrees

⊖ — Experimental Data (Ref. 42)  
 ——— VORSTAB Calculation without Viscous Effect

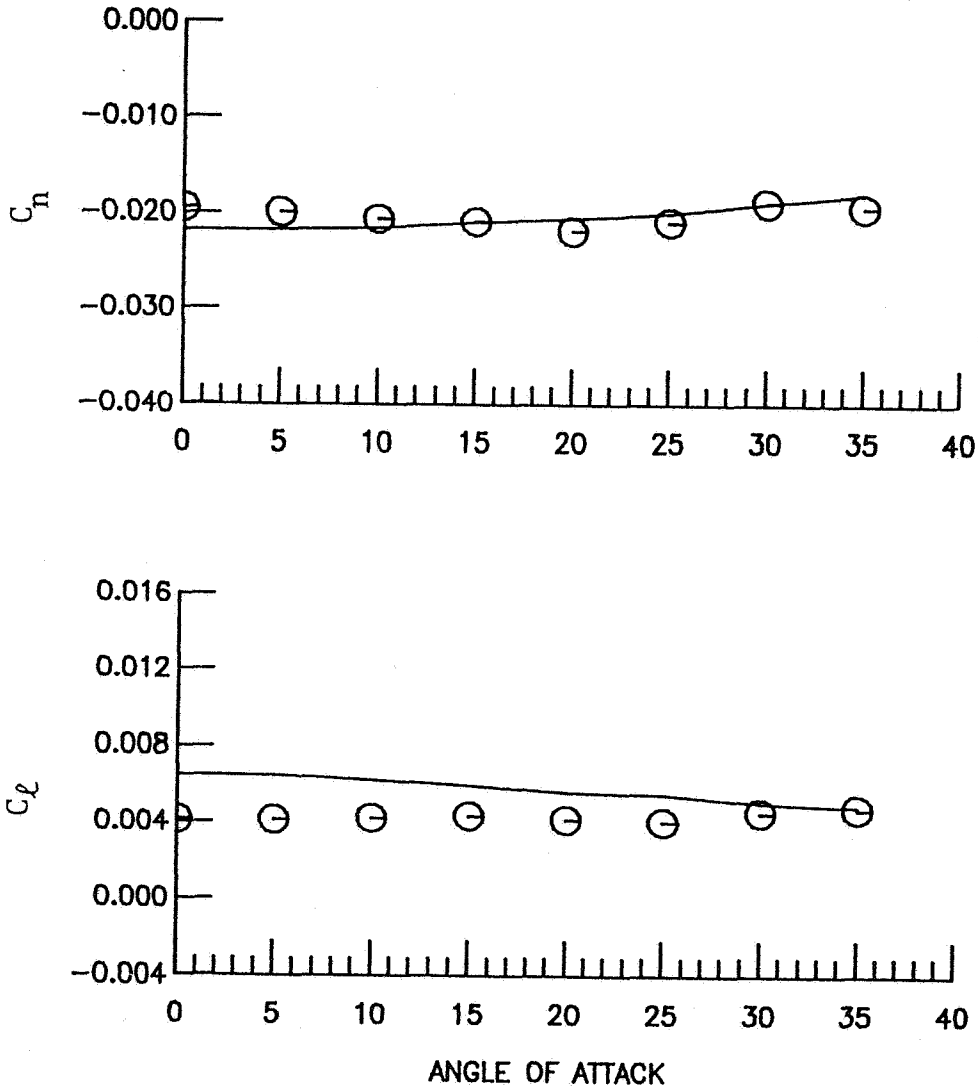


Figure 48. Calculation of an F-106B Rudder Control Power,  
 $\delta_r = 25$  Degrees



# Report Documentation Page

1. Report No. NASA CR-4182		2. Government Accession No.		3. Recipient's Catalog No.	
4. Title and Subtitle Calculation of Aerodynamic Characteristics of Airplane Configurations at High Angles of Attack				5. Report Date October 1988	
				6. Performing Organization Code	
7. Author(s) J. B. Tseng and C. Edward Lan				8. Performing Organization Report No. CRINC-FRL-730-1	
				10. Work Unit No. 533-02-01-03	
9. Performing Organization Name and Address Flight Research Laboratory The University of Kansas Center for Research, Inc. Lawrence, Kansas 66045-2969				11. Contract or Grant No. NAG1-635	
				13. Type of Report and Period Covered Contractor Report	
12. Sponsoring Agency Name and Address National Aeronautics and Space Administration Langley Research Center Hampton, VA 23665-5225				14. Sponsoring Agency Code	
15. Supplementary Notes  Langley Technical Monitor: William L. Sellers III Final Report					
16. Abstract  In this study, calculation of longitudinal and lateral-directional aerodynamic characteristics of airplanes by the VORSTAB code is examined. The numerical predictions are based on the potential flow theory with corrections of high angle-of-attack phenomena; namely, vortex flow and boundary layer separation effects. To account for the vortex flow effect, vortex lift, vortex action point, augmented vortex lift and vortex breakdown effect through the method of suction analogy are included. The effect of boundary layer separation is obtained by matching the nonlinear section data with the three-dimensional lift characteristics iteratively.  Through correlation with results for nine fighter configurations, it is concluded that reasonably accurate prediction of longitudinal and static lateral-directional aerodynamics can be obtained with the VORSTAB code up to an angle of attack at which wake interference and forebody vortex effect are not important. Possible reasons for discrepancy at higher angles of attack are discussed.					
17. Key Words (Suggested by Author(s)) Longitudinal Aerodynamics Lateral-Directional Stability Derivatives Vortex Flow Viscous Separation			18. Distribution Statement  Unclassified - Unlimited Subject Category 02		
19. Security Classif. (of this report) Unclassified		20. Security Classif. (of this page) Unclassified		21. No. of pages 120	22. Price A06

AIRCRAFT CONFIGUR.  
 ANGLE OF ATTACK  
 BOUNDARY LAYER SEPARATION  
 LONGITUDINAL STABILITY  
 DIRECTIONAL  
 VISCOUS FLOW

VORTICES  
 AERODYN. CONFIG.  
 POTENTIAL FLOW  
 FLOW THEORY  
 LIFT  
 FIGHTER AIRCRAFT

APPROVED  
 2/27/88